The vertical structure of turbulence above an urban canopy

Ph. D. thesis
Inauguraldissertation

vorgelegt der
Philosophisch-Naturwissenschaftlichen Fakultät
der Universität Basel

von

Christian Feigenwinter
aus Basel und Reinach (Baselland)

Basel, 1999

Institut für Meteorologie, Klimatologie und Fernerkundung
Departement Geographie der Universität Basel

Genehmigt von der Philosophisch-Naturwissenschaftlichen Fakultät der Universität Basel auf Antrag der Herren Professoren Eberhard Parlow, Basel und Christian Bernhofer, Dresden

Basel, den 11. Januar 2000

Prof. Dr. Andreas Zuberbühler
Dekan

Acknowledgements

My first thanks go to Prof. Dr. Eberhard Parlow at MCR Lab. At his Institute, I had all the freedom and support to finish my work according to my own ideas and my own schedule. He also made it possible for me to take part in several conferences and workshops, including the one in Vancouver, 1997.

Dr. Roland Vogt was the initiator of the BASTA-project and also of the special measurement campaign at the BALCAB-tower in summer 1995. Without his experience and his excellent climbing skills, the measurements would have been of poor quality. His encouragement during inevitable phases of stagnation was invaluable and his rich experience and scientific background were always a source of inspiration. He also reviewed the final manuscript. For all this, I want to express my sincere gratitude to him and I am confidently looking forward to present and future common projects.

Very little would have been possible without a solid computational background. “SysOp” Günter Bing from MCR Lab always had a solution for the little and big problems that arise whenever a computer is switched on naively.

I also thank Paul Wittlin, who invited us to use the antenna tower and the facilities of BALCAB, Basler Kabelfernsehen AG, at the Messe Basel for our measurements in summer 1995 and gave us all the support we needed, and also Guido Hornung, who gave us a hand during the installation procedure.

Dr. Mathias Rotach from the Dept. of Geography of the Swiss Federal Institute of Technology offered many conceptual and instrumental suggestions during the planning phase of the campaign. Also, his institute provided two sonics and six ventilated temperature/humidity sensors, which is gratefully acknowledged.

Special thanks are due to Dr. Matthias Roth in Vancouver, now in Singapore, who reviewed my TAC paper very carefully. This forced me to rethink and recalculate the results again and gave me the confidence to have done it right.

Dr. Peter Blattner in Wellington, New Zealand, scanned parts of the study for possible defects of my English.

Last but not least, the help and support of the MCR Lab staff is greatly appreciated. Dr. Dieter Scherer was always there to make up for my limited skills in physics and mathematics. Paul Muller prepared the mounting devices for the instruments in an excellent way. Eva van Gorsel tested and used my IDL-programs, this helped a lot to optimize the calculations, also she provided the pictures of the site.

My wife Karin’s patient and loving support during all these years was a source of delight, while Iris and Boris are happy that this study is finished, so that we can start some new projects together.

Reinach, September 99

Zusammenfassung

Von Juli 1995 bis Februar 1996 wurde eine Spezial-Messkampagne an einem 51 m hohen Mast auf dem Dach der Messe Basel, Schweiz, durchgeführt. Dabei wurden in drei Höhen (z/h = 1.5, 2.1 und 3.2) mit Ultraschall-Anemometer-Thermometern gleichzeitig die turbulenten Ströme von Impuls und fühlbarer Wärme gemessen. Diese Arbeit analysiert die hochfrequenten Turbulenzmessungen (20.83 Hz) mit verschiedenen Methoden.

Die Beziehungen der Monin-Obukhov Ähnlichkeits-Theorie für die integralen Statistiken werden für die mechanischen Eigenschaften der Turbulenz leicht unterschätzt, für die thermischen Eigenschaften in den beiden unteren Niveaus gut angenähert.

Die Analyse der gemittelten Fourier-Spektren zeigt eine gute Übereinstimmung mit den Referenz-Spektren aus dem Kansas-Experiment. Die mittlere räumliche Ausdehnung eines turbulenten Wirbels, welche unter Anwendung der Taylor-Hypothese aus den Peak-Frequenzen der Spektren errechnet wurde, wird jeweils mit zunehmender Höhe und zunehmender Instabilität grösser. So lassen sich unter leicht instabilen Bedingungen in der Höhe z/h = 3.2 Werte von 1200 m, 412 m und 141 m für die horizontale, laterale und vertikale Ausdehnung angeben.

Mittels Quadranten-Analyse wurden Häufigkeit, Art und Grösse der organisierten Strukturen ermittelt. Die Resultate sind stark von der herrschenden Schichtung abhängig. Unter neutralen Bedingungen deutet der Übergang zur Dominanz der „ejections“ auf eine Obergrenze der Rauhigkeitsschicht zwischen z/h = 2.1 und z/h = 3.2 hin. Mit zunehmender Instabilität vermindert sich die Mächtigkeit der Rauhigkeitsschicht und es bildet sich oberhalb von z/h = 1.5 eine „constant flux layer“ aus. Dies wird durch die Analyse der Profile der turbulenten Flüsse von Impuls und fühlbarer Wärme bestätigt.

Die Anwendung der Wavelet-Analyse erlaubt es, organisierte Strukturen (ejection-sweep cycles), welche sich in Temperatur-Rampen manifestieren, zu detektieren und in ihrem mittleren zeitlichen Verlauf und im vertikalen Profil darzustellen. Es zeigt sich, das die organisierten Strukturen ähnlich verlaufen wie über vegetationsbewachsenen Oberflächen, die dominante Zeitskala ist mit ca. 90 Sekunden allerdings wesentlich länger. Die gefundene Strukturen sind effizient im Transport von fühlbarer Wärme, wogegen deren Beitrag zum Impulstransport eher gering ist.

Abstract

In this study, the fluctuations of the horizontal wind components u' and v', the vertical component w' and temperature T', sampled with 20.83 Hz and measured simultaneously at three levels (z/h=1.5, 2.1 and 3.2, with z as the sensor height and h the height of the roughness elements) over an urban canopy in the inner city of Basel, Switzerland, from July 1995 to February 1996 are analyzed. By combining the results from spectral analysis, quadrant analysis and wavelet analysis, patterns of the organized structures (first- and second order moments) under unstable conditions have been calculated and their dominating time scale has been determined. The conditionally sampled fluxes have been compared to the conventionally (Reynolds-)averaged fluxes.

The analysis of the integral statistics shows that the dimensionless standard deviation σ_w/u_* is slightly smaller than the Monin-Obukhov similarity function, whereas the σ_θ/θ_* values follow the inertial sublayer prediction very close for the two lower levels. The profile of friction velocity suggests that the upper boundary of the roughness sublayer lies between z/h = 2.1 and z/h = 3.2 for neutral conditions. This is also the height where ejections start to dominate over sweeps in quadrant analysis. As instability increases, the magnitude of the roughness sublayer is diminished and the profiles of momentum and sensible heat flux suggest, that a constant flux layer is established above z/h = 1.5.

Composite spectra are in a reasonable correspondence with the reference spectra from the Kansas experiment. The wavelengths derived from peak frequencies, applying Taylor's hypothesis, become larger with both, increasing height and increasing instability. The longitudinal, lateral and vertical magnitude of a mean eddy under weakly unstable conditions at z/h = 3.2 was determined to be 1200 m, 412 m and 141 m, respectively.

The analysis of the organized structures shows a remarkably stable pattern, which is very similar to the profiles found over vegetation canopies, however the dominating time scale of around 90 seconds is significantly larger due to the rougher surface and the higher roughness elements. The found structures are efficient in transporting sensible heat, but the contribution of the detected events to the transport of momentum is low, and the association with the temperature ramp is even lost at the uppermost measurement level at z/h = 3.2 for the conditionally sampled horizontal wind component and the friction velocity.

Table of contents

1 Introduction 1

2 Theory 3

2.1 The planetary boundary layer 3

2.2 The structure of the urban boundary layer 6

2.3 Similarity theory 7

2.3.1 Monin-Obukhov similarity 7

2.4 Spectral analysis 10

2.4.1 Data processing for spectral analysis 11

2.5 Quadrant analysis 12

2.6 Wavelets 14

2.6.1 Basics 14

2.6.2 Wavelet applications in atmospheric in turbulence research 16

2.6.3 The method 17

2.6.4 Conditional sampling 19

3 Experimental setup 21

3.1 Observation site 21

3.2 Instrumentation 24

3.3 Meteorological conditions 25

4 Results 29

4.1 Estimation of the zero plane displacement height 29

4.2 Integral statistics 30

4.2.1 Profiles 30

4.2.2 Normalized standard deviations 34

4.3 Quadrant analysis 36

4.4 Spectral analysis 42

4.4.1 Velocity spectra 42

4.4.2 Temperature spectra 45

4.4.3 Cospectra 45

4.5 Wavelet analysis 47

4.5.1 Meteorological conditions 47

4.5.2 Event detection 48

4.5.3 First order moments 55

4.5.4 Second order moments 59

5 Summary and conclusions 63

5.1 Mechanical and thermal properties 63

5.2 Organized motions 63

5.3 The structure of the lower urban boundary layer 63

5.4 Outlook 64

References 65

A Appendix 69

A.1 Ultrasonic anemometer/thermometer measurement principles 69

A.2 The Gill-Solent 3 axis research ultrasonic anemometer/thermometer 71

A.3 Sonic calibration and intercomparison 73

List of figures

Fig. 2.1: The concept of an idealized PBL (adapted and slightly modified from Schmid and Rotach, 1997). 3

Fig. 2.2: Concept of the sublayers in the UBL, with z_i as mixed layer height and z_* as the height of the roughness sublayer (adapted from Rotach, 1999). 6

Fig. 2.3: The vertical structure of an urban boundary layer, modified after Oke (1988). 6

Fig. 2.4: Schematic turbulence spectrum with: 1) energy containing range, 2) inertial subrange and 3) dissipation range (adapted from Kaimal and Finnigan, 1994). 10

Fig. 2.5: Arbitrarily chosen spectrum of vertical velocity component. Light gray: raw spectrum, (+) frequency smoothing (spectrum averaged into 20 bands), (*) spectral slicing (spectrum composed from high-frequency and low-frequency spectrum), (Δ) tapered spectrum with spectral slicing. 11

Fig 2.6: The concept of quadrant analysis and the definition of the hyperbolic hole *H*. Adapted from Shaw et al. (1983). 12

Fig. 2.7: Phase-space representation using the wavelet transform (adapted from Kumar and Fourfoula, 1994). 16

Fig. 2.8: The Mexican hat wavelet in the time (top) and frequency (bottom) domain. 17

Fig. 2.9: Wavelet transform (top) of the artificial ramp time series (middle, solid line). Cross sections (grey) of the wavelet transform (the wavelet coefficients) for scales corresponding to periods of 5 (solid), 20 (dotted), 50 (dashed) and 100 seconds (dashed-dotted) are shown in the middle. The plot at the bottom shows the wavelet spectrum (+) and two Fourier spectra with a different number of classes for frequency smoothing (◊: 10 classes, Δ: 15 classes). 18

Fig. 3.1: The Basel region from satellite view (Composite Landsat-TM5 and SPOT, A. Hold, MCR Lab). 21

Fig. 3.2: Location of the measurement tower in the inner city of Basel. The radius of the circle is 1000 m. 22

Fig. 3.3: View from the measurement tower to North West (E. van Gorsel, MCR Lab). 23

Fig. 3.4: View from the measurement tower to North East (E. van Gorsel, MCR Lab). 23

Fig. 3.5: View from the measurement tower to South (E. van Gorsel, MCR Lab). 23

Fig. 3.6: Situation of the tower and instrumentation setup. View from south. 24

Fig. 3.7: Ground-plan of the tower (scale 1:50) and instrumentation setup (1:25) (E. van Gorsel, MCR Lab). 25

Fig. 3. 8: Distribution of wind direction (16 classes) and wind speed for the measurement period. From left to right: all stability classes, night-time values (R_n < -20 Wm^{-2}, 1846 hours), day-time values (R_n > 0 Wm^{-2}, 1626 hours). Dark to light gray colors refer to wind velocities greater than 0, 2, 3 and 4 m/s, respectively. Circles refer to percentage of all considered respective values. 26

Fig. 3.9: Course of air temperature at z/h=1.3 during the measurement period. 26

Fig. 3.10: Course of air temperature differences $\theta_{z/h=3.2}$-$\theta_{z/h=1.3}$ during the measurement period. 27

Fig. 4.1: Scaled profiles of standard deviation $\sigma_u/u_{*\,top}$ for all stability classes. 30

Fig. 4.2: Scaled profiles of standard deviation $\sigma_v/u_{*\,top}$ for all stability classes. 31

Fig. 4.3: Scaled profiles of standard deviation $\sigma_w/u_{*\,top}$ for all stability classes. 31

Fig. 4.4: Scaled profiles of standard deviation $\sigma_\theta / \sigma_{\theta top}$ for all stability classes. 31

Fig. 4.5: Averaged profiles of friction velocity u_* for all stability classes. The shaded regions refer to ±10% of the value at z/h = 2.1. 32

Fig. 4.6: Averaged profiles of kinematic heat flux $\overline{w'\theta'}$ for all stability classes. The shaded regions refer to ±10% of the value at z/h = 2.1. 32

Fig. 4.7: Left column: σ_w/u_* for unstable conditions. Class averages are plotted with standard deviations as error bars (fitted curve in light gray). Functional relationships are from Panofsky and Dutton (1984) (solid), Clarke et al. (1982) (dotted) and Rotach (1993b) (dashed-dotted). Right column: same as left but for $-\sigma_\theta/\theta_*$. Functional relationships is after De Bruin et al. (1993). The free convection limit is indicated by the dashed line. 33

Fig. 4.8: Profiles of stress fractions $S(i,H)$ (top) and time fractions $T(I,H)$ (bottom) for all stability classes. 36

Fig. 4.9: Contribution of stress fractions $S(i,H)$ for varying hole size H and all stability classes. 36

Fig. 4.10: Cumulative magnitudes of stress fractions $\Sigma S(i,H)$ (solid) and time fractions $\Sigma T(i,H)$ (dashed) for varying hole size H and all stability classes. 37

Fig. 4.11: As figs. 4.8 and 4.9, but for neutral stratification $|(z-z_d)/L| < 0.05$. 38

Fig. 4.12: Averaged vertical profiles of momentum flux fractions (left) and sensible heat flux fractions (right) contributed by the four quadrants for weakly unstable stratification $-0.5 < (z-z_d)/L < -0.05$. 38

Fig. 4.13: Contribution of stress fractions (left) and heat flux fractions (right) for varying hole size H and weakly unstable stratification $-0.5 < (z-z_d)/L < -0.05$. 39

Fig. 4.14: Cumulative magnitudes of flux fractions $\Sigma S(i,H)$ (solid) and time fractions $\Sigma T(i,H)$ (dashed) of momentum flux (left) and sensible heat flux (right) for varying hole size H and weakly unstable stratification $-0.5 < (z-z_d)/L < -0.05$. 39

Fig. 4.15: Averaged vertical profiles of momentum flux fractions (left) and sensible heat flux fractions (right) contributed by the four quadrants for unstable stratification $(z-z_d)/L < -0.5$. 40

Fig. 4.16: Contribution of stress fractions (left) and heat flux fractions (right) for varying hole size H and unstable stratification $(z-z_d)/L < -0.5$. 40

Fig. 4.17: Spectra of longitudinal wind component u (left) and lateral wind component v (right) for stable (dashed-dotted), neutral (dotted), weakly unstable (solid) and unstable (dashed) conditions. Reference spectrum from Kaimal et al. (1972) (solid thin). 43

Fig. 4.18: As fig. 4.17 but for vertical wind component w. 43

Fig. 4.19: As fig. 4.17 but for ratios of spectral energy densities $S_w(f)/S_u(f)$. Reference curve (solid thin) from Kaimal et al. (1972). 44

Fig. 4.20: As fig. 4.17 but for sonic temperature θ_s. 45

Fig. 4.21: As fig. 4.17 but for cospectra of $u'w'$.(left) and cospectra of $w'\theta'$ (right). 46

Fig. 4.22: Meteorological conditions from August 3 to 5 1995 (DOY 215-217). From top to bottom and from left to right: Net radiation, air temperature at z/h=1.5, wind speed at z/h=3.2, relative humidity at z/h=1.5, wind direction at z/h=3.2, stability index (+: z/h=1.5, ∗: z/h=2.1, Δ: z/h=3.2), u_* and sensible heat flux (solid: z/h=1.5, dotted: z/h=2.1, dashed-dotted: z/h=3.2). The periods selected for analysis are shaded. 47

Fig. 4.23: Arbitrarily chosen time series of temperature fluctuations θ '. The three windows refer to z/h=3.2, 2.1 and 1.5 (from top to bottom). 48

Fig. 4.24: Temperature fluctuations θ' (bottom) and corresponding wavelet scalograms (top) for DOY 215, 16:00-16:53. The three windows refer to z/h=3.2, 2.1 and 1.5 (from top to bottom). 49

Fig. 4.25: Wavelet scalograms (top) and time series (bottom) for DOY 215, 16:00-16:53 at z/h = 1.5. The five windows refer to w', u', θ ' , $u'w'$ and $w'\theta$' (from top to bottom). 50

Fig. 4.26: Wavelet (left) and Fourier spectra of u', w' and θ' (top to bottom) for the period from 10:00 to 18:00 on DOY 215. Measurements at z/h: solid line = 1.5, dotted line = 2.1 and dashed line = 3.2. Displayed are averages of spectra based on hourly runs (background, light gray). 53

Fig. 4.27: Wavelet (left) and Fourier spectra of u', w' and θ' (top to bottom) for the period from 15:00 to 18:00 on DOY 216. Measurements at z/h: solid line = 1.5, dotted line = 2.1 and dashed line = 3.2. Displayed are averages of spectra based on hourly runs (background, light gray). 53

Fig. 4.28: Wavelet (left) and Fourier spectra of u', w' and θ' (top to bottom) for the period from 10:00 to 18:00 on DOY 217. Measurements at z/h: solid line = 1.5, dotted line = 2.1 and dashed line = 3.2. Displayed are averages of spectra based on hourly runs (background, light gray). 54

Fig. 4.29: Time series of temperature fluctuations θ' (filtered by a 5 s running mean) at z/h = 3.2, 2.1 and 1.5 (from top to bottom) on DOY 215, 14:00-14:53. Solid lines indicate the detected events taken for conditional sampling. Dashed lines are detected events at z/h = 1.5, that do not have corresponding temperature ramps above. 54

Fig. 4.30: Superimposed conditional averages (light gray), normalized by the corresponding standard deviation for $\langle u' \rangle$, $\langle w' \rangle$ and $\langle T' \rangle$ (left to right) at z/h =3.2, 2.1 and 1.5 (from top to bottom) for 8 runs from 10:00-18:00 on DOY 215. Solid thick lines indicate the over-all average. 56

Fig. 4.31: Averaged pattern of ejection-sweep cycles from DOY 215. Contours represent $\langle T' \rangle$ values (light colors positive, dark colors negative, contour lines: solid: ± 0.5, dotted: 0.0). Arrows correspond to $\langle u' \rangle$ (horizontal component) and $\langle w' \rangle$ (vertical component). All values are normalized by their respective standard deviation. 56

Fig. 4.32: As fig. 4.30 but for DOY 216, 15:00-18:00 57

Fig. 4.33: As fig. 4.31 but for DOY 216, 15:00-18:00 57

Fig. 4.34: As fig. 4.30 but for DOY 217, 10:00-18:00 58

Fig. 4.35: As fig. 4.31 but for DOY 217, 10:00-18:00 58

Fig. 4.36: Conditional averages $<u'w'>$ and $<w'T'>$ and cross-products $<u'><w'>$ and $<w'><T'>$ (normalized by $\left|\overline{u'w'}\right|$ and $\left|\overline{w'T'}\right|$) for DOY 215, 10:00-18:00. 60

Fig. 4.37: Same as fig. 4.36 but for DOY 217, 10:00-18:00. 61

Fig. A.1: Schematic view of a sonic path. 69

Fig. A.2: Side-view (left) and top-view (right) of the Gill-Solent sonic anemometer/thermometer 71

Fig. A.3: The three sonics at the field intercomparison in Tuscany 1996 73

Fig. A.4: Comparison of matrix calibration and manufacturer's (Gill-) calibration. Regression line solid, light gray, 1:1 line dotted. 75

Fig. A.5: Comparison between instruments. Regression line solid, light gray, 1:1 line dotted. 76

List of tables

Tab. 2.1:	Relationship between stability parameters	8
Tab. 2.2:	Empirical constants for MOS-relationships	9
Tab. 3.1:	Instrumental setup (see also fig. 3.6)	24
Tab. 4.1:	Values for the zero plane displacement height z_d calculated by the temperature variance method for the selected wind direction sections (number of runs per section in brackets).	29
Tab. 4.2:	Stability classes and number of analyzed 53-minute runs for profiles and integral statistics	30
Tab. 4.3:	Number of analyzed 53-minute runs for nondimensionalized standard deviations (σ_w/u_* / $-\sigma_\theta/\theta_*$) in fig. 4.7.	34
Tab. 4.4:	Comparison of values C_1 and C_2 in eq. (2.26) for σ_w/u_* and σ_θ/θ_* from different studies	35
Tab. 4.5:	The ratio of summed time fractions to summed stress fractions for hole size 5 and 10, ΔS_0, $\gamma = S_{2,0}/S_{4,0}$ and Exuberance Ex for all stability classes	37
Tab. 4.6:	Spectral peak frequencies of wind components u, v and w above urban surfaces (except Kaimal et al., 1972) from various studies.	44
Tab. 4.7:	(Co)spectral peak frequencies of temperature θ, momentum flux $\overline{u'w'}$ and kinematic heat flux $\overline{w'\theta'}$ above urban surfaces (except Kaimal et al., 1972) from various studies.	46
Tab. 4.8:	Comparison of dominating time scales in other studies	51
Tab. 4.9:	Meteorological conditions for the analyzed runs of DOY 215	52
Tab. 4.10:	Meteorological conditions for the analyzed runs of DOY 216	52
Tab. 4.11:	Meteorological conditions for the analyzed runs of DOY 217	52
Tab. 4.12:	Statistics of event detection for DOY 215 and 217	55
Tab. 4.13:	Ratios of conditionally averaged heat flux to Reynolds flux and large-scale contributions for the runs of DOY 215, 216 and 217. N is the number of samples in a time window.	60
Tab. A.1:	Operation modes of the Gill Research sonic	71
Tab. A.2:	Regression coefficients for calibration comparison: $y_{gill}=a0+a1*x_{matrix}$	73
Tab. A.3:	Regression coefficients and standard deviations for instrument comparison: $y_{instr\ 1}=a0+a1*x_{instr\ 2}$	74

List of symbols and abbreviations

α	wind direction
β	Bowen ratio
γ_H	ratio of sweeps to ejections at hole size H
ε	dissipation rate of turbulent kinetic energy
ζ	stability index
τ	surface shear stress
τ	wavelet position dilation
θ	potential temperature
θ_*	scaling temperature
$\varphi_{1,2,3}$	sonic angles
$\upsilon_{1,2,3}$	sonic angles
ψ	wavelet function
λ	wavelength
λ_m	peak wavelength
λ_v	latent heat of vaporization
ϕ_i	semi-empirical function for property i
σ_x	standard deviation of property x
ρ	density of air
ω	frequency
c	speed of sound
c_p	specific heat of air at constant pressure
$c_{f,s,1,2,x}$	empirical constants for MOS-relationships (f: free convection, s: stable) for property x
C_ψ	admissibility parameter for wavelet function ψ
d	sonic path length, distance apart transducers
E	evaporation rate
Ex	Exuberance
e	vapor pressure
q	specific humidity
f	non-dimensional frequency
f_c	Coriolis parameter
f_m	peak frequency
g	acceleration due to gravity
$\Re$	gas constant for dry air
h	mean height of roughness elements
H	turbulent flux of sensible heat

H	hyperbolic hole size
k	von Karman constant
L	Monin-Obukhov length
M_{jk}	statistical moments
n	natural frequency
p	atmospheric pressure
q	specific humidity
Rf	bulk Richardson number
Ri	gradient Richardson number
R_n	net radiation
R_{wc}	correlation coefficient for properties w and c
s	wavelet scale
S_{moist}	effect of evaporation on moisture change
S_x	spectral energy density of property x
$S_{i,H}$	flux fraction in quadrant i for hole size H
$T_{i,H}$	time fraction in quadrant i for hole size H
T	temperature
t	time
T_{sv}	acoustic virtual temperature
T_v	virtual temperature
$\boldsymbol{U}$	wind vector
u_*	friction velocity
u, v, w	longitudinal, lateral and vertical component of wind vector
$\boldsymbol{V}$	sonic path vector
$V_\perp$	normal path component
V_p	along path component
W	Wavelet coefficients
z	height above ground level
z_d	zero plane displacement height
z_*	height of the roughness sublayer
z_i	mixed layer height, height of the PBL

TKE	turbulent kinetic energy
UBL	urban boundary layer
PBL	planetary boundary layer
RS	roughness sublayer
SL	surface layer
CL	canopy layer
FFT	fast Fourier transform

1 Introduction

The biggest part of the human population lives in cities or urban agglomerations. Anthropogenic activities (living, working, traffic, etc.) modify more and more these urban areas in manifold ways. Cities consist of building structures of different vertical and horizontal extension with varying building material. The interaction between this complex urban morphology and the atmosphere close to the ground leads to the urban boundary layer. A city in its complete extension influences the physical and the chemical state of the lower 1-2 km of the atmosphere.

The discussion on the predicted global climate change has shifted again increasing interest to the topic "urban climate". Many measurements of air temperature were done at places, which during this century gradually changed from rural to urban sites, and therefore for example the question arises, whether the measured increased temperatures could not be explained by the heat island effect.

In the early years of urban climate research the primary scope was focussed on finding measures for the strength of the urban anomaly compared to its “rural” counterpart. The climate of cities has been recognized as a mesoscale phenomenon whose properties are affected by anthropogenic influences and urban planning. In general there are three main characteristics valid for most urban atmospheres (i.e. Landsberg, 1981, Oke, 1987, Garrat, 1992):

- The urban environment in the nighttime is warmer than the surrounding areas, this fact is usually referred to as the “urban heat island”.
- Due to the very rough surface of a city, the air motion is slower compared to rural surfaces.
- Evaporation rates are generally lower because large parts of the ground are sealed.

In recent years the aspect of air pollution became increasingly important in urban climate research (Cermak, 1995). Sources of pollutants are highly concentrated in urban areas and some of them could sensitively harm the health of the residents in case of an accident. A better understanding of the dispersion processes over heterogeneous terrain like an urban surface is therefore needed for the development of dispersion models and models for accident scenarios, where a fast and well founded forecast could even save lives.

The transport of any property in the atmosphere is strongly associated with advection and dispersion. Dispersion again is governed to a large amount by the turbulent state of the lower atmosphere. The knowledge of these turbulent characteristics is therefore an essential part for the design of a useable dispersion model (Rotach, 1999). Unfortunately the common “classical” theories for the description of atmospheric turbulence rely on flat and homogeneous surface types. In complex terrain and especially over a rough urban surface the required preconditions of these theories are often not given and their application becomes questionable at least.

The aim of this study is to provide more information about the nature and the structure of turbulence in the lowest one hundred meters above a typical European urban surface. Beside the classical approaches the identification and description of organized motions was a main point of interest. The results should also give a contribution to the design of future experiments on the subject.

2 Theory

2.1 The planetary boundary layer

The planetary boundary layer (PBL, also known as the atmospheric boundary layer, ABL) is the region of the lowest 1-2 km of the lower atmosphere (troposphere). Its depth and structure is determined by the physical and thermal properties of the underlying surface in conjunction with the dynamics and thermodynamics of the lower atmosphere. Above the PBL is the free atmosphere, where the flow is no longer influenced by surface properties and is in near-geostrophic balance. The PBL is the layer, where the turbulent exchange of momentum, heat and mass occurs. The energy for this turbulent exchange is provided by the large vertical wind shear and the thermal effects of surface heating. Temporal variations of the PBL depth are forced by the diurnal cycle of heating and cooling the surface and the evolution and passage of mesoscale and synoptic scale systems, while spatial variations occur due to changes in land use and surface topography. The PBL responds to surface forcings with a timescale of about an hour or less.

Fig. 2.1 shows the concept of an idealized homogeneous, stationary and neutrally stratified boundary layer.

The main characteristics of the regions and layers are:

- outer region: the turbulent fluxes vary with height (mostly decreasing with increasing height). With increasing height, the influence of the surface (friction) decreases in favor of the Coriolis effects. Wind direction changes to the geostrophic direction at the upper boundary. The most important scaling length is the height of the PBL z_i.
- inner region: vertical turbulent fluxes can be considered as constant. Coriolis effects can be neglected in favor of friction forces. The most important scaling length is the height above ground z.
- mixed layer: turbulence is mainly driven by thermal convection
- inertial sublayer: the characteristics of both regions hold approximately.
- roughness sublayer: influences of the surface and the roughness elements force the flow to be essentially three dimensional.
- canopy layer: characteristic profiles of mean variables and higher order moments for certain types of canopies, highly intermittent turbulence.

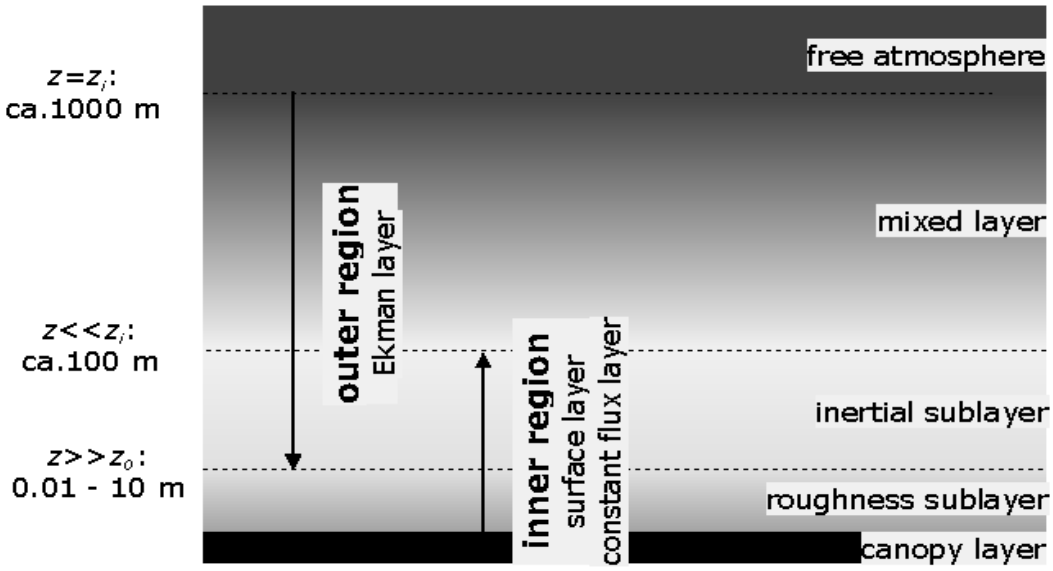

Fig. 2.1: The concept of an idealized PBL (adapted and slightly modified from Schmid and Rotach, 1997).

This is just an idealized concept of the PBL, which is varying strongly according to atmospheric and surface conditions. The next section will treat the subject of the urban boundary layer more sophistically.

The state of the atmosphere can be described by the following seven variables:

- the wind velocity vector ***U*** with its longitudinal, lateral and vertical components *u, v* and *w*
- temperature *T* or potential temperature θ
- pressure *p*
- density ρ
- specific humidity *q*

Five equations form the frame in which the spatial (*x, y, z*) and temporal (*t*) dependence of these variables can be described, namely: the conservation equations for momentum (equations of motion, Navier-Stokes' equations), mass (continuity equation), moisture and heat (the first law of thermodynamics) and the equation of state for ideal gases. For this complex set of equations as applied to the boundary layer, no analytical solution is known. Therefore the equations have to be simplified depending on the scale of the problem to solve by eliminating terms that are orders of magnitude smaller than others.

To separate the processes of different scales, Reynolds' decomposition is usually applied. The variables of interest are split into a mean and a fluctuating part. For any given variable *x*, this means

$$x = \overline{x} + x' \tag{2.1}$$

where $\overline{x}$ is the average of *x* over a given time interval and *x'* is the momentary deviation from this average. By this, $\overline{x'} = 0$ and for the product of two variables *x* and *y*

$$\overline{xy} = \overline{x} \cdot \overline{y} + \overline{x'y'} \tag{2.2}$$

holds. Note that the nonlinear term $\overline{x'y'}$ is not necessarily zero. The second moments $\overline{x'^2}$ and $\overline{x'y'}$ can be interpreted in a statistically sense as variance and covariance, respectively.

Applying Reynolds' averaging and assuming several reasonable conditions, that are valid in the PBL, namely:

- incompressibility,
- hydrostatic equilibrium of the mean flow (dynamic pressure changes are negligible),
- density changes are only essential for $\rho' g$,
- $(\rho', \theta', p') << \left(\overline{\rho}, \overline{\theta}, \overline{p}\right)$,
- molecular diffusivity << turbulent diffusivity,

the governing equations can be substantially simplified to a *Boussinesq* set of equations for the mean motions in the turbulent boundary layer (see i.e. Stull (1988) or Panofsky and Dutton (1984) for a comprehensive derivation of the equations):

$$\frac{d\overline{u}}{dt} = f_c \overline{v} - \frac{1}{\overline{\rho}} \frac{\partial \overline{p}}{\partial x} - \frac{\partial(\overline{u'w'})}{\partial z} \tag{2.3}$$

$$\frac{d\overline{v}}{dt} = f_c \overline{u} - \frac{1}{\overline{\rho}} \frac{\partial \overline{p}}{\partial y} - \frac{\partial(\overline{v'w'})}{\partial z} \tag{2.4}$$

$$\frac{d\overline{w}}{dt} = -g - \frac{1}{\overline{\rho}} \frac{\partial \overline{p}}{\partial z} \tag{2.5}$$

the equations of motion (conservation of momentun), where f_c is the Coriolis parameter and *g* the acceleration due to gravity,

$$\frac{d\overline{T}}{dt} = -\frac{1}{\overline{\rho} c_p} \left(\lambda_v E + \frac{\partial \overline{R}_n}{\partial z} \right) - \frac{\partial(\overline{w'\theta'})}{\partial z} \tag{2.6}$$

the first law of thermodynamics, where the first term on the right side stands for the effect of net radiation and the effect of latent heat on temperature change, R_n is the net radiation, *E* the evaporation rate, λ_v the latent heat of vaporization of water and c_p the specific heat at constant pressure for moist air,

$$\frac{d\overline{q}}{dt} = -\frac{\partial(\overline{w'q'})}{\partial z} + S_{moist} \tag{2.7}$$

the conservation of moisture, where S_{moist} stands for the effect of evaporation on moisture change,

$$\overline{p} = \overline{\rho} \Re \overline{\theta} (1 + 0.61 \overline{q}) \tag{2.8}$$

the equation of state with $\Re$ as the gas constant for dry air and

$$\frac{\partial \overline{u}}{\partial x} + \frac{\partial \overline{v}}{\partial y} + \frac{\partial \overline{w}}{\partial z} = 0 \tag{2.9}$$

the continuity equation.

The total derivative *d/dt* is defined as

$$\frac{d}{dt} = \frac{\partial}{\partial t} + \overline{u} \frac{\partial}{\partial x} + \overline{v} \frac{\partial}{\partial y} + \overline{w} \frac{\partial}{\partial z} \tag{2.10}$$

From the equations of motion eqs. (2.3-5) the budget equation for turbulent kinetic energy (TKE) per unit mass , defined as $\overline{e} = \frac{1}{2}\left(\overline{u'^2 + v'^2 + w'^2}\right)$,

close to the surface can be written after Panofsky and Dutton (1984) as

$$\underset{I}{\frac{d\bar{e}}{dt}} = \underset{II}{-\overline{u'w'}\frac{\partial \bar{u}}{\partial z}} \underset{III}{-\overline{v'w'}\frac{\partial \bar{v}}{\partial z}} \underset{IV}{+ g\frac{\overline{w'\theta'}}{\bar{\theta}}\left(1+\frac{0.07}{\beta}\right)} + \underset{V}{\frac{1}{\rho}\frac{\partial(\overline{w'p'})}{\partial z}} \underset{VI}{-\frac{\partial(\overline{ew'})}{\partial z}} \underset{VII}{-\varepsilon} \qquad (2.11)$$

Term II and III refer to the production rate of TKE by the mean wind shear; term IV describes the buoyant production (unstable conditions) or consumption (stable conditions) of TKE, term V relates pressure perturbations to the redistribution of TKE, term VI represents the turbulent transport of TKE and term VII stands for the dissipation of TKE into heat. The following restrictions have been made to derive eq. (2.11) from eqs. (2.5-9): Vertical velocity fluctuations are of the same magnitude as the horizontal and vertical gradients are much larger than the horizontal gradients. The factor $(1+0.07/\beta)$ in term IV accounts for the production of convective energy due to water vapor, where β is the Bowen Ratio, the ratio of sensible to latent heat flux at the surface.

In the set of equations for turbulent flow above, the number of unknowns is larger than the number of equations and when we introduce new equations for these unknowns, even more unknowns appear. The higher the order of moments included in the equations, the higher the number of unknown moments will be. This fact is known as the *closure problem*, for any finite set of those equations, the description of turbulence is not closed. It follows that at a certain level of desired complexity (the order of closure), assumptions have to be made about the remaining unknowns. Similarity theory for example can be viewed as a type of zero-order closure. Similarity relationships can be used to diagnose the mean values of wind, temperature, etc. as a function of height without any turbulence closure assumptions to be made, however this implies, that the turbulent fluxes are known. In first order closure the turbulent fluxes are related to mean quantities, this is for example done in K-theory, where the turbulent transport is related to the gradient of the mean by an eddy diffusivity coefficient. The equations of mean and turbulent flow can be simplified by making assumptions about the evolution of the variables or their horizontal variability.

Homogeneity

For turbulent flows, homogeneity means, that the statistics of a variable do not change in space. This does not hold for the vertical direction in the PBL, where the flow is clearly stratified. Homogeneity in the boundary layer therefore means horizontal homogeneity. If homogeneity is given, the partial derivations $\partial/\partial x$ and $\partial/\partial y$ vanish (as in eq.(2.10)). Homogeneity also always refers to the scale of the problem under consideration: very close to the surface, even a flat desert is inhomogeneous, whereas sufficiently far from the ground, even a rough surface like a forest or a city can be considered as homogeneous. As a measure for homogeneity the “required fetch” is introduced. Fetch refers to the upwind distance with the same surface characteristics. If the fetch is large enough, the flow can be considered adapted to the surface and no essential horizontal differences exist.

Stationarity

If the statistics of a variable do not change in time, stationarity is given and hence $\partial/\partial t=0$. Stationarity is therefore homogeneity in time. Due to the diurnal cycle of solar radiation (influencing temperature, humidity and wind) and changing synoptic patterns, stationarity is not given in the boundary layer. However, stationarity can be approached by choosing a suitable averaging time. The spectrum of atmospheric motions shows a pronounced gap at time periods of one hour. Motions at the low frequency side of the gap can be associated with the mean flow, motions right of the gap represent turbulence. Averaging periods of 30 to 60 minutes therefore record the turbulent exchange under approximate stationary conditions.

Isotropy

If the statistics of a flow are invariant to rotation and reflections of the coordinates ($\sigma_u^2=\sigma_v^2=\sigma_w^2$), isotropy is given. Obviously, the flow in the in the PBL for the given averaging times is fully anisotropic. However, the concept of isotropy becomes very important for spectral considerations. The smallest eddies are found to be isotropic in the inertial subrange, which allows a relatively easy description of the spectral densities in this scale. See chapter 2.4 for the concept of atmospheric turbulence spectra.

2.2 The structure of the urban boundary layer

A city consists of building structures of varying material and varying horizontal and vertical length scales. The interaction between this heterogeneous urban surface and the atmosphere modifies the surface layer and produces an urban boundary layer. The turbulent exchange processes will vary strongly both in time and space due to the inhomogeneous physiognomy of a city. At the rural-urban interface, an internal boundary layer is formed, the urban boundary layer (UBL). If the site of consideration is far enough from this transitional region, the former rural boundary layer is completely replaced by the UBL. Within the UBL the roughness sublayer (RS) and the canopy layer (CL) are considerably extended compared to their rural counterparts, whereas the inertial sublayer is reduced or may even vanish. This concept was first presented by Rotach (1999) and is shown in figs. 2.2 and 2.3.

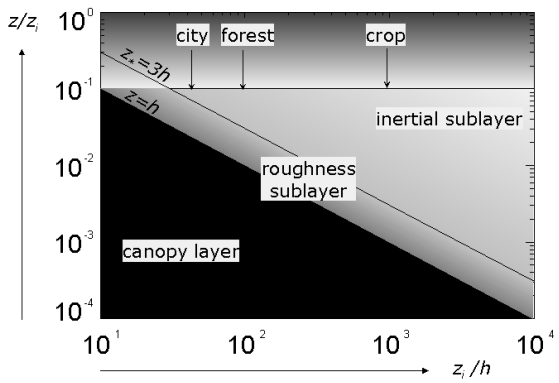

Fig. 2.2: Concept of the sublayers in the UBL, with z_i as mixed layer height and z_* as the height of the roughness sublayer (adapted from Rotach, 1999).

Strictly speaking the conventional methods to describe the characteristics of turbulent exchange of momentum, heat and mass, as developed for smooth, homogeneous surfaces, can not be applied to the urban boundary layer. Due to the lack of better knowledge dispersion- and flow-models still apply the semi-empirical Monin-Obukhov similarity framework (chapter 2.3) for the parameterization of the urban boundary layer. Therefore, the present model calculations are normally based on very simplified methods.

For modeling purposes it is important to know the complex structure of the turbulent characteristics above urban areas and how they compare to the better known values of other surfaces types. The dimensionless variances of the three wind components are of special interest because they play a dominant role in pollution dispersion models.

The properties of urban surfaces strongly affect the local atmosphere. Their aerodynamic roughness and emission of thermal energy act on the wind field. In the lower part, in the urban canopy layer, high levels of turbulence result from pressure patterns formed on the individual buildings and by thermal convection cells.

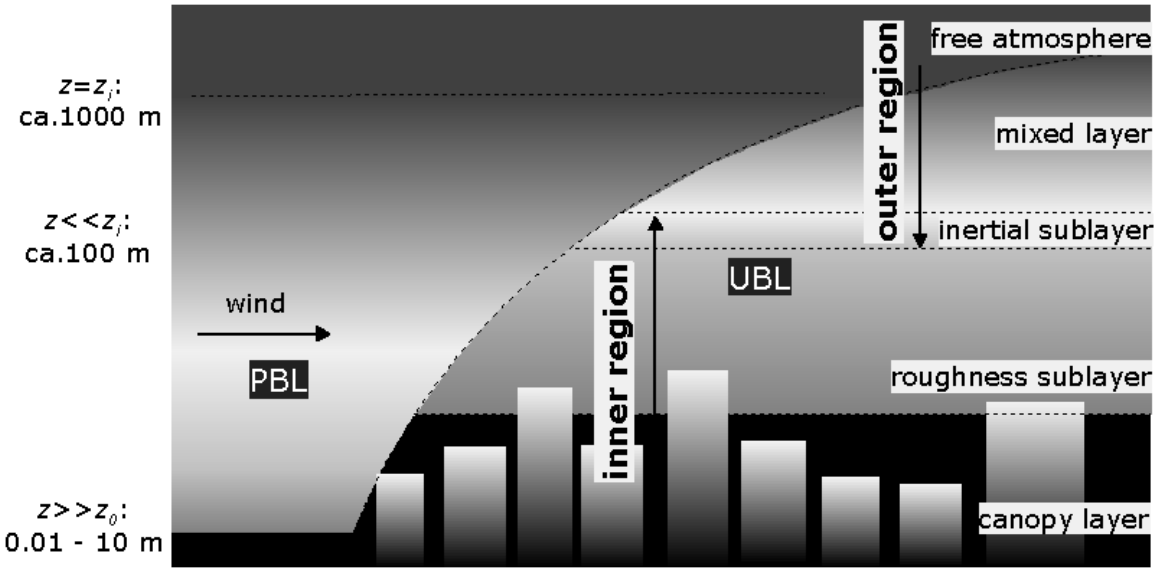

Fig. 2.3: The vertical structure of an urban boundary layer, modified after Oke (1988).

2.3 Similarity theory

Similarity theory provides a useful tool to derive empirical relationships for the variables of interest, if it is not possible to derive laws based on first principles of the governing physics of the turbulent flow. It is based on organizing the variables into dimensionless groups by applying a dimensional analysis called Buckingham Pi theory. A non-dimensionalized variable can then be described by an empirical "universal" function of dimensionless groups of variables, as long as all important variables for the situation studied are taken into account. This universal function works everywhere at all the time for the problem in question.

Four steps have to be performed for developing the empirical relationships (Stull, 1988):

- chose the relevant variables for problem in question
- organize the variables into non-dimensionalized groups
- experimentally determine the values of the dimensionless groups
- describe the relationship between groups by fitting an empirical curve to the data

This four step process results in an empirical equation or a set or curves of a similar shape (hence the name similarity theory).

2.3.1 Monin-Obukhov Similarity

The crucial part of similarity theory is the choice of the relevant variables. This is relatively simple for the surface layer (SL), where the fluxes of momentum, sensible and latent heat are almost constant (variation < 10 %) due to the required conditions for homogeneity and stationarity and a comparison of the order of magnitudes. Equation (2.3) i.e. then reduces to

$$\frac{\partial}{\partial z}\overline{u'w'} \approx 0\,, \tag{2.12}$$

which means, that the coordinate system can always be rotated in a way that $\bar{v} = 0$ and the mean wind vector is described by $\bar{u}$ only (cf. Appendix A.2). The problem is therefore one dimensional for a homogeneous surface.

In their original work from 1958, Monin and Obukhov determined the four relevant variables that govern the turbulent flow in the SL as:

- the height above ground level z. In the case of rough surfaces the reference height is $(z- z_d)$, where z_d is the zero plane displacement height (cf. chapter 4.1)
- the friction velocity u_* to account for production of mechanical turbulence due to friction at the surface
- the kinematic heat flux $\overline{w'\theta'}$ to account for energy exchange at the surface (and production of thermal turbulence)
- the term g/θ to consider for buoyancy effects due to temperature variations, where g stands for earth's gravity acceleration

As a second length scale (beside z), Monin and Obukhov used the well known Monin-Obukhov length (also Obukhov length, introduced first in 1946 by Obukhov) L

$$L = \frac{u_*^2\,\bar{\theta}}{kg\theta_*\left(1+\dfrac{0.07}{\beta}\right)} \tag{2.13}$$

with the scaling variables u_* for velocity and θ_* for temperature (linked to the turbulent fluxes of momentum and sensible heat), namely:

$$u_* = \sqrt{-\overline{u'w'}} = \sqrt{\frac{\tau}{\rho}} \tag{2.14}$$

$$\theta_* = \frac{-\overline{w'\theta'}}{u_*} = \frac{-\left(\dfrac{H}{\bar{\rho}c_p}\right)}{u_*} \tag{2.15}$$

where τ is the surface shear stress and k the von-Karman constant (which was introduced for historical reasons). Note also, that the term $(1+0.07/\beta)$ in eq. (2.13) was introduced later by Lumley and Panofsky (1964) to account for buoyancy effects of water vapor. Since in practice, the lateral flux of momentum does not vanish completely after the coordinate rotation (cf. Appendix A.2), the friction velocity u_* is calculated by

$$u_* = \sqrt[4]{\overline{u'w'}^2 + \overline{v'w'}^2}\,, \tag{2.16}$$

however, differences between eqs. (2.14) and (2.16) are very small.

From the above relationships, a dimensionless group

$$\zeta = \frac{z - z_d}{L} \tag{2.17}$$

can be formed. By the definition of similarity theory, every other parameter describing the turbulent flow in the SL, nondimensionalized by its relevant scaling variable, can now be described by an universal function of ζ, which is independent on the surface, height, velocity, etc.

When $z\text{-}z_d$ is small compared to L, mechanical turbulence dominates. For $(z\text{-}z_d) > |L|$, buoyancy effects become more important. ζ therefore indicates the relative importance of mechanical and thermal effects, thus ζ and L are also a measure for the stability of the stratification of the atmosphere similar to the gradient Richardson number Ri or the bulk Richardson number Rf, which are defined as follows:

$$Ri = \frac{g}{\overline{\theta}} \frac{(\partial \overline{\theta} / \partial z)}{(\partial \overline{u} / \partial z)^2} \tag{2.18}$$

$$Rf = \frac{g}{\overline{\theta}} \frac{\overline{w'\theta'}}{\overline{u'w'}(\partial \overline{u} / \partial z)^2} \tag{2.19}$$

The relations between these common stability parameters are given in tab.2.1.

Tab. 2.1: Relationship between stability parameters

stability	*Ri, Rf, ζ*	*L*
unstable	< 0	< 0
neutral	= 0	$\rightarrow \pm \infty$
stable	> 0	> 0

The gradients of velocity and temperature, nondimensionalized by $k(z\text{-}z_d)/u_*$ can be written as an universal function of ζ, namely:

$$\frac{k(z - z_d)}{u_*} \frac{\partial \overline{u}}{\partial z} = \phi_M(\zeta) \tag{2.20}$$

$$\frac{k(z - z_d)}{\theta_*} \frac{\partial \overline{\theta}}{\partial z} = \phi_H(\zeta) \tag{2.21}$$

If the right-hand side is set to unity, eq. (2.20) is the familiar differential equation of the logarithmic wind profile for neutral conditions, thus the universal functions $\phi_M = \phi_H = 1$ and $(z\text{-}z_d)/L = 0$ for neutral stratification. Businger et al. (1971) presented the well established semi-empirical relationships for ϕ_M and ϕ_H such as:

$$\phi_M = (1 - 16\zeta)^{-1/4} \tag{2.22}$$

and

$$\phi_H = (1 - 16\zeta)^{-1/2} \tag{2.23}$$

for unstable conditions with $\zeta < 0$, and

$$\phi_M = \phi_H = (1 + 5\zeta) \tag{2.24}$$

for stable conditions with $\zeta > 0$.

In the same way, similarity theory predicts the variances of the turbulent fluctuations, usually considered in terms of the standard deviations $\sigma_{u,v,w,\theta}$ and normalized appropriately by u_* and θ_* in the general form (after de Bruin et al., 1993)

$$\frac{\sigma_x}{x_*} = f_x(\zeta) \tag{2.25}$$

where x stands for u, v, w and θ and x_* is the respective scaling variable (u_* for velocity and θ_* temperature). For unstable conditions, eq. (2.25) becomes (Panofsky and Dutton, 1984)

$$f_x(\zeta) = \pm c_{x1}(1 - c_{x2}\zeta)^{\pm 1/3} \tag{2.26}$$

with the empirical constants c_{x1} and c_{x2} . With $\zeta \rightarrow -\infty$, eq. (2.26) passes over to

$$f_x(\zeta) \rightarrow \pm c_{fx}(\zeta)^{\pm 1/3}, \tag{2.27}$$

the prognostic equation for free convection (Wyngaard et al., 1971). The (+)-sign in the above equations is valid for the wind fluctuations u, v, w, the (-)-sign is valid for temperature fluctuations θ.

For stable conditions,

$$\frac{\sigma_x}{x_*} = c_{sx} \tag{2.28}$$

holds, which implies, that the nondimensionalized standard deviations are constant and similar to the neutral limit of eq.(2.26). The empirical constants in Tab. 2.2 (adapted from Wyngaard et al., 1971, Tillman, 1972 and Panofsky and Dutton, 1984) have been used as a reference in this work.

Many authors have verified the above relationships and the empirical constants by experimental measurements, though the scatter of data points among the various investigations is large. This is mainly due to non standard measuring techniques of the fluxes, the vertical variation of these parameters in the SL, variations in sampling time and possibly the influence of mesoscale circulation features.

Tab. 2.2: Empirical constants for MOS-relationships

constant		constant	
$c_{\theta 1}$	2.9	$c_{f\theta}$	0.95
$c_{\theta 2}$	28.4	c_{fw}	1.8
c_{w1}	1.25	$c_{s\theta}$	2
c_{w2}	3	c_{sw}	2.5

2.4 Spectral analysis

If stationarity is fulfilled, a turbulent time series can be analyzed as a function of time *f(t)* as well as a function of frequency $\hat{f}(\omega)$. Fourier transformation is the tool to get from one domain to the other. Both can be looked at as an equivalent consideration of the same property.

$$\hat{f}(\omega) = \int_{-\infty}^{\infty} f(t) e^{i\omega t} dt \tag{2.29}$$

$$f(t) = \frac{1}{2\pi} \int_{-\infty}^{\infty} \hat{f}(\omega) e^{-i\omega t} d\omega$$

In atmospheric turbulence research we are mainly interested in frequencies of the turbulent fluctuations (eddies) contributing to the total turbulence. In the case of turbulence, the spectral density *S(n)* is the contribution of a single frequency *n* to the total variance of the spectrum, thus the spectrum gives us a idea of how much of the variance of a time series is associated with a particular frequency. For stationary conditions the spectral density $S_x(n)$ of any given property *x* corresponds to the total variance of the Fourier transformed time series. See i.e. Stull (1988), Eugster (1994) or Panofsky and Dutton (1984) for a comprehensive derivation of this relation:

$$\overline{x'^2} \equiv \sigma_x^2 = 2 \int_0^{\infty} S_x(n) dn \tag{2.30}$$

The coherence between the frequency and the size of an eddy in turbulent flows is given by Taylor's 'frozen turbulence' hypothesis. It says that turbulence can be considered as 'frozen' in the case where the turbulent eddies evolve with a timescale longer than the time it takes the eddy to be advected past a sensor. The high frequency part of turbulence spectra mostly fulfills this condition and the following equation holds for frequency *n,* wavelength λ and the horizontal velocity $\overline{u}$ of an eddy:

$$\lambda = \frac{\overline{u}}{n} \tag{2.31}$$

To compare turbulence spectra from different conditions it is convenient to use a normalized frequency *f* for plotting the spectra, where *f* is defined as

$$f = \frac{n(z - z_d)}{\overline{u}}. \tag{2.32}$$

The nature of atmospheric turbulence spectra is directly related to the fact, that production and dissipation are not occurring at the same scales. Production is feeding only the large size eddies (at low frequencies), whereas dissipation is happening only at the high frequency end of the spectrum. This means, that the rate of transport across the middle part of the spectrum equals the rate of dissipation ε. This transfer is considered as taking place inertially, there is neither production nor dissipation. This concept is also known as the energy cascade which was captured by Lewis Richardson in his famous poem ('big whorls....'). Therefore, all turbulence spectra can be subdivided in three main parts:

1. Energy containing range

   Production of energy by buoyancy and mechanical shear

2. Inertial subrange

   Characteristic timescale is the 'Kolmogorov microscale'. Based on Kolmogorov (1941), Kaimal et al. (1972) showed, that Kolmogorov's hypothesis is applicable also to experimental data, which finally gives us the base for modeling turbulence spectra. The spectral density in this range is proportional to f^x.

3. Dissipation range

   Turbulent energy is dissipated into molecular oscillation.

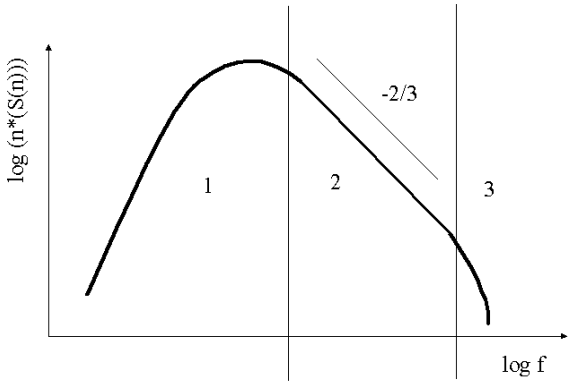

Fig. 2.4: Schematic turbulence spectrum with: 1) energy containing range, 2) inertial subrange and 3) dissipation range (adapted from Kaimal and Finnigan, 1994).

2.4.1 Data processing for spectral analysis

Time series of 53 minutes (2^{16} samples at 20.83 Hz) have been chosen for spectral analysis to minimize the amount of time for the spectra calculation. Four steps are performed before calculating the spectra:

- Correction for possible non-stationarities by linear detrending
- Rotation of the coordinate system around the z-axis such that the x-axis is aligned with the mean wind direction. ($\overline{v}$ = 0, see Appendix A.3).
- Rotation of the coordinate system in the x-y plane, such that the mean vertical wind becomes zero ($\overline{w}$ = 0, see Appendix A.3).
- Tapering with a cosine taper to eliminate edge effects prior to the discrete Fourier transformation (Stull, 1988; Kaimal and Finnigan, 1994).
- Calculation of FFT-spectrum
- Averaging raw FFT-spectrum into 20 logarithmically spaced frequency classes (0.0004..8.3 Hz).

Composite spectra have been formed for velocity and temperature fluctuations and momentum and sensible heat flux. Due to normalization of the spectra (spectral density *S(n)* by *n/(co)variance* and frequency *n* by $(z\text{-}z_d)/\overline{u}_z$), the single spectra are comparable to each other and averaged composite spectra can be calculated. This is done by processing the following steps:

- Normalization of the spectral density *S*(*n*) by *n*/(*co*)*variance*
- Normalization of the frequency *n* by $(z\text{-}z_d)/\overline{u}_z$
- Interpolating (fit) the single spectra by a cubic spline
- Averaging the fitted curves into a defined set of 20 logarithmically spaced non-dimensional frequency classes (ranging from 0.0015..380) with consideration of the stability

This procedure finally results in the composite spectra shown in chapter 4.4.

A general remark concerning the conventional way of computing and plotting atmospheric turbulence spectra must be made: Since the usual plot of atmospheric turbulence spectra is double logarithmic, the classes for averaging the single spectra are logarithmically spaced. This results in fewer values to be averaged into low-frequency classes than at the high-frequency end, which causes the spectra to look sometimes very jagged at the low-frequency end. Kaimal and Finnigan (1994) suggested the so called spectral slicing method to smooth the spectra as well at the low-frequency as at the high-frequency part: time series are subdivided into *N* non-overlapping blocks of equal length for the calculation of *N* single high-frequency spectra, which then will be averaged to obtain an averaged spectrum for the high-frequency part. This minimizes the influence of single spikes in the time series. The low frequency part of the spectrum is formed by block averaging the original time series (simulating a lower sampling rate) and then compute the spectrum. Both, high- and low-frequency spectra are then averaged into logarithmically spaced frequency bands such that an overlapping region of bands at the transition from low- to high-frequency spectra exists. See Kaimal and Finnigan (1994), Mazzoni (1996) or Eugster (1994) for a detailed description of the procedure. Figure 2.4 shows the effect of frequency smoothing, spectral slicing and tapering of an arbitrarily chosen raw spectrum.

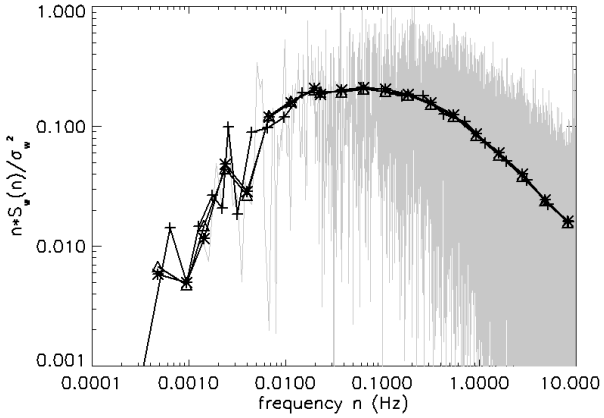

Fig. 2.5: Arbitrarily chosen spectrum of vertical velocity component. Light gray: raw spectrum, (+) frequency smoothing (spectrum averaged into 20 bands), (*) spectral slicing (spectrum composed from high-frequency and low-frequency spectrum), (Δ) tapered spectrum with spectral slicing.

2.5 Quadrant analysis

It has to be taken in mind, that the term „conditional sampling“ describes a broad class of methods for analyzing turbulence time series. The goal is always to extract information about postulated events or patterns of coherent motion by detecting the events and to assign each realization a time origin (i.e. the edge of a ramp structure). Next, an ensemble-averaged pattern of the detected events is produced, which gives the possibility to determine the contribution of the coherent motions to overall turbulent fluxes like $-\overline{u'w'}$ or $\overline{w'\theta'}$. According to the detection scheme, four categories of conditional analysis can be distinguished:

- Quadrant analysis (Wallace et al., 1972) classifies *u'w'* (or *w'θ'*) into four quadrants in the *(u',w')*-plane and provides information about the contributions of ejections and sweeps to the total flux, however, it says nothing about the characteristic patterns of the turbulent flow.
- Visual event detection
- Automated detection algorithms for sharp changes in turbulence signals
- Event detection based on wavelet transforms

In this section, the theory of quadrant analysis is described, for wavelet analysis refer to chapter 2.6.

The mean rate of downward diffusion of longitudinal momentum is represented by the kinematic Reynolds stress $-\overline{u'w'}$. Additional information about the diffusion process is provided by sorting the instantaneous values of *u'* and *w'* into four categories according to the sign of the fluctuating components. The quadrants in the *(u',w')*-plane are numbered conventionally and named after Shaw et al. (1983) as follows:

- quadrant 1: $u' > 0$, $w' > 0$ outward interaction
- quadrant 2: $u' < 0$, $w' > 0$ ejection or burst
- quadrant 3: $u' < 0$, $w' < 0$ inward interaction
- quadrant 4: $u' > 0$, $w' < 0$ sweep or gust

Quadrants 1 and 3 both represent upward transfer, while quadrants 2 and 4 represent contributions to downward diffusion of momentum. By introducing a hyperbolic hole *H* as a region in the *(u',w')*-plane, where instantaneous values of *u'w'* are smaller than $H \cdot \left|\overline{u'w'}\right|$, and increasing *H* progressively, the small and frequent contributions to Reynolds stress are excluded from the analysis and the incidence of events exhibiting large values of *u'w'* can be determined easily within each quadrant.

The fraction of the flux outside hole *H* in quadrant *i* is then defined as

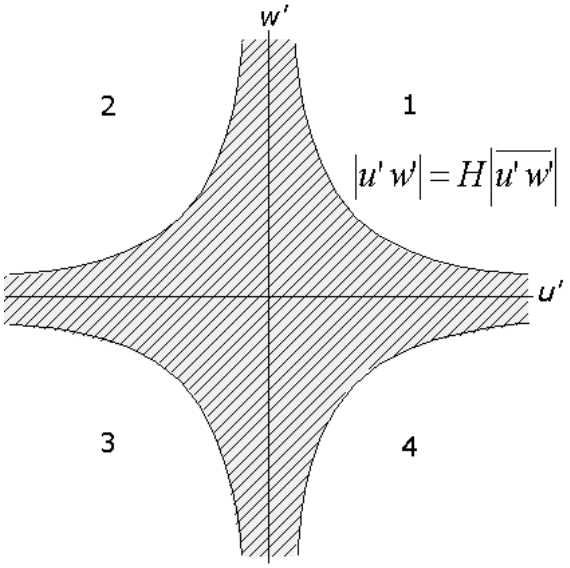

Fig 2.6: The concept of quadrant analysis and the definition of the hyperbolic hole *H*. Adapted from Shaw et al. (1983).

$$S_{i,H} = \frac{\langle u'w' \rangle_{i,H}}{\overline{u'w'}}, \tag{2.33}$$

where angle brackets $\langle ... \rangle$ denote a conditional average

$$\langle u'w' \rangle_{i,H} = \lim_{T \to \infty} \frac{1}{T} \int_0^T u'(t) w'(t) I_{i,H}(t) dt \tag{2.34}$$

with

$$I_{i,H} = \begin{cases} 1 & \text{if } (u'w') \text{ is in quadrant } i \\ & \text{and } |u'w'| \geq H|\overline{u'w'}| \\ 0 & \text{otherwise} \end{cases} \tag{2.35}$$

It follows from the definition of the flux fraction in eq. (2.33), that $\sum_{i=1}^{4} S_{i,0} = 1$. In addition, the time fraction $T_{i,H}$ for any contribution $S_{i,H}$ is

$$T_{i,H} = \lim_{T \to \infty} \frac{1}{T} \int_0^T I_{i,H}(t) dt, \tag{2.36}$$

i.e., $T_{2,H}$ and $T_{4,H}$ are total sweep and ejection durations for hole size *H*, respectively. $T_{i,H}$ can also be viewed as the ratio of the total duration of events in quadrant *i* to the sampling period *T*. Note that for scalar transport (i.e. *w'θ'*), quadrants 1 and 3 refer to ejections and sweeps, respectively.

From the stress fractions $S_{i,H}$, two measures of the relative importance of sweeps and ejections can be defined: The difference ΔS_H

$$\Delta S_H = S_{4,H} - S_{2,H} \tag{2.37}$$

or their respective ratio

$$\gamma_H = \frac{S_{2,H}}{S_{4,H}}. \tag{2.38}$$

Furthermore, Shaw et al. (1983) introduce exuberance E as the ratio of uncorrelated (upward) to organized (downward) contributions to the total momentum flux, say

$$Ex = \frac{S_{1,0} + S_{3,0}}{S_{2,0} + S_{4,0}}. \tag{2.39}$$

Quadrant analysis has been applied by numerous authors over a wide range of canopies: Finnigan (1979) (wheat crop), Raupach (1981) (wind tunnel), Shaw et al. (1983) (Zea mays L.), Raupach (1981) (wind tunnel) (1983), Bergström and Högström (1982) (pine forest), Maitani & Shaw (1990) (deciduous forest), Chen (1990) (mallee bushland), Katul et al. (1997) (tall natural grass, bare soil). Rotach (1993a) and Oikawa and Meng (1995) (both urban). A general conclusion of all these studies is the dominance of gusts over burst within and close above the canopy, where as in the high roughness sublayer and surface layer, bursts contribute most to the momentum transport. The relative contribution of gusts increases both with surface roughness and with proximity to the canopy top from both sides. Only a few studies analyze the sensible heat flux by means of quadrant analysis and practically no distinction of stability classes has been considered until now. In this study, the fluxes of momentum and sensible heat are investigated by the means of quadrant analysis with consideration of the different stability conditions (chapter 4.3) and compared to the results of the studies mentioned above

.

2.6 Wavelets

During the past ten years, wavelet transforms have been formalized into a rigorous mathematical framework for signal and image processing among others. It has become a common analysis tool in geophysics. An increasing number of papers dealing with the subject of atmospheric turbulence and wavelets have been published since 1991, when Farge (1992) and Meneveau (1991) established the wavelet transform in turbulence research. A comprehensive description of applications in geophysics is given in Foufoula-Georgiou and Kumar (1994). Several textbooks exist that treat the wavelet analysis theoretically, from which a few shall be mentioned here: Daubechies (1992), Holschneider (1995) and Wickerhauser (1993).

The continuous wavelet transform is an attractive tool for decomposing a time series into time-frequency space, which gives the opportunity to determine both the dominant modes of variability and how these modes vary in time. This is in contrast to the Fourier transform, which has been so far the dominant technique used in processing data sets provided by fast response wind and temperature sensors. The Fourier transform is strictly localized in frequency and so it is not well-suited to investigate intermittent processes like atmospheric turbulence, because all temporal information is lost. Hence, it is a „global“ transform. The wavelet transform is characterized as a „local“ transform because the transform coefficients are only influenced by a portion of the signal around the point defined by the translation parameter. Thus the wavelet transform is able to detect isolated events and preserve information about their occurrence time and characteristic feature.

In this chapter, a basic introduction to wavelets is given, followed by a review of the related literature concerning atmospheric turbulence and a overview of the work done since. A methodic part shows the analytic possibilities of the wavelet transform for event detection event detection, which are used in this study. The results of wavelet analysis of the data related to this work are presented in chapter 4.5.

2.6.1 Basics

The continuous wavelet transform $W(s,\tau)$ of a real square integrable signal $f(t)$ with respect to an analyzing wavelet $\psi(t)$ can be defined as

$$W(s,\tau) = \frac{1}{s}\int_{-\infty}^{+\infty} f(t)\psi\left(\frac{t-\tau}{s}\right)dt = \frac{1}{s}\int_{-\infty}^{+\infty} f(t)\psi_{s,\tau}(t)dt \tag{2.40}$$

where s is a scale dilation and τ a position translation. In Fourier space, using Parseval's theorem, Eq. (2.40) can be written as

$$W(s,\tau) = \frac{1}{s}\int_{-\infty}^{+\infty} \hat{f}(\omega)\hat{\psi}^{*}(s\omega_{\tau})d\omega = \frac{1}{s}\int_{-\infty}^{+\infty} \hat{f}(\omega)\hat{\psi}^{*}_{s,\tau}(\omega)d\omega \tag{2.41}$$

where the asterix indicates the complex conjugate and „^„ stands for the Fourier transform of a function given by

$$\hat{f}(\omega) = \frac{1}{2\pi}\int_{-\infty}^{+\infty} f(t)e^{-i\omega t}dt \tag{2.42}$$

The continuous wavelet transform can be viewed as a numerical microscope whose optics, magnification and position are given by $\psi(t)$, s and τ, respectively, in fact, it is the convolution of $f(t)$ with a scaled and translated version of a wavelet function $\psi(t)$.

A wavelet ψ is defined as a real or complex valued function of a real variable that must have zero mean and be localized in both time (t) and frequency space (ω), this means the following two integrals have to converge:

$$E = \int_{-\infty}^{+\infty} |\psi(t)|^2 dt \tag{2.43}$$

$$C_{\psi} = 2\pi\int_{-\infty}^{+\infty} \frac{|\hat{\psi}(\omega)|^2}{\omega}d\omega \tag{2.44}$$

From eq. (2.43) it follows, that ψ has finite energy. Equation (2.44) implies, that ψ has a zero mean with its Fourier transform around the zero frequency limited. This is called the admissibility condition (Farge, 1992) and C_{ψ} is the admissibility parameter, which is scale independent and constant for each wavelet function.

As a consequence of the admissibility condition in eq. (2.44), the wavelet transform as a bandpass filter with a known response function (namely the wavelet function) is invertable and it is possible to reconstruct the original time series using the following equation:

$$f(t) = \frac{1}{C_\psi} \int_{-\infty}^{+\infty} \int_{0}^{+\infty} W(s,\tau) \frac{1}{s^2} \psi(s\omega t) ds d\tau \quad (2.45)$$

The wavelet transform is also energy preserving so that it follows, that the total energy E_f of a function *f(t)* can be written as

$$\begin{aligned} E_f &= \int_{-\infty}^{+\infty} |f(t)|^2 dt = \int_{-\infty}^{+\infty} \left|\hat{f}(\omega)\right|^2 d\omega \\ &= \frac{1}{C_\psi} \int_{0}^{+\infty} \frac{ds}{s} \int_{-\infty}^{+\infty} |W(s,\tau)|^2 d\tau \end{aligned} \quad (2.46)$$

Eq. (2.46 correlates the spectral energy density (also referred to as Fourier or energy spectrum) $E_f(\omega) = \left|\hat{f}(\omega)\right|^2$ to the so called wavelet variance

$$E_W(s) = \int_{-\infty}^{+\infty} |W(s,\tau)|^2 d\tau \,. \quad (2.47)$$

In other words, $E_W(s)$ is the energy of a function *f(t)* at scale *s* and is sometimes also referred to as wavelet scalogram. Thus the coherence between Fourier spectrum and wavelet spectrum is given by

$$E_W(s) = 2 \int_{-\infty}^{+\infty} E_f(\omega) E_{\psi_s}(\omega) d\omega \,, \quad (2.48)$$

i.e., $E_W(s)$ is the Fourier spectrum of *f(t)* averaged by the Fourier spectrum of the bandpass filter (the wavelet function) ψ_s at scale *s*. See Perrier et al. (1995) for an comprehensive theoretical discussion of the comparison between Fourier and wavelet spectra.

The wavelet transform conserves not only the energy of a function, but also the inner product of two functions. So just as the wavelet variance is correlated to the Fourier spectrum, one can define a wavelet covariance as an equivalent of a Fourier cross-spectrum of two functions *f(t)* and *g(t)* as

$$E_{W_{f,g}}(s) = \int_{-\infty}^{+\infty} W_f(s,\tau) W_g^*(s,\tau) d\tau \quad (2.49)$$

with W_f and W_g as the wavelet transforms of the two functions *f(t)* and *g(t)*. In analogy to the Fourier cross-spectrum, one is able to define a wavelet cospectrum and quadrature spectrum as the real and the imaginary part of eq. (2.49), respectively, a wavelet amplitude spectrum as the absolute value of the cross-spectrum and a phase spectrum from the ratio of quadrature spectrum and cospectrum.

If we use nonorthogonal wavelets (as is the case in this study), we have to consider the redundancy of the information from the continuous wavelet transform. The similarity of wavelets with adjacent values of *s* in the time-representation must provide the same kind of information from one scale to another, whereas, in the frequency space, the broad peaks may interfere from one scale to another. In other words, a particular wavelet coefficient contains information about its neighbours in the (s, τ) plane. To quantify this redundancy, one has to study the properties of $\left|\psi_{s,\tau}(t)\right|^2$ and $\left|\hat{\psi}_{s,\tau}(\omega)\right|^2$, and specifically their standard deviations. As a consequence of eq. (2.44), $\hat{\psi}_{s,\tau}(\omega = 0) = 0$, and therefore, the center $\omega^0_{\hat{\psi}_{s,\tau}}$ of a bandpass filter $\psi_{s,\tau}(t)$ is located away from the origin $\omega = 0$ and can be determined as the center of mass for $\omega > 0$ by

$$\omega^0_{\hat{\psi}_{s,\tau}} = \frac{\int_0^\infty \omega \left|\hat{\psi}_{s,\tau}(\omega)\right|^2 d\omega}{\int_0^\infty \left|\hat{\psi}_{s,\tau}(\omega)\right|^2 d\omega} \quad (2.50)$$

and its standard deviation $\sigma_{\hat{\psi}_{s,\tau}}$ as

$$\sigma_{\hat{\psi}_{s,\tau}} = \left(\int_0^\infty (\omega - \omega^0_{\hat{\psi}_{s,\tau}})^2 \left|\hat{\psi}_{s,\tau}(\omega)\right|^2 d\omega \right)^{\frac{1}{2}} \quad (2.51)$$

Similarly, the localization in the time domain $t^0_{\psi_{s,\tau}}$ is given by

$$t^0_{\psi_{s,\tau}} = \frac{\int_{-\infty}^\infty t \left|\psi_{s,\tau}(t)\right|^2 dt}{\int_{-\infty}^\infty \left|\psi_{s,\tau}(t)\right|^2 dt} \quad (2.52)$$

and analogous its standard deviation $\sigma_{\psi_{s,\tau}}$ by

$$\sigma_{\psi_{s,\tau}} = \left(\int_0^\infty (t - t^0_{\psi_{s,\tau}})^2 \left|\psi_{s,\tau}(t)\right|^2 dt \right)^{\frac{1}{2}} . \quad (2.53)$$

From eqs.(2.50 –2.53) the following relationships can be derived:

$$\sigma_{\psi_{s,\tau}} = s \sigma_{\psi_{1,0}} \quad (2.54)$$

$$\sigma_{\hat{\psi}_{s,\tau}} = \frac{\sigma_{\hat{\psi}_{1,0}}}{s} \quad (2.55)$$

$$\omega^0_{\hat{\psi}_{s,\tau}} = \frac{\omega^0_{\hat{\psi}_{1,0}}}{s} \quad (2.56)$$

Therefore, an increased resolution in the time domain for the time localization of high frequency components comes with the cost of an increased uncertainty in the frequency localization and vice-versa. Equation (2.56) gives the relationship between the wavelet scale *s* and the equivalent Fourier period or frequency. To illustrate the above relationships, the resolution cells of the wavelet transform for certain points in the phase space are shown qualitatively in fig. 2.7.

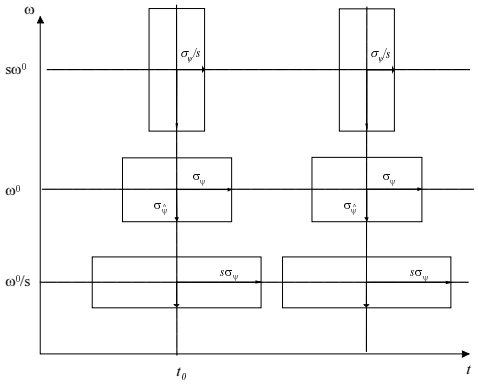

Fig. 2.7: Phase-space representation using the wavelet transform (adapted from Kumar and Fourfoula, 1994).

2.6.2 Wavelet applications in atmospheric turbulence research

In the following section, an overview on some important contributions of wavelet applications in atmospheric turbulence shall be given. However, there is no claim to completeness, since a large amount of papers dealing with the subject have been published in the last years. Most of the authors mentioned below have also published several papers with similar contents, which are not cited in the following.

One of the most important applications of wavelets in atmospheric turbulence research is the detection of the organized structures that rule the flow within and above a canopy. In consequence, it is possible to construct averaged patterns of the dynamics of turbulent transport processes and analyze the contributions of the coherent motions to momentum and heat fluxes for instance. Turbulent transport within and above a canopy is dominated to a large extent by large-scale intermittent coherent structures. These structures are known as periodic ramp patterns in time series of scalars (i.e. temperature) or, in a more general point of view, as occasional large amplitude excursions from the mean on time series of turbulent variables (Paw U et al., 1992). They are characterized by cycles of ‘sweeps’ (‘gusts’) and ‘ejections’ (‘bursts’), which have been observed over a wide range of canopies (Gao et al., 1989; Bergström and Högström, 1989; Paw U et al., 1992, Katul et al., 1997). In fact, the ejection-sweep sequence appears to be a general feature of all wall bounded flows (see also chapter 2.5).

In the study of Collineau and Brunet (1993a, 1993b), the advantages of wavelet transform algorithms for jump detection compared to other methods like the Variable Interval Time-Averaging (VITA) method (i.e. Shaw et al., 1989) or the Window Averaged Gradient (WAG) (Bisset et al., 1990) technique is demonstrated on a forest canopy data set. Using the so called Mexican hat wavelet, a second derivative-like wavelet (a twice-differentiated Gaussian), jump detection only involves identification of zero-crossing points with a particular slope sign depending on the slope of the jumps. VITA, WAG and wavelet detection functions using first derivative-like wavelets (i.e. the Haar wavelet) require the use of a threshold to select the larger peaks in the detection function, this means, these methods have to be calibrated against a reference for each analyzed run. For an extended data set like the one analyzed in this study, the zero-crossing method provides an admittedly tool for the isolation of organized motions. Additionally, the wavelet transform as an alternative to the Fourier spectral analysis also can be used to determine the characteristic time scales of the organized structures as shown by Collineau and Brunet (1993b). One year later, Brunet and Collineau (1994) applied the same method to a maize canopy data set.

Hagelberg and Gamage (1994a, 1994b) presented a technique based on a non-orthogonal wavelet transform to provide a signal decomposition which preserves coherent structures. Embedded within this technique were a coherent structure detection mechanism, an analysis of intermittency resulting in a intermittency index, and filtering techniques. An other decomposition method was presented by Howell and Mahrt (1994) using the Haar wavelet. They partitioned the turbulence time series into four modes of variations: a mesoscale mode, a large eddy scale mode, a transporting eddy mode and a fine scale mode, using a variable cutoff scale to separate the transport mode from the fine scale mode.

Hudgins et al. (1993) was one of the first papers that presented a (cubic spline) wavelet cross scalogram of atmospheric turbulence data to visualize the highly intermittent features of the momentum flux field. He also emphasizes the advantages of the better resolution of low frequency variations in wavelet spectra compared to Fourier spectra. Katul

and Parlange (1994a, 1995) used the orthonormal wavelet transform to analyze the role of temperature and heat fluxes in surface-layer turbulence by wavelet spectra. In their 1994 study, Katul et al. (1994b) investigated power-law deviations from the classical Kolmogrov theory in the inertial subrange using a conditional sampling scheme based on an orthonormal wavelet representation.

Handorf and Foken (1997) analyzed the turbulent exchange processes over the Antarctic shelf-ice. They determined the contribution of large scale eddies to the total turbulent flux of sensible heat by conditional sampling based on wavelet analysis.

As one can see, the analysis of turbulence time series by the means of wavelet transforms has become an important alternative to the well established spectral Fourier analysis during the last 5 years. But it has to be stated, that in most studies, only a few runs of data are analyzed, so they have to be considered rather as methodological studies than a complete analysis. However, this studies show, that wavelet analysis is a promising tool to get more insight in the nature of turbulence concerning coherent structures and their dominant time scales.

2.6.3 The method

Wavelet analysis in this study was done using the continuous wavelet transform according to the really practical guide to wavelet analysis given in Torrence and Compo (1998). Because in practice, we operate with finite time series f_n, the above equations for the continuous wavelet transform have to be modified for a discrete sequence f_n. Equation (2.40) then becomes

$$W_n(s) = \sum_{n'=0}^{N-1} x_{n'} \psi^* \left[\frac{(n'-n)\delta t}{s} \right], \qquad (2.57)$$

in other words, a variation of wavelet scale s and a translation along the localized time index n, or according to eq. (2.41) in Fourier space

$$W_n(s) = \sum_{k=0}^{N-1} \hat{x}_k \hat{\psi}^*(s\omega_k) e^{i\omega_k n \delta t} \qquad (2.58)$$

where the angular frequency ω_k is defined as

$$\omega_k = \begin{cases} \dfrac{2\pi k}{N\delta t} & : \; k \le \dfrac{N}{2} \\ -\dfrac{2\pi k}{N\delta t} & : \; k > \dfrac{N}{2} \end{cases} \qquad (2.59)$$

and $k = 0...N\text{-}1$ is the frequency index. Using eq.(2.58) and a standard Fourier transform routine, the continuous wavelet transform for a given scale s can be computed at all n simultaneously and very efficiently. See Torrence and Compo (1998) for a closer look at the properties of the continuous wavelet transform on discrete time series, like i.e. normalization and reconstruction.

The Mexican hat wavelet, a second derivative of a Gaussian, is shown in fig. 2.8 in the time domain as well as in the Fourier domain. This wavelet is used for all transforms in this study for reasons addressed in the next section. It can be seen that a change of the scale dilation s causes an expansion for $s > 1$ and a contraction for $s < 1$ of the analyzing wavelet function in the time domain and the contrary in the frequency domain.

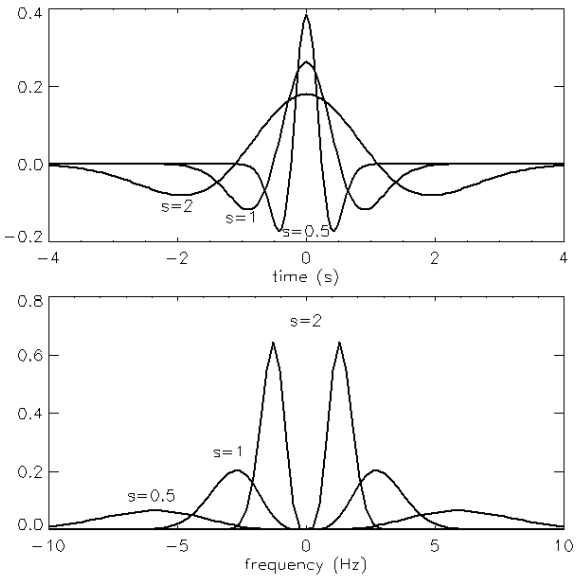

Fig. 2.8: The Mexican hat wavelet in the time (top) and frequency (bottom) domain.

A simple example shall demonstrate the capabilities of the wavelet transform on a artificial data set before applying to real data.

To demonstrate the jump detection purposes of the Mexican hat wavelet („jump“ means a sharp decrease or increase in the signal), the wavelet transform has been applied to a signal of idealized ramps. The ramp time series consists of 6 irregularly spaced ramps shown in fig. 2.9. The ramps have a duration time of 100 and 25 seconds, respectively, and the sampling time interval is supposed to be 1 second.

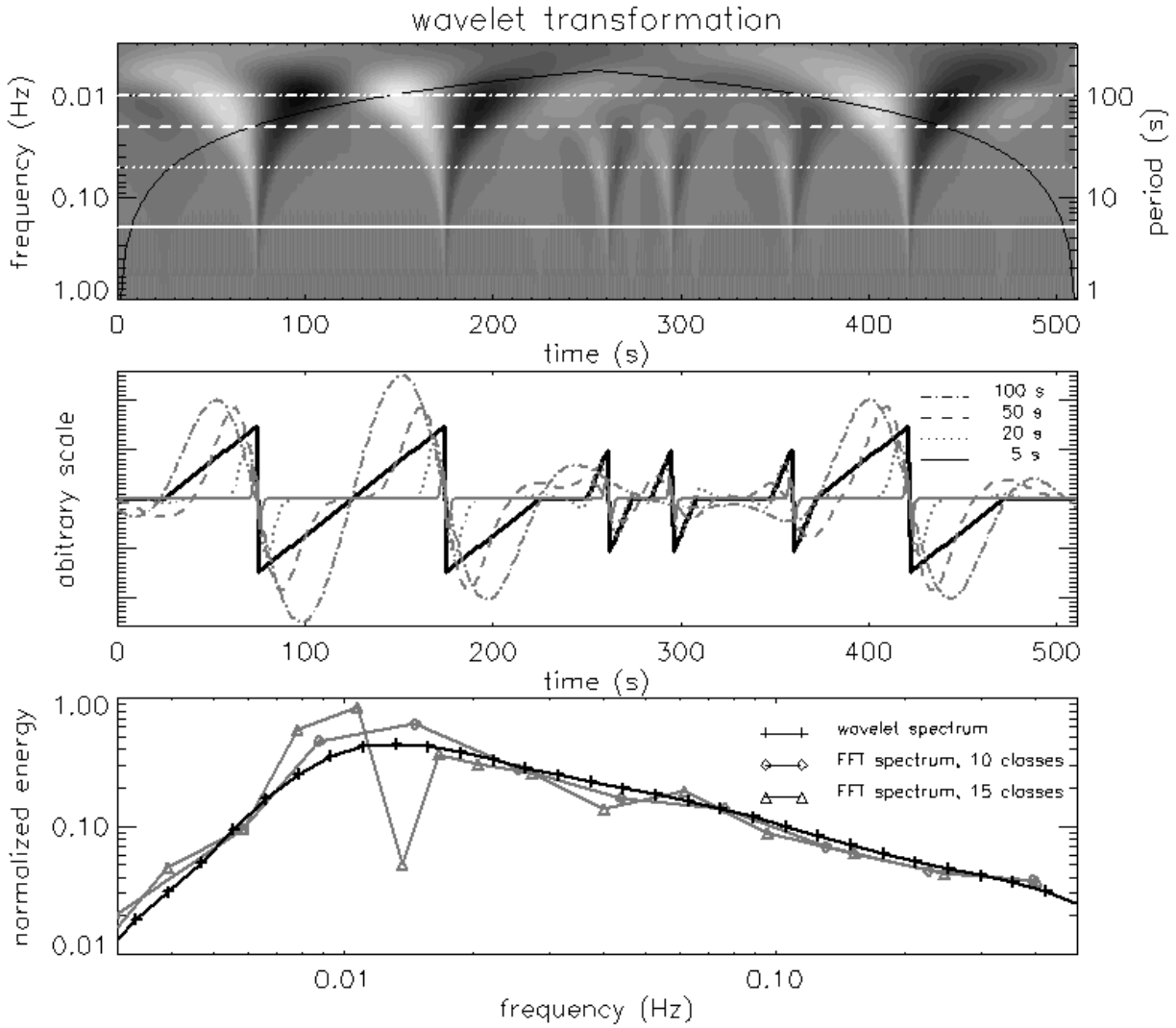

Fig. 2.9: Wavelet transform (top) of the artificial ramp time series (middle, solid line). Cross sections (grey) of the wavelet transform (the wavelet coefficients) for scales corresponding to periods of 5 (solid), 20 (dotted), 50 (dashed) and 100 seconds (dashed-dotted) are shown in the middle. The plot at the bottom shows the wavelet spectrum (+) and two Fourier spectra with a different number of classes for frequency smoothing (◊: 10 classes, Δ: 15 classes).

The wavelet coefficients for the different scales show zero-crossovers at the exact times when jumps occur (fig. 2.9, middle), although a certain scale dependence can be observed. It is obvious that if the scale *s* overrides the characteristic duration of the ramp, the zero-crossover does not any more represent precisely the time of the sharp decrease (the „jump“) in the time series. Therefore, it is important to evaluate the characteristic timescale of the event of interest before the detection algorithm is applied. This is done by analyzing the wavelet variance (or spectrum) according to eq. (2.47).

It is expected that the wavelet spectrum exhibits a peak at the scales that contribute most to energy of the input signal, in analogy to Fourier spectra. For our ramp time series, the peak should occur at frequencies that correspond to a time scale slightly lower than 100 seconds. Indeed, this is the case in fig. 2.9 (bottom), where the wavelet spectrum as well as the Fourier spectrum of the ramp time series is shown. They both peak in the range of 0.01 and 0.015 Hz, which corresponds to a time-scale of 100..66 s. This is also a good example for the advantages of wavelet spectra compared to Fourier spectra, which has also been mentioned earlier in this chapter. The wavelet spectrum appears much smoother in the low frequency part and the peak frequency can be determined easily. However, it must be taken in mind that for large time series the computing time for wavelet spectra is very high

compared to FFT spectra. The chosen number of classes for spectral slicing strongly modifies Fourier spectra in the low-frequency range. In fig. 2.9, the Fourier spectrum is calculated applying the procedure described in chapter 2.4 with averaging the raw spectrum into 10 and 15 bands, respectively. Wavelet transform is done on 35 scales ranging from 1..400 seconds, the time interval between every data point is assumed to be 1 second.

The top of fig. 2.9 represents the wavelet scalogram according to eq. (2.47). This is a contour plot of the wavelet coefficients plotted against time (ordinate) and frequency or scale (abscissa). Light colors represent positive, dark colors negative wavelet coefficients. The higher the number of scales and the smaller the spacing between scales in the continuous wavelet transform, the better the resolution of the plot. Fig. 2.9 gives an idea of how to interpret such a scalogram with respect to the original input signal, which is given by the ramp time series shown in the middle of fig. 2.9. Every sharp decrease is represented by a clear transition from light to dark colors at scales corresponding to frequencies smaller than 0.5 Hz (a period of 2 s). The two small ramps between 250 s and 310 s are not any more distinguishable at frequencies below 0.02 Hz (a scale of 50 s) in the scalogram. Low-amplitude ramps are represented by low amplitudes of the wavelet coefficients, resulting in more diffuse colors in the contour plot. The black line represents the so called „cone of influence“. When analyzing finite-length time series, errors will occur at the start and end points of the wavelet spectrum, because the Fourier transform assumes the data to be cyclic. The region above this line is subject of errors due to edge effects of the Fourier transformation (Torrence and Compo, 1998).

2.6.4 Conditional sampling

Once we have detected the significant events by the zero crossing method, conditional averages sampled over a suitable time window Δt centered on detection points t_i are calculated by

$$\langle f'(t)\rangle = \frac{1}{N}\sum_{i=1}^{N}\frac{f(t+t_i)-\overline{f_i}}{\sigma f_i} \qquad (2.60)$$

with $t_i-\Delta t/2 < t < t_i+\Delta t/2$, N the number of detection points, σf_i the standard deviation for the time window for normalization and $\overline{f_i}$ the mean value for the time window. Angle brackets denote the conditional average (Collineau and Brunet, 1993b).

To get an estimate of the contribution of the detected organized structures to the total flux of momentum and sensible heat, a triple decomposition of the turbulent variables is used (Bergström and Högström, 1989, Collineau and Brunet, 1993b). Any instantaneous variable f can be decomposed into:

$$f = \overline{f} + f_l + f_s\,. \qquad (2.61)$$

$\overline{f}$ is the long-term average, f_l a perturbation due to large-scale motion and f_s the remaining small-scale fluctuation, with $f_l + f_s = f'$, the turbulent fluctuation in the classical Reynolds decomposition of eq. (2.1). Applying conditional sampling to f', we get $\langle f'\rangle = f_l$, assuming that f_s is uncorrelated with the detected large scale motion and thus $\langle f_s\rangle = 0$. If two fluctuations f' and g' are considered, we obtain:

$$\langle f'g'\rangle = \langle f'\rangle\langle g'\rangle + \langle f_s g_s\rangle\,. \qquad (2.62)$$

Defining a time averaging operator $\overline{\langle\ \rangle}$ as

$$\overline{\langle f'\rangle} = \frac{1}{\Delta t}\int_{-\Delta t/2}^{\Delta t/2}\langle f'(t)\rangle dt \qquad (2.63)$$

over the detection window Δt and averaging eq. (2.62) according to eq. (2.63), we obtain:

$$\overline{\langle f'g'\rangle} = \overline{\langle f'\rangle\langle g'\rangle} + \overline{\langle f_s g_s\rangle}\,. \qquad (2.64)$$

$\overline{\langle f'g'\rangle}$ should now be close to the conventionally averaged Reynolds flux $\overline{f'g'}$, if the detected structures are reasonably representative of the flow, and the first term on the RHS of eq. (2.62) then represents the contribution to $\overline{f'g'}$ from the organized motions whereas the second term on the RHS of eq. (2.62) represents the contribution from small scale motions. This method of conditional sampling is adapted from (Collineau and Brunet, 1993b). Wilczak (1984) and Bergström and Högström (1989) used a similar method, however they worked with time-windows of variable length and averaged every window into 31 bins. The conditional average was then formed by weighting these ‘event’-fluxes according to their individual lengths.

3 Experimental setup

The special measurement campaign was designed as a case study to investigate the vertical structure of the flow and turbulence above an urban canopy. Measurements were taken between July 14, 1995 and February 29, 1996, which results in a total of over 200 days of continuous turbulence data.

Though the large horizontal variability of an European urban surface would require a much denser network of observations for this purpose, because of its three dimensional structure, it was supposed to gain a deeper understanding of the processes contributing to turbulence over such a inhomogeneous surface with the setup described in the following. It must also be stated that it is much more difficult to find a place for measurements in a city than in rural areas considering financial and infrastructural aspects. At last we were very lucky having found an excellent tower in a representative urban area provided by BALCAB, Basler Kabelfernsehen AG.

3.1 Observation site

The city of Basel lies at the point where the borders of Switzerland, Germany and France meet, just at the knee, where the river Rhine turns from a westward direction to north at the transition from the High Rhine Valley to the Upper Rhine Valley. It is surrounded by the hill of the Black Forest (≈1000 m a.s.l., Germany) in the northeast, the Vosges mountains (≈1000 m a.s.l., France) in the northwest and the Jura mountains (≈800 m a.s.l., Switzerland) in the south. The open terrain in the west, where the Airport is situated, is called Burgunderpforte. This topography mainly rules the mesoscale flow over the city, which is dominated by a easterly winds along the Rhine valley turning to north just above the city. Fig. 3.1 gives an overview of the situation.

The data analyzed in this study were collected during a special measurement campaign as a part of the BASTA-project from July 1995 to February 1996 in the inner city of Basel at the area of the Messe Basel. This part of the city is a commercial/ residential area consisting of building blocks,

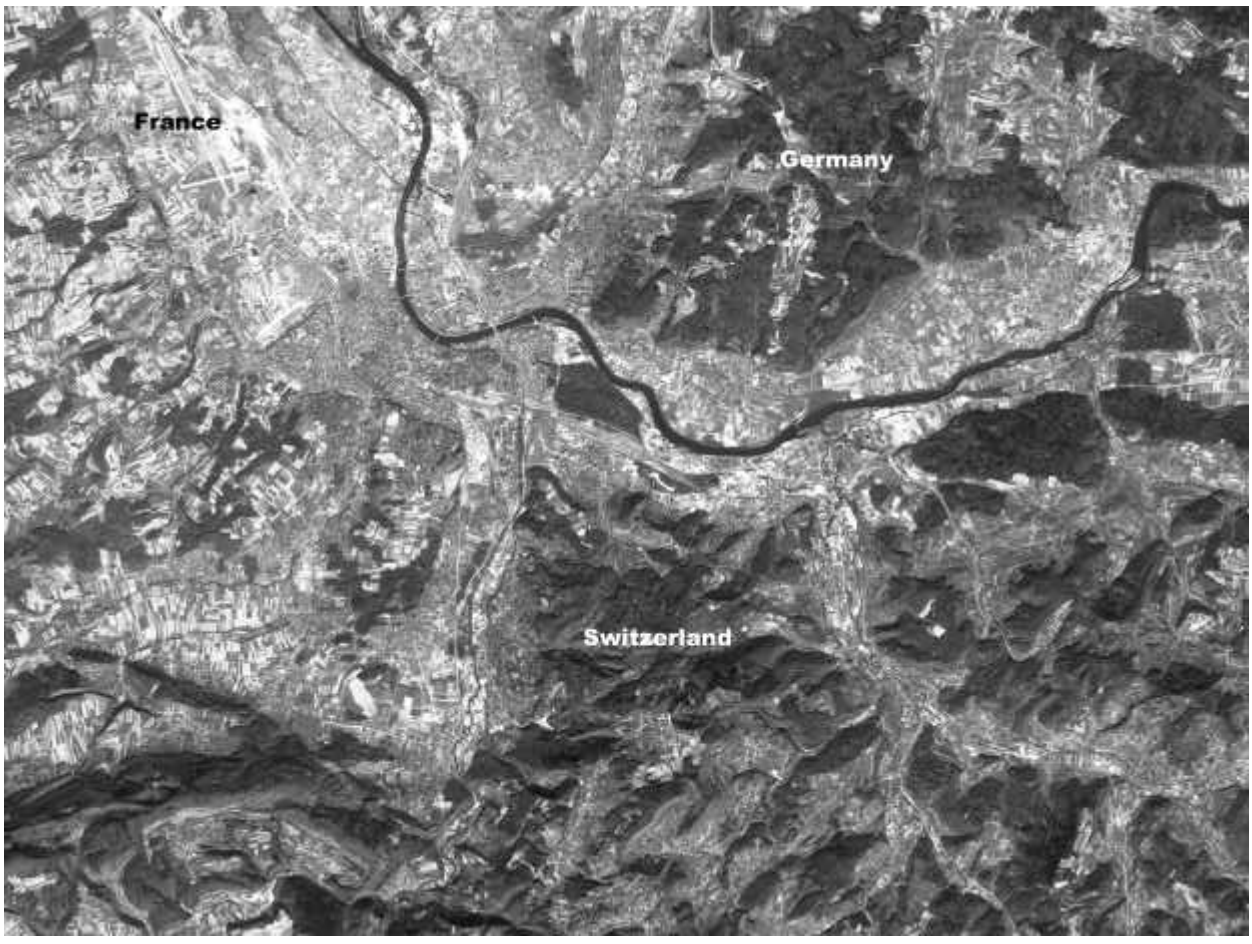

Fig. 3.1: The Basel region from satellite view (Composite Landsat-TM5 and SPOT, A. Hold, MCR Lab).

streets, squares and a few small parks, very typical for European cities. An overview of the site is given in figs. 3.2-5. Within 500 m around the measurement tower, the percentage of area covered by buildings over total area is ≈ 50 % and the average building height is ≈ 24 m with a variation of about ± 6m. Coordinates of the tower location are:

Geographic: 7°35’59’’ E, 47°33’55’’ N;

UTM: 32394687, 5269037;

SLK: 268300, 612125.

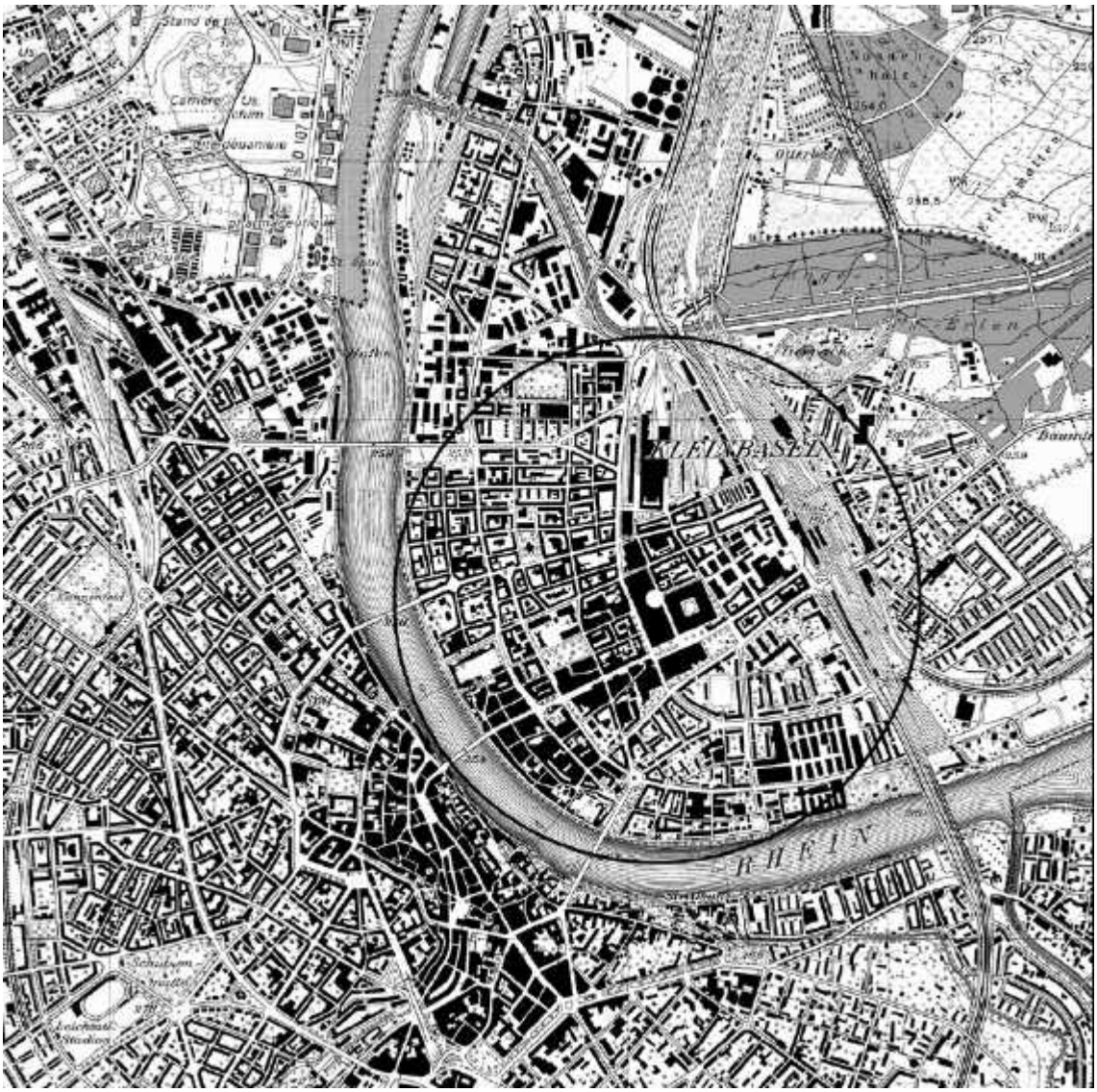

Fig. 3.2: Location of the measurement tower in the inner city of Basel. The radius of the circle is 1000 m.

Fig. 3.3: View from the measurement tower to North West (E. van Gorsel, MCR Lab).

Fig. 3.4: View from the measurement tower to North East (E. van Gorsel, MCR Lab).

Fig. 3.5: View from the measurement tower to South (E. van Gorsel, MCR Lab).

3.2 Instrumentation

Instrumentation was mounted on a 51 m antenna tower, which had its basement on the roof of a business building at 24 m above street level.

Three ultrasonic anemometer-thermometers (sonics) measured at three heights (36, 50 and 76 m a.g.l) the fluctuations of the wind vector (u', v', w') and the sonic temperature (q_s'). At the two lower levels, the sonics were mounted at the end of a north-northeast facing horizontal 6 m boom (∅ 0.08 m), at the uppermost level, the instrument was mounted right on the top of the tower. Sonic data were sampled at 20.83 Hz and all raw data were stored for subsequent analysis. Additionally two profiles (east and west) of wind speed (u), and one profile of air temperature (q) and humidity (q) were measured, each profile consisting of six heights (31, 36, 42, 50, 64 and 75 m a.g.l.). Wind direction (a) was determined at three levels (31, 50, 75 m a.g.l.), and net radiation (R_n) was measured at 64 m. These instruments were mounted on 6 m horizontal booms with 0.08 m diameter (4 m at 64 and 75 m a.g.l., ∅ 0.06 m) facing east-west, anemometers were located 3 m (2 m for the two uppermost levels), thermometers and humidity sensors about 2 m away from the tower center. The profile data were stored as 10 min averages on a Campbell 21X data logger. See tab. 3.1 and figs. 3.1-7 for an overview of the experimental setup.

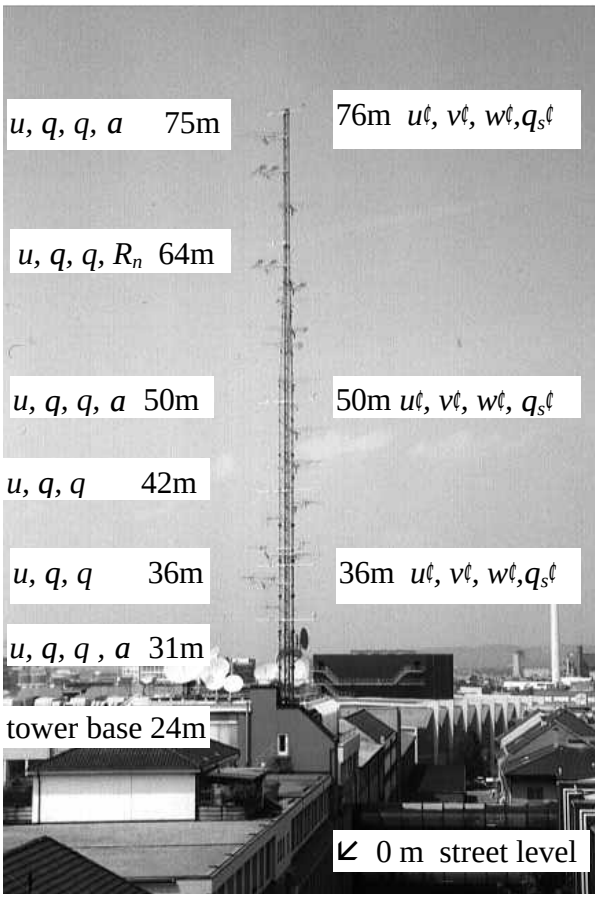

Fig. 3.6: Situation of the tower and instrumentation setup. View from south.

Because of the huge tower and the traffic in the nearby street canyon, the installation of the experimental setup had to be done very carefully and a regular service of the instruments was not possible. For this reason, the radiation data only gives a crude idea of the real value.

In urgent cases, i.e. the total failure of an instrument, we changed the relevant devices. This was done in August, 18, when the ventilation of the 36 m thermistor failed, and in January, 17, 1996, when we exchanged the cup-anemometers at 64 and 75 m.

Tab. 3.1: Instrumental setup (see also fig. 3.6)

	Instrument	Manufacturer	Height [m] a.g.l.
u	cup anemometer	Vaisala WAA15	75, 64, 50, 42, 36, 31
u, a	propeller vane	Young	75, 50, 36
q, q	thermistor, capacitive sensor	Vaisala HMP35A in ventilated radiation shield	75, 64, 50, 42, 36, 31
R_n	pyrradiometer	Schenk Mod. 8111	64
u', v', w', q_s'	ultrasonic anemometer thermometer	Gill-Solent, R2, asymmetric head	76, 50, 36

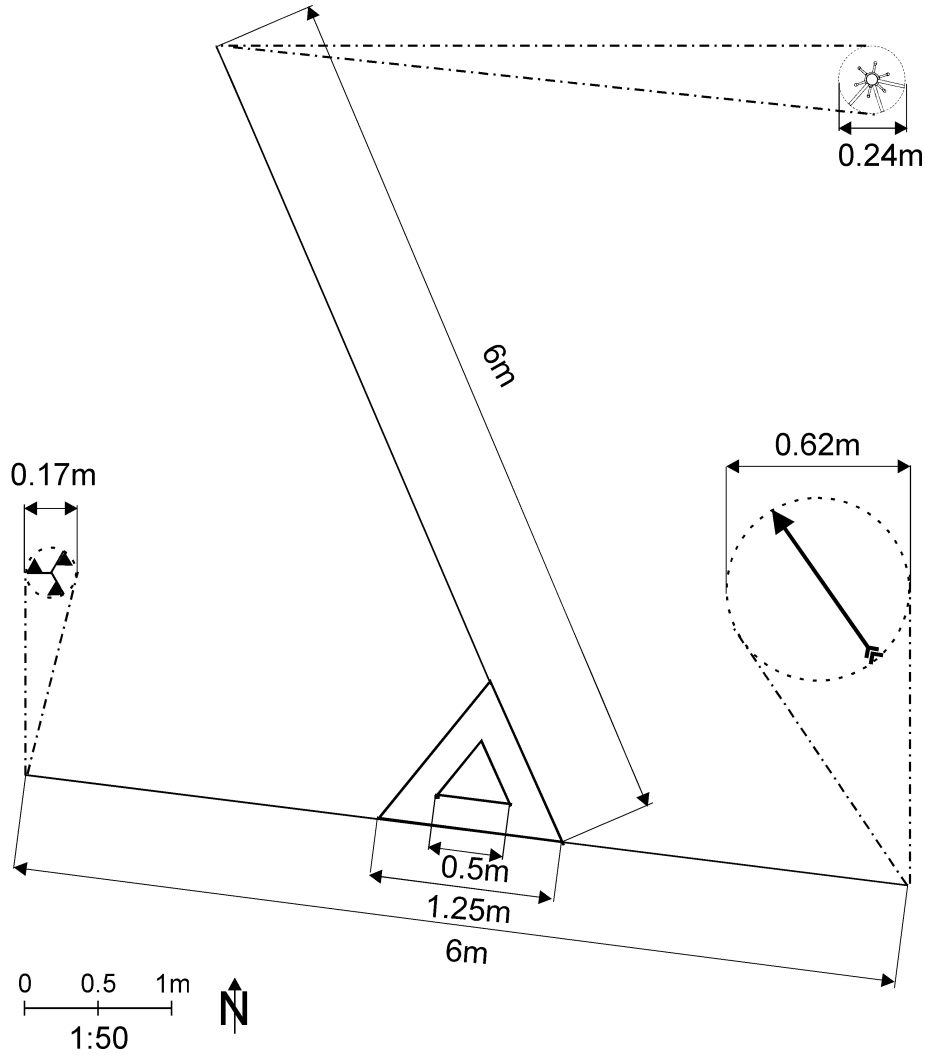

Fig. 3.7: Ground-plan of the tower (scale 1:50) and instrumentation setup (1:25) (E. van Gorsel, MCR Lab).

The tower has a triangle cross section with a sidelength of 1.25 m at the base and 0.5 m at the top. Fig. 3.7 shows the ground-plan of the tower in a 1:50 scale and the instruments in a 1:10 scale. From this figure the undistorted sector of the sonics can be derived easily: it is in the range of 224° < a or a < 103°. Only sonic data from this sector have been analyzed.

In summer 1998, the tower has been moved to another location because the building has been pulled down and a new construction has been built up.

3.3 Meteorological conditions

The distribution of the main wind direction during the measurement period from July 1995 to the end of February 1996 depends strongly on stability conditions, a clear distinction between day and night can be observed in fig. 3.8. During night time (and stable conditions), the flow is dominated by cold air flowing down the upper Rhine valley in the North from the surrounding valleys in the East and South. During day time and unstable conditions, the flow is dominated by two directions, namely a western to north-north western sector and a eastern to south-eastern sector. Westerly winds correspond to situations mainly dominated by synoptic conditions, whilst the North-North-West to East-South-East pattern clearly reflects the surrounding topography of the measurement site and its mesoscale wind systems.

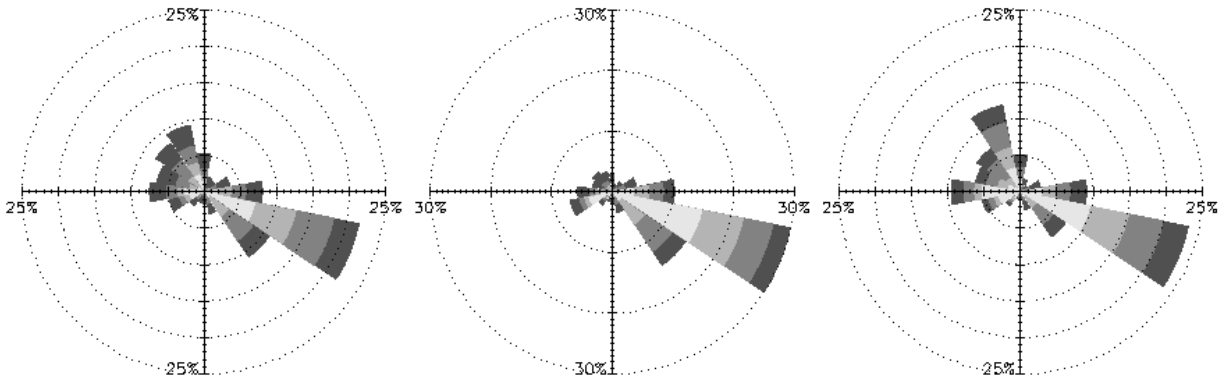

Fig. 3. 8: Distribution of wind direction (16 classes) and wind speed for the measurement period. From left to right: all stability classes, night-time values (R_n < -20 Wm^{-2}, 1846 hours), day-time values (R_n > 0 Wm^{-2}, 1626 hours). Dark to light gray colors refer to wind velocities greater than 0, 2, 3 and 4 m/s, respectively. Circles refer to percentage of all considered respective values.

The following figures show the temperature conditions during the measurement period. In fig. 3.9, the air temperature at z/h = 1.3 is plotted to give an impression of the thermal conditions close above the roof level.

Figure 3.10 shows the behavior of the temperature differences between z/h = 3.2 and z/h = 1.3. Positive temperature gradients are very rare and of small magnitude, if at all, they occur preferably at night time. This means, that also during night time and negative net radiation, we have mostly positive sensible heat fluxes, which is a common feature of urban sites (Feigenwinter et al., 1996). Because heat is released at night from the storage and from anthropogenic sources, the stratification of the urban atmosphere is near neutral or weakly unstable even during clear nights.

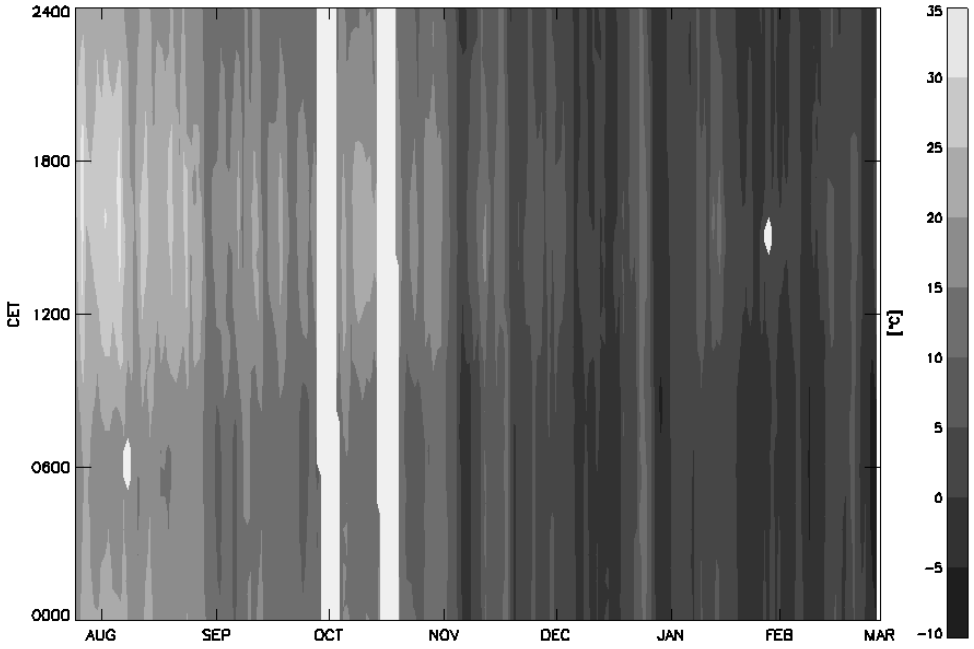

Fig. 3.9: Course of air temperature at z/h = 1.3 during the measurement period.

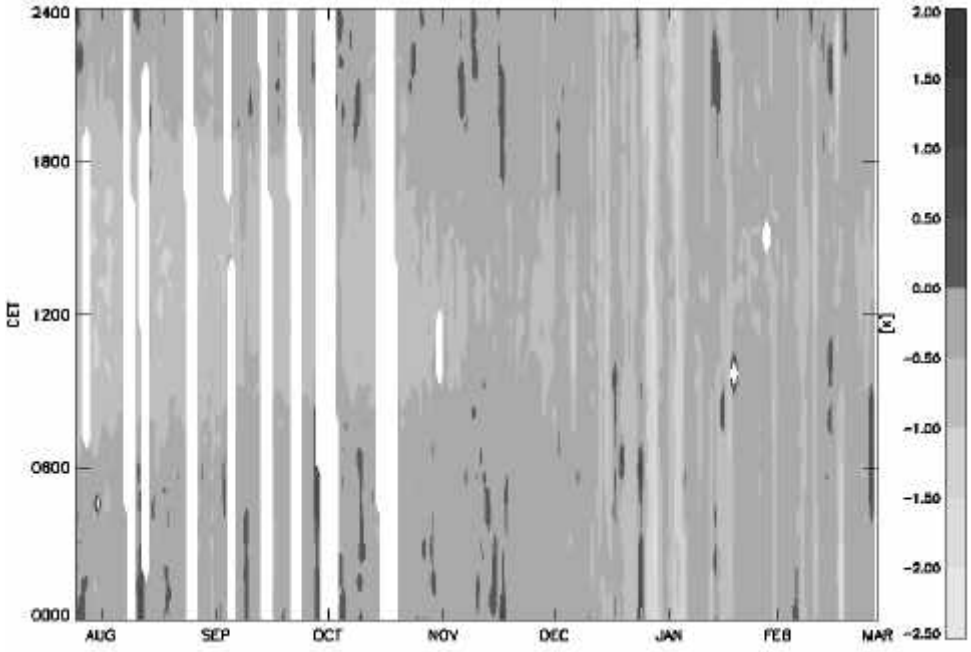

Fig. 3.10: Course of air temperature differences $q_{z/h=3.2}$-$q_{z/h=1.3}$ during the measurement period.

4 Results

4.1 Estimation of the zero plane displacement height

The zero plane displacement height z_d was determined by the temperature variance method described in Rotach (1994). Under certain conditions the surface of a city can be regarded as thermally homogeneous, even though it is dynamically rough. Therefore the measurement of the dimensionless temperature variance σ_θ/θ_* can be used for the determination of z_d provided that the same z_d is valid for the flux of momentum as well as for the flux of latent heat. According to MOS theory, the relationship in eq. (2.26) describes the behavior of σ_θ/θ_* for unstable conditions in the SL. To get an estimate of z_d, the difference between measured and calculated values is minimized according to eq. (4.1) by varying z_d.

$$err = \left(\frac{1}{N} \sum_{i=1}^{N} \left(\frac{\sigma_{\theta_i}}{\theta_{*i}} - \left(\frac{\sigma_\theta}{\theta_*} \right)_{eq.(2.26)} \right)^2 \right)^{\frac{1}{2}} \qquad (4.1)$$

In eq. (4.1), N is the number of measurements and *err* is the value to be minimized.

Table 4.1 gives an overview on the results of the temperature variance method for the undisturbed sector of wind direction. The resulting averaged z_d estimates for the lower two measurement heights are 21 m and 23.5 m and correspond quite well whereas at the topmost level we find an unrealistic high value of about 40 m. The reason for this could be the different source area of this sensor that probably does not fulfill the conditions for thermal homogeneity. A zero plane displacement of 22 m corresponds to 0.92 times the building height h, which seems comparatively high to values for vegetation canopies, which are in the range of 2/3 to 3/4 h. However, considering that urban buildings stand very close together and are stiff compared to a vegetation canopy, in a way that the wind profile can not penetrate very deep into the urban canopy layer, and also taking into account the excellent agreement of the results from the lower two sonics, it is justified to use a z_d-value of 22 m. Van Gorsel (1998) analyzed the same data set for an estimation of z_d, using the equation for the logarithmic wind profile under neutral conditions. Her results are in good agreement with the values presented in this study, namely 15, 20 and 30..50 m for z/h = 1.5, 2.1 and 3.2, respectively. Also, a further attempt similar to the temperature variance method, using the universal function for σ_w/u_* (eq. 2.26) for the calculation of z_d, yielded the same results. This method is described in De Bruin (1997). In any case, the physical meaning of z_d as a property of the surface itself as well as a property of the flow in the surface layer still remains unclear. Also it is likely, that different z_d exist for momentum, sensible and latent heat flux, if the source area for the fluxes is not the same. Since all three methods yielded similar qualitative and quantitative results and no 'clear choice of the best method' can be recommended (Grimmond et al., 1998), z_d = 22 m is taken for all further calculations.

Tab. 4.1: Values for the zero plane displacement height z_d calculated by the temperature variance method for the selected wind direction sections (number of runs per section in brackets).

Height	Azimuth								Average
	240°± 15°	270°± 15°	300°± 15°	330°± 15°	0°± 15°	30°± 15°	60°± 15°	90°± 15°	225°- 105°
z/h=3.2	47.0 (12)	42.0 (68)	39.0 (26)	39.0 (99)	37.0 (50)	35.0 (2)	34.0 (4)	48.0 (51)	**40.1**
z/h=2.1	29.5 (15)	23.5 (115)	26.5 (39)	22.5 (106)	19.5 (47)	-	19.5 (5)	23.5 (53)	**23.5**
z/h=1.5	25.5 (18)	22.0 (120)	22.0 (47)	20.0 (125)	19.0 (54)	18.5 (3)	24.5 (3)	16.5 (56)	**21.0**

4.2 Integral statistics and profiles

For comparison reasons with spectral and wavelet analysis in the following chapters, all analysis has been done on 53-minute averages. In Feigenwinter et. al. (1999), the analysis of profiles and integral statistics has been done on 30-minute averages. In fact, differences are not crucial at all. Table 4.2 gives an overview on the chosen stability classes and the number of analyzed 53-minute runs.

The following restrictions have been applied for data selection:

- wind direction: 224° < α or α < 103° (undisturbed sonic sector)
- wind speed at z/h = 3.2: $\overline{u} > 2$ ms^{-1}
- all three measurement levels lie in the same stability class. Therefore, the sum of the runs of the four stability classes from stable to unstable does not equal the number of the overall-class. Though lots of runs are eliminated, this procedure guarantees that we have the same conditions at all three levels.

4.2.1 Profiles

In figs. 4.1-3, average profiles of velocity standard deviations are shown for the five stability classes. Standard deviations $\sigma_{u,v,w}$ and the friction velocity u_* are scaled with the u_*-value from the uppermost measurement level at z/h=3.2 and error bars indicate the run-to-run variability. In the near neutral case, profiles of σ_u and σ_v in fig. 4.1 and fig. 4.2 are nearly uniform, whereas σ_w increases slightly with height. Taking into account the small scatter, the values correspond surprisingly well to the recommended values of 2.4, 1.9 and 1.25 by Panofsky and Dutton (1984) for σ_u/u_*, σ_v/u_* and σ_w/u_*, respectively, for neutral conditions and flat terrain. Under unstable conditions the profiles of σ_u and σ_v decrease with height, whereas for stable conditions σ_u increases and σ_v has a relative minimum at z/h=2.1. The scaled vertical velocity variance σ_w/u_* in fig. 4.3 shows a slight increase with height and increases from neutral to unstable conditions, differences become larger as instability increases. This is in contrast to the observation of Rotach (1995), who reported a decrease of σ_w/u_{*ref} with increasing height for near-neutral stratifications.

Tab. 4.2: Stability classes and number of analyzed 53-minute runs for profiles and integral statistics

All	Stable	Neutral	Weakly unstable	Unstable
$-20 < (z- z_d)/L < 20$	$(z- z_d)/L > 0.05$	$-0.05 \le (z- z_d)/L \le 0.05$	$-0.5 \le (z- z_d)/L < -0.05$	$(z- z_d)/L < -0.5$
1372	78	113	301	73

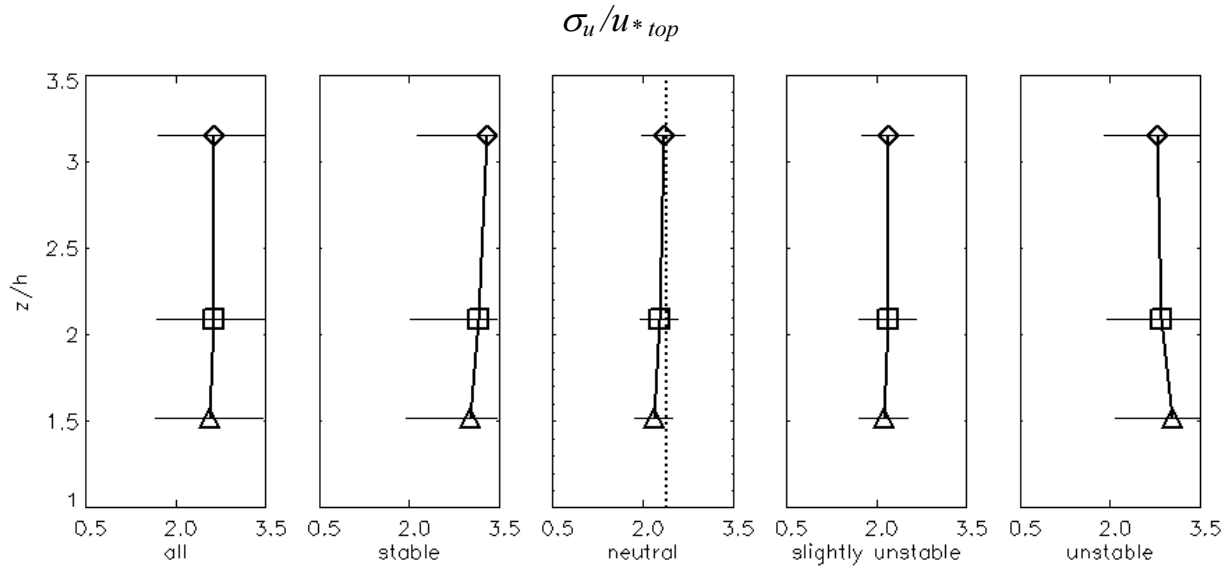

Fig. 4.1: Scaled profiles of standard deviation $\sigma_u/u_{*\,top}$ for all stability classes.

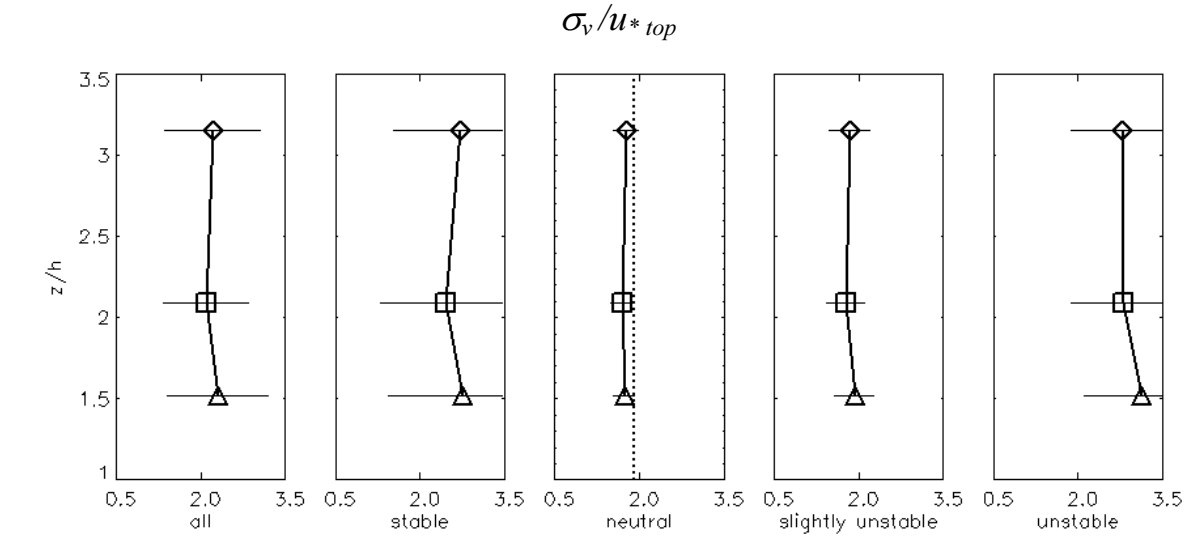

Fig. 4.2: Scaled profiles of standard deviation $\sigma_v/u_{*\,top}$ for all stability classes.

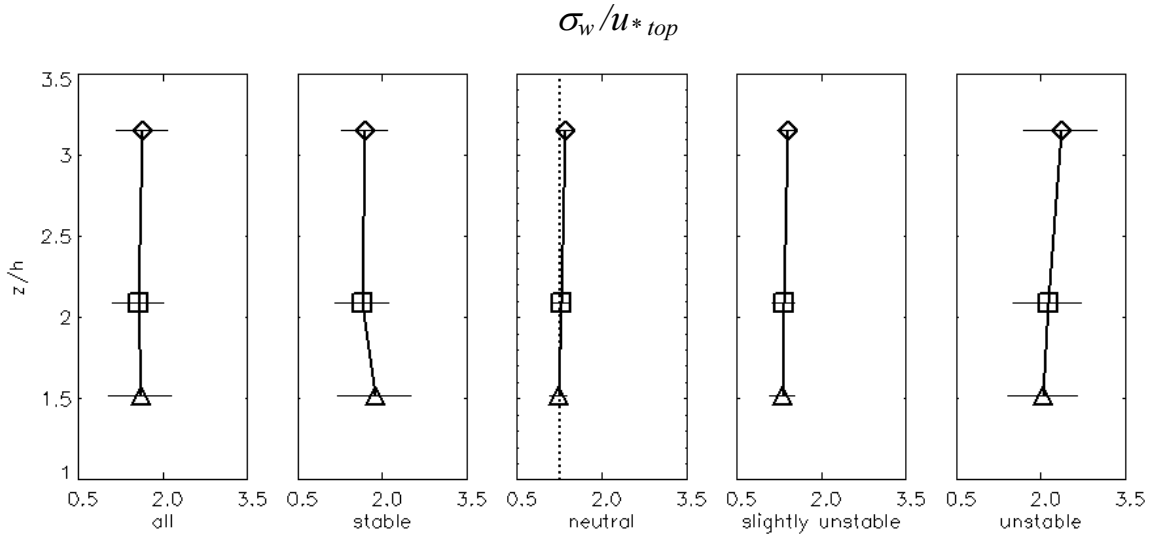

Fig. 4.3: Scaled profiles of standard deviation $\sigma_w/u_{*\,top}$ for all stability classes.

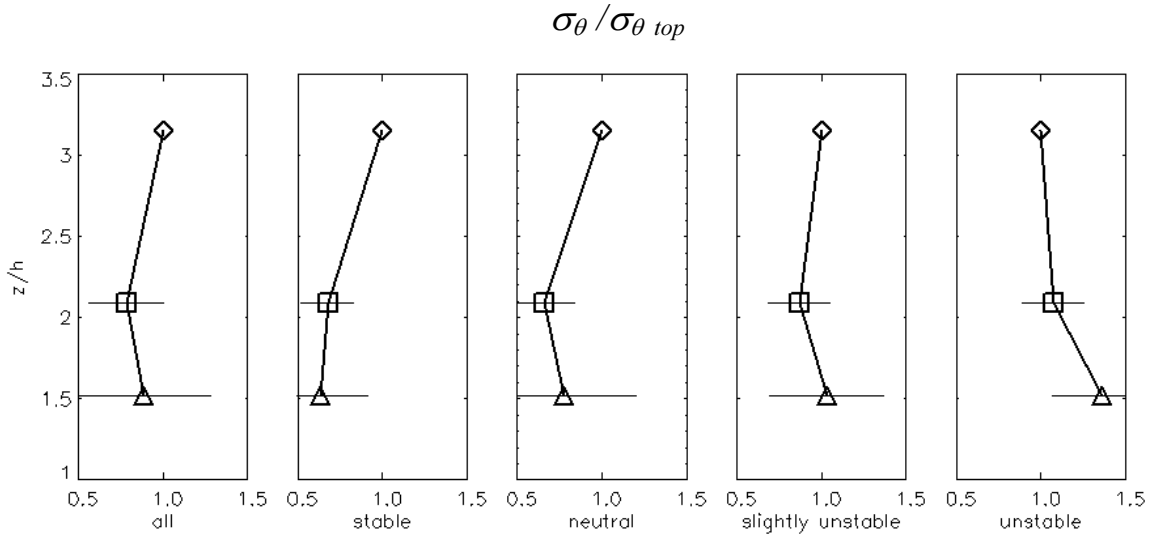

Fig. 4.4: Scaled profiles of standard deviation $\sigma_\theta/\sigma_{\theta top}$ for all stability classes.

The profile of temperature variance normalized by the σ_θ value of the uppermost level (fig. 4.4) shows a strong decrease of σ_θ with increasing height for unstable conditions. At z/h=1.5 fluctuations are about 50% higher than at z/h=3.2. For stable and neutral stratifications, σ_θ is reduced in the lower levels compared to the top level. This increase of σ_θ between z/h=2.1 and z/h=3.2 for slightly unstable to stable stratifications supports the idea of different thermal source areas, as we would expect σ_θ to decrease with height. This effect is suppressed under strong unstable conditions, where σ_θ is dominated by thermal convection.

Profiles of friction velocity u_* are displayed in Fig. 4.5. For unstable stratification u_* decreases slightly between the two upper levels, whereas for the remaining cases, a significant increase with height between the two lower levels can be observed. Under stable stratification the maximum occurs at z/h=2.1 at the second measurement level. Considering these profiles and taking into account Rotach's (1993a) suggestion to consider the RS as the layer within u_* increases from zero to the IS value, we can set the upper boundary of the RS somewhere around the second measurement level at z/h=2.1. A similar profile of u_* is reported in Oikawa and Meng (1995).

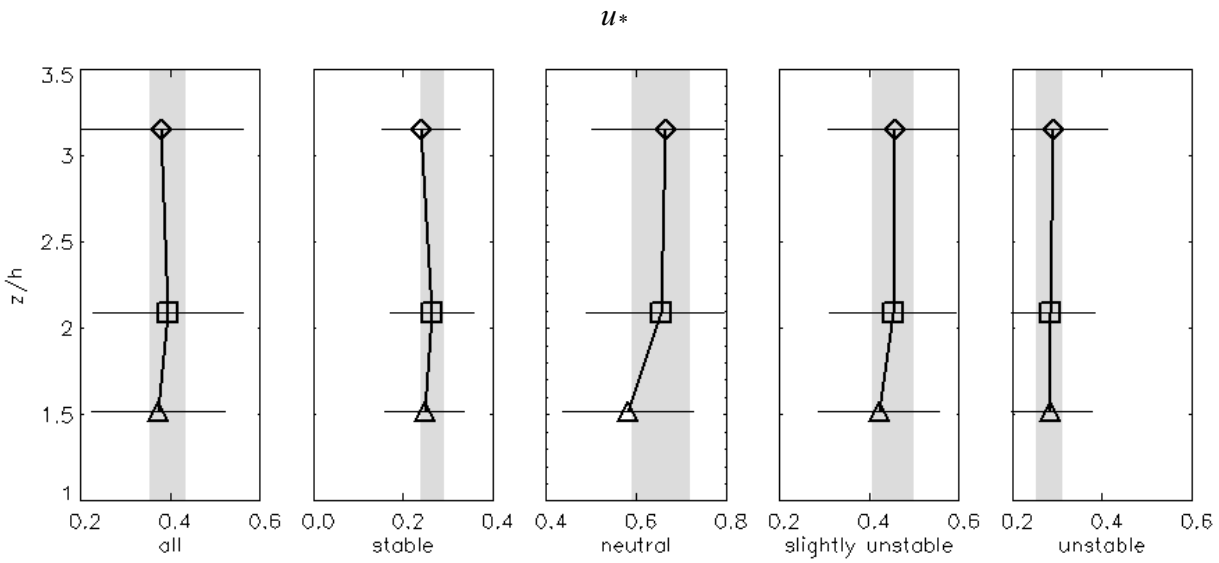

Fig. 4.5: Absolute profiles of friction velocity u_* for all stability classes. The shaded regions refer to ±10% of the value at z/h = 2.1.

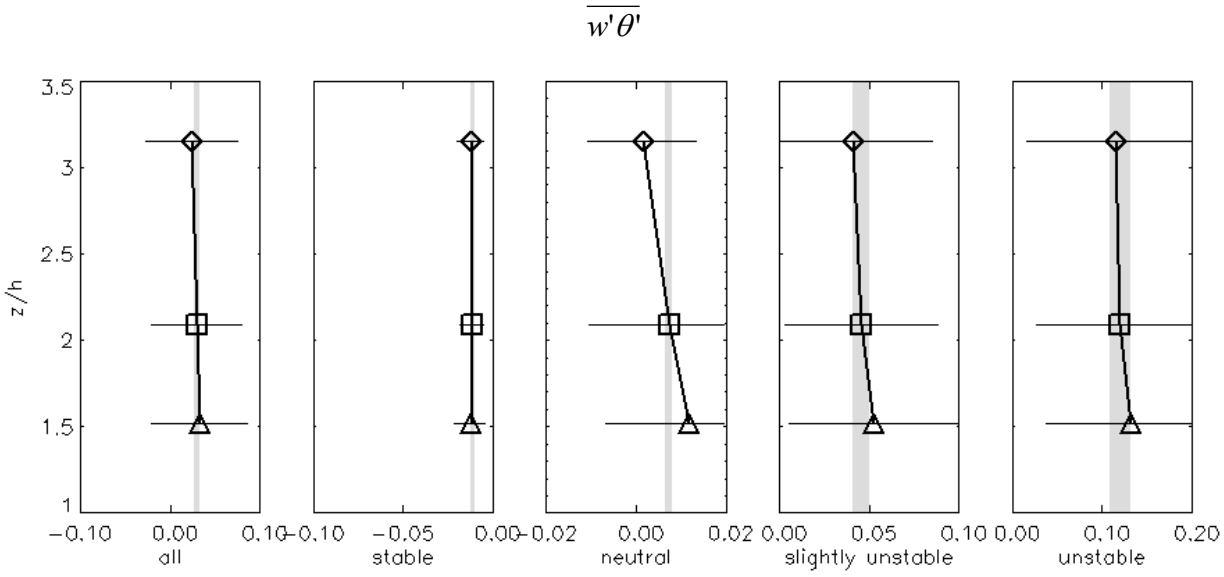

Fig. 4.6: Averaged profiles of kinematic heat flux $\overline{w'\theta'}$ for all stability classes. The shaded regions refer to ±10% of the value at z/h = 2.1.

Due to the occasional very small values, the profiles of the kinematic heat flux $\overline{w'\theta'}$ are not normalized with the value from the uppermost level but displayed in fig. 4.6 as simple arithmetic averages for the respective stability class. Though the over all profile looks nearly constant, it shows a slight decrease with increasing height, in fact, the 10% variation supposed for a constant flux layer is only given for unstable conditions and above $z/h = 2.1$. The decrease of $\overline{w'\theta'}$ with increasing height is given for all stability classes, except under stable conditions. This is in contrast to the conceptual sketch of the vertical variability of the turbulent flux of sensible heat in Rotach (1991), which predicts an increase of the sensible heat flux above the RS. Obviously, the lowest level is directly and strongly influenced by the near roof level, that acts as heat source (or sink), and the absence of any evaporating medium. During stable conditions, radiative cooling and during unstable conditions, thermal convection leads to smaller respectively larger fluxes than at the levels above. This is in extreme contrast to profiles of sensible heat flux over a pine forest reported in Vogt (1995), where the lowest level shows always the smallest sensible heat fluxes, but the largest latent heat fluxes during the day under unstable conditions. An explanation for this could be the horizontal advection of cooler (or warmer in the case of the forest) air in the higher layers.

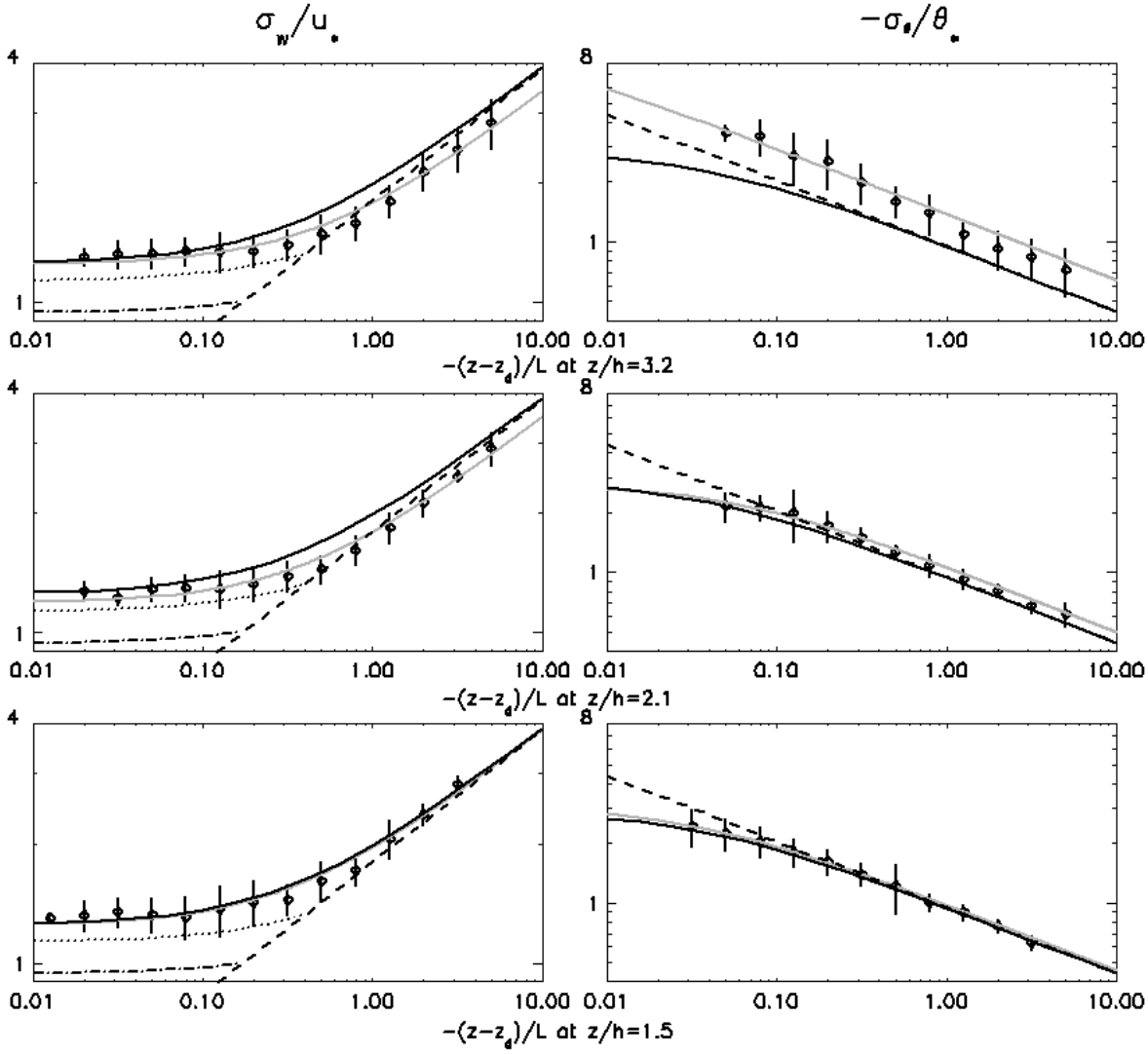

Fig. 4.7: Left column: σ_w/u_* for unstable conditions. Class averages are plotted with standard deviations as error bars (fitted curve in light gray). Functional relationships are from Panofsky and Dutton (1984) (solid), Clarke et al. (1982) (dotted) and Rotach (1993b) (dashed-dotted). Right column: same as left but for $-\sigma_\theta/\theta_*$. Functional relationships is after De Bruin et al. (1993). The free convection limit is indicated by the dashed line.

Tab. 4.3: Number of analyzed 53-minute runs for nondimensionalized standard deviations (σ_w/u_* / $-\sigma_\theta/\theta_*$) in fig. 4.7.

	$-(z-z_d)/L$													
	0.013	0.021	0.033	0.052	0.082	0.129	0.205	0.325	0.515	0.815	1.29	2.05	3.25	5.15
z/h=3.2		4/-	11/-	17/5	44/13	52/18	82/37	93/49	92/56	57/36	49/39	30/23	20/14	9/8
z/h=2.1		8/-	13/-	47/15	67/26	86/41	107/5	79/49	68/42	44/35	26/20	15/14	5/5	4/4
z/h=1.5	6/-	17/-	52/-	64/21	99/53	84/34	80/46	84/60	50/38	17/16	14/12	4/4	4/4	

4.2.2 Normalized standard deviations

In this section, the nondimensionalized standard deviations of the vertical wind component and temperature are analyzed. The following plots shall give an idea, of how good the MOS relationships are fulfilled and whether MOS theory is applicable over such a heterogeneous surface like a European city. It must be stated, that the results are extremely sensitive on the data set used. For $-\sigma_\theta/\theta_*$ for instance, the restriction has been made, that $\overline{w'\theta'}$ must at least reach a value of 0.03 (0.01 for σ_w/u_*), otherwise, the plot is not readable due to extremely large errorbars for stabilities near neutral. This explains the missing datapoints and the low number of analyzed runs for σ_θ/θ_* at near neutral values of $(z-z_d)/L$ in tab. 4.3 and fig. 4.7.

The analysis shows, that the dimensionless standard deviation for the vertical wind velocity σ_w/u_* is systematically smaller for all three measurement heights than the values predicted by the MOS function for σ_w/u_* and unstable conditions $(z-z_d)/L < -0.1$.

The reference values for C_{w1} and C_{w2} in eq. (2.26) are taken from Panofsky and Dutton (1984) as 1.25 and 3. A similar behavior is reported by Clarke et al. (1982), Roth and Oke (1993b), Rotach (1993b) and Oikawa and Meng (1995), however, deviations to the reference in this study are smaller, which is shown on the left side in fig. 4.4. Note that local values of u_* and L are taken. As listed in tab. 4.4, all urban studies report smaller values for C_{w1} and C_{w2} in eq. (2.26), therefore, one can conclude, that over rough urban surfaces, an enhanced mechanical production of vertical velocity fluctuations and thus transfer of momentum is established.

Since the zero plane displacement height z_d was determined by the temperature variance method (see previous section) from the two lower levels, the $-\sigma_\theta/\theta_*$ values are practically forced to follow the MOS function in eq. (2.26) with $C_{\theta1}$ and $C_{\theta2}$ as 2.9 and 28.4 (see tab. 2.2). Measurements at this heights therefore fit well to the predicted function. However, the large anomalies at the uppermost level at z/h=3.2 at the RHS in fig. 4.7 suggests, that thermal homogeneity is not given for the source area of this sensor. This is also in agreement to the statement derived from the σ_θ-profile in fig. 4.4 in the previous section and the failure of the temperature variance method for this measurement level. Large scatter is expected near neutral, where the sensible heat flux becomes close to zero but temperature fluctuations are still present, therefore runs with kinematic heat fluxes < 0.03 Kms^{-1} have been excluded from the analysis. In his review paper, Roth (1999) published average values for $C_{\theta1}$ and $C_{\theta2}$ derived from several studies (tab. 4.4). It is interesting that the averaged curve for $z/h >$ 2.5 lies well above the reference line. Obviously there is a trend to higher values for $-\sigma_\theta/\theta_*$ in urban areas above the roughness sublayer.

Tab. 4.4: Comparison of values C_1 and C_2 in eq. (2.26) for σ_w/u_* and σ_θ/θ_* from different studies

C_{w1}	C_{w2}	z/h	surface	study
1.25	3		„ideal“	Panofsky and Dutton (1984)
1.13	1.56	$z/h \approx 4$	average value of four urban sites, $0 \geq (z- z_d)/L \geq -5$	Clarke et al. (1982)
0.94	1.29	$1.27 \leq z/h \leq 1.55$	urban site, $0 \geq (z- z_d)/L \geq -1$	Rotach (1993b)
1.12	2.48	$1.5 \leq z/h \leq 5.6$	average of several urban studies	Roth (1999)
1.15	2.09	$2.5 \leq z/h$	average of several urban studies $-0.05 \geq (z- z_d)/L \geq -6.2$	
1.24	1.94	$z/h = 3.2$	urban site, $-0.01 \geq (z- z_d)/L \geq -8$	this study
1.19	2.46	$z/h = 2.1$		
1.25	2.90	$z/h = 1.5$		
$C_{\theta 1}$	$C_{\theta 2}$	z/h	surface	study
2.9	28.4		„ideal“	De Bruin et al. (1993)
3.03	24.4	$1.5 \leq z/h \leq 5.6$	average of several urban studies	Roth (1999)
4.1	65	$2.5 \leq z/h$	average of several urban studies $-0.05 \geq (z- z_d)/L \geq -6.2$	
9.8	366	$z/h = 3.2$	urban site, $-0.02 \geq (z- z_d)/L \geq -8$	this study
2.8	18.1	$z/h = 2.1$		
3.1	31.4	$z/h = 1.5$		

4.3 Quadrant analysis

A common problem of quadrant analysis is the fact, that if the total turbulent momentum flux or sensible heat flux is very small, extremely large contributions of the individual sectors can occur, which will lead to a domination of the average by single events. Therefore, events with contributions larger than five times the average for hole size 0 have been excluded from calculation.

Another problem arises when analyzing the sensible heat flux under near neutral conditions by the means of quadrant analysis. Because of the change of sign, contributions can be positive and negative for each quadrant. Therefore, only unstable cases have been analyzed for $\overline{w'\theta'}$.

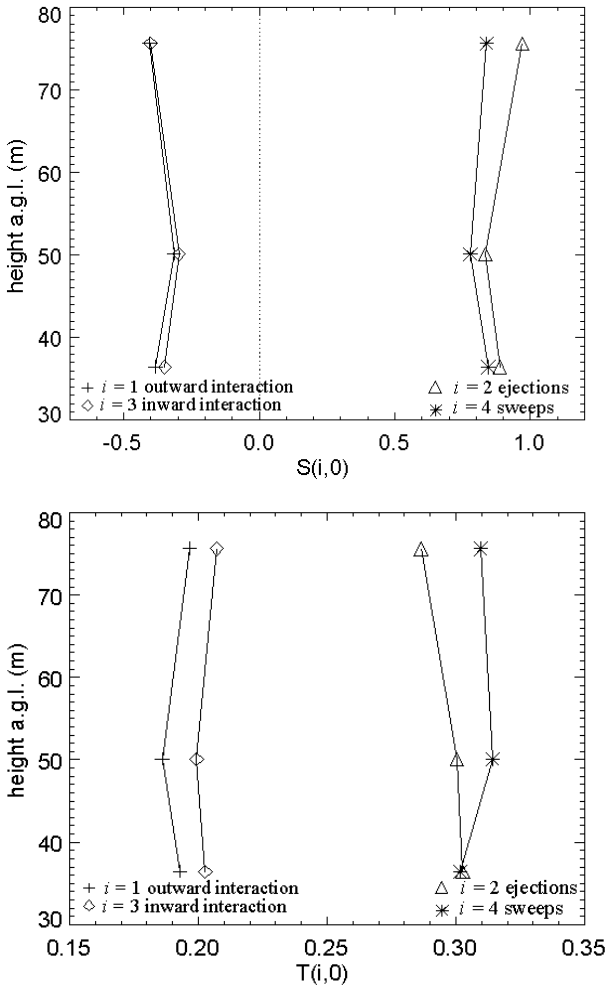

Fig. 4.8: Profiles of stress fractions $S(i,H)$ (top) and time fractions $T(i,H)$ (bottom) for all stability classes.

Because vertical transport of lateral momentum ($\overline{v'w'}$) is included in Reynolds stress according to the definition in eq. (2.16), this contribution would have been to be analyzed separately in quadrant analysis. However, in practically all of the analyzed runs, Reynolds stress is dominated by the longitudinal component and $\overline{v'w'}$ is much smaller than $\overline{u'w'}$, therefore the analysis has been done only for $\overline{u'w'}$.

The upper part of fig. 4.8 shows the contributions of the averaged stress fractions at hole size zero $S_{i,0}$ for all three measurement levels and all stability classes ($-20 < (z-z_d)/L < 20$). The contributions of organized motions (sweeps and ejections) are roughly two times larger than those of the interaction quadrants. Ejections contribute slightly more to the total momentum flux than sweeps, especially at the uppermost level, which means, that $|\Delta S_{H=0}|$ is largest at this particular level. It will be shown later, that different vertical profiles of the averaged stress contributions are obtained, if stability is considered.

Looking at the profile of time fractions in fig. 4.8 (bottom), the summed time fractions of sweeps and ejections cover about 60% of the total time. However, with increasing height, the time fraction of the ejections decreases, though the stress fraction of the same quadrant increases. This means, that a large amount of momentum is transported due to ejections in a relatively short time. Again, as for the stress fractions, the profiles differ considerably if stability is considered.

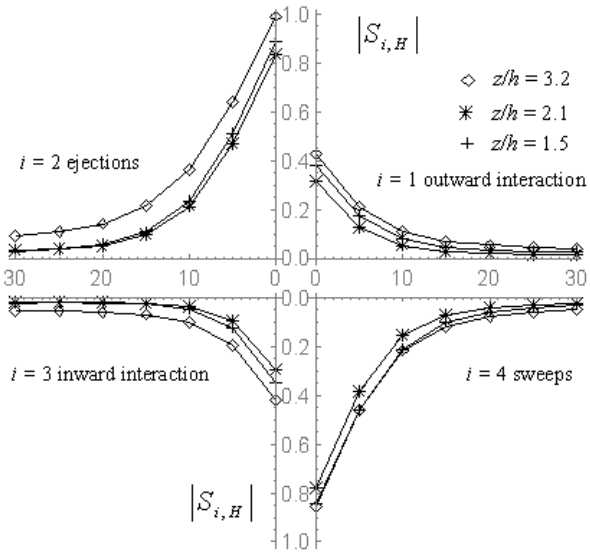

Fig. 4.9: Contribution of stress fractions $S(i,H)$ for varying hole size H and all stability classes.

From fig. 4.9, the dominance of ejections (i=2) at the uppermost level z/h=3.2 can be derived up to excluded regions of hole size 30, which associates these structures to large scale processes. Large contributions to the average momentum flux during ejections and sweeps can be observed at all levels, whereas the contributions from the interaction quadrants are comparatively small and rapidly decreasing with increasing hole sizes and therefore correlated with small scale turbulence. Looking at the cumulative distribution at all three heights of momentum flux fractions and time fractions for varying hole sizes in fig. 4.10, large parts of the flux are accomplished with a comparatively short duration, i.e. about 70% of the flux during 15 % of the time. The ratio of the summed fractions $\Sigma T(i,H)/\Sigma S(i,H)$ as a measure of intermittency is given in tab. 4.5 as well as other parameters related to quadrant analysis like ΔS_0, $\gamma = S_{2,0}/S_{4,0}$ and Exuberance Ex.

Parameters ΔS_0, and $\gamma = S_{2,0}/S_{4,0}$ both give an idea about the dominance of ejections over sweeps or vice versa. If the whole stability range is considered, ejections dominate sweeps at all levels, dominance is strongest at level z/h = 3.2. Exuberance Ex as the ratio of "random" (the interaction terms) to "organized" turbulence (ejections and sweeps) is high compared to other studies. The differentiation into stability classes will bring more clearness to the subject.

For neutral stratification, sweeps are more efficient in transferring momentum to the surface than ejections as far as the two lower levels are considered. At z/h=3.2, the contributions from quadrants 2 and 4 are of the same magnitude, as shown in fig. 4.11. Also, at z/h = 1.5, sweeps are associated with processes of larger scales than ejections, and contributions for all hole sizes are larger than at the two levels above in this quadrant. Obviously, during neutral conditions, when turbulence is mainly mechanically driven, momentum is transported to the surface to a large amount by downward motions of relatively large scales.

Tab. 4.5: The ratio of summed time fractions to summed stress fractions for hole size 5 and 10, ΔS_0, $\gamma = S_{2,0}/S_{4,0}$ and Exuberance Ex for all stability classes

	$\frac{\sum T(i,5)}{\sum S(i,5)}$	$\frac{\sum T(i,10)}{\sum S(i,10)}$	ΔS_0	$\frac{S_{2,0}}{S_{4,0}}$	Ex
z/h = 3.2	0.22	0.13	-0.135	1.16	-0.46
z/h = 2.1	0.19	0.11	-0.057	1.07	-0.38
z/h = 1.5	0.21	0.12	-0.041	1.05	-0.42

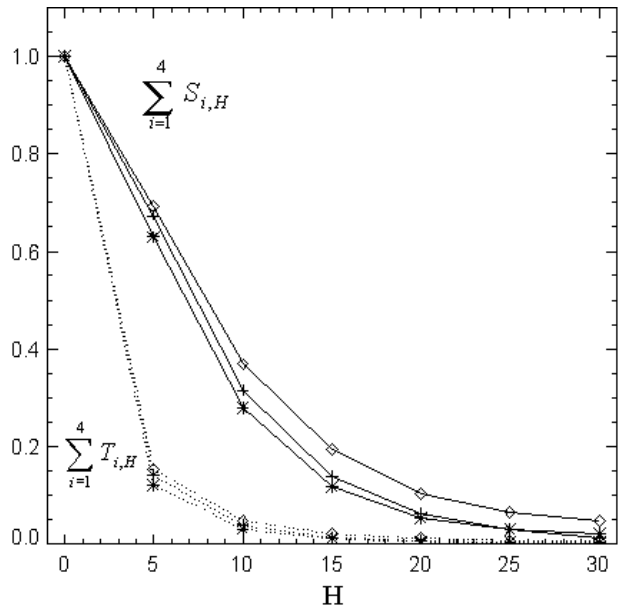

Fig. 4.10: Cumulative magnitudes of stress fractions $\Sigma S(i,H)$ (solid) and time fractions $\Sigma T(i,H)$ (dashed) for varying hole size H and all stability classes.

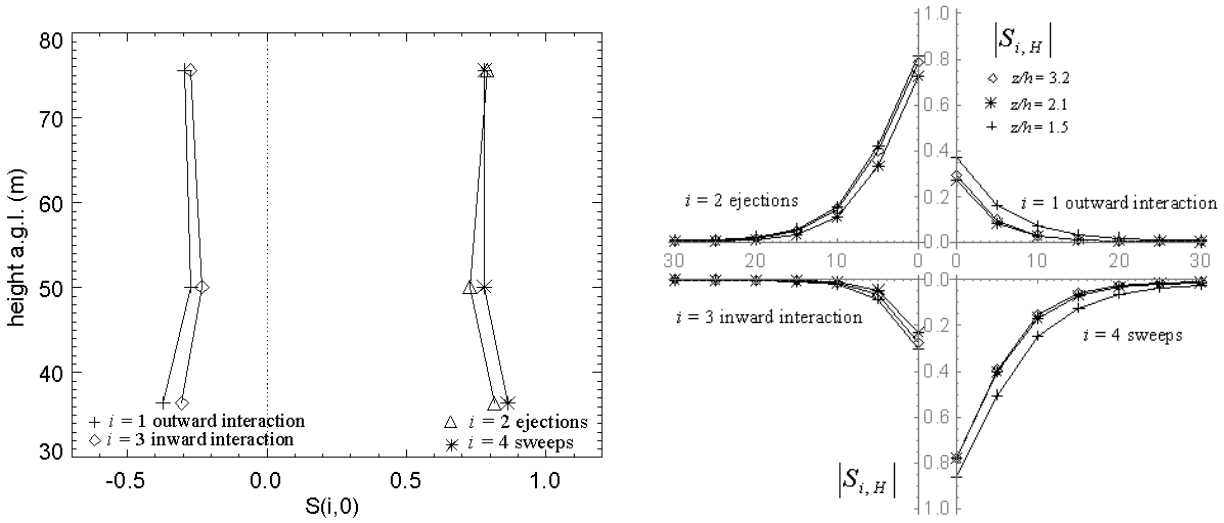

Fig 4.11: As figs. 4.8 and 4.9, but for neutral stratification $|(z-z_d)/L| < 0.05$.

As stratification becomes more unstable, the contribution of ejections to the total flux is dominant at all heights, while the profile of the counter-gradient quadrants 1 and 3 (the interaction terms) looks more or less the same as under neutral conditions. This is shown in fig. 4.12 (left). The right side of fig. 4.12 shows the contributions of the four quadrants to the total sensible heat flux (note that quadrant 1 here refers to ejections and quadrant 3 to sweeps). While the profiles of the two lower levels are comparable to each other for contributions to momentum and sensible heat flux, the interaction terms become increasingly important and contributions of all quadrants are generally higher at the uppermost level z/h=3.2.

The uppermost level at z/h=3.2 shows large contributions to the total sensible heat flux even at hole sizes greater than 15 (cf. fig. 4.14). This means, that large scale eddies contribute essentially to the total sensible heat flux in a relatively short portion of time, compared to the two lower levels. The same pattern was observed by Bergström and Högström (1989) under unstable conditions over a pine forest.

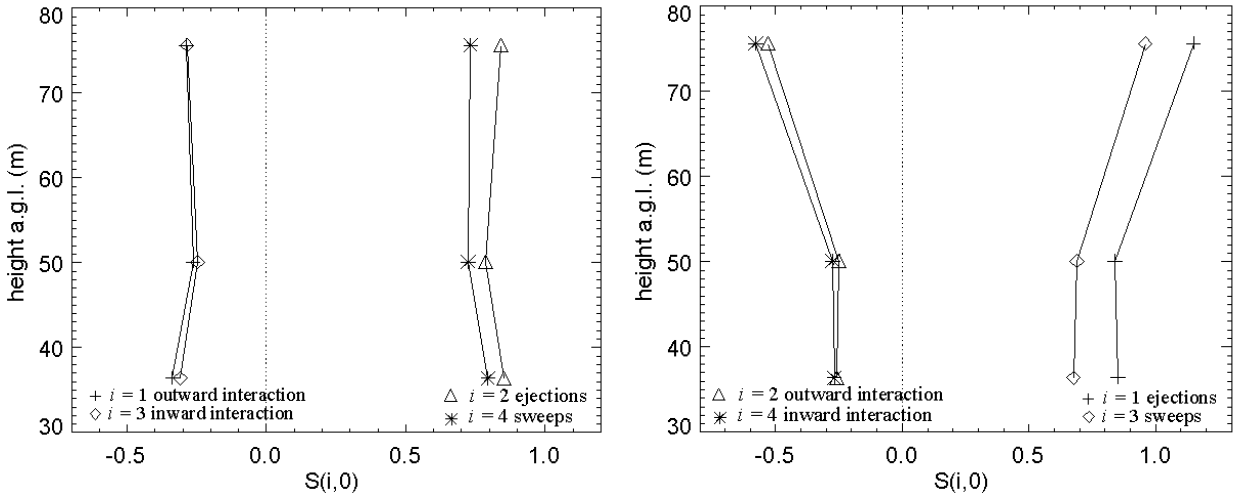

Fig 4.12: Averaged vertical profiles of momentum flux fractions (left) and sensible heat flux fractions (right) contributed by the four quadrants for weakly unstable stratification $-0.5 < (z-z_d)/L < -0.05$.

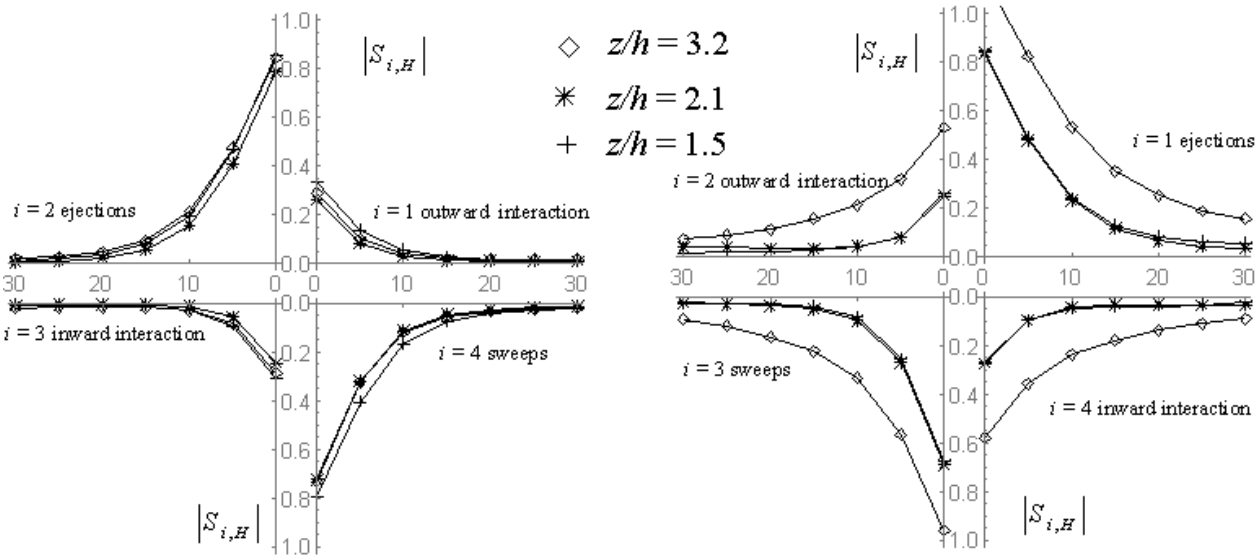

Fig 4.13: Contribution of stress fractions (left) and heat flux fractions (right) for varying hole size *H* and weakly unstable stratification $-0.5 < (z\text{-}z_d)/L < -0.05$.

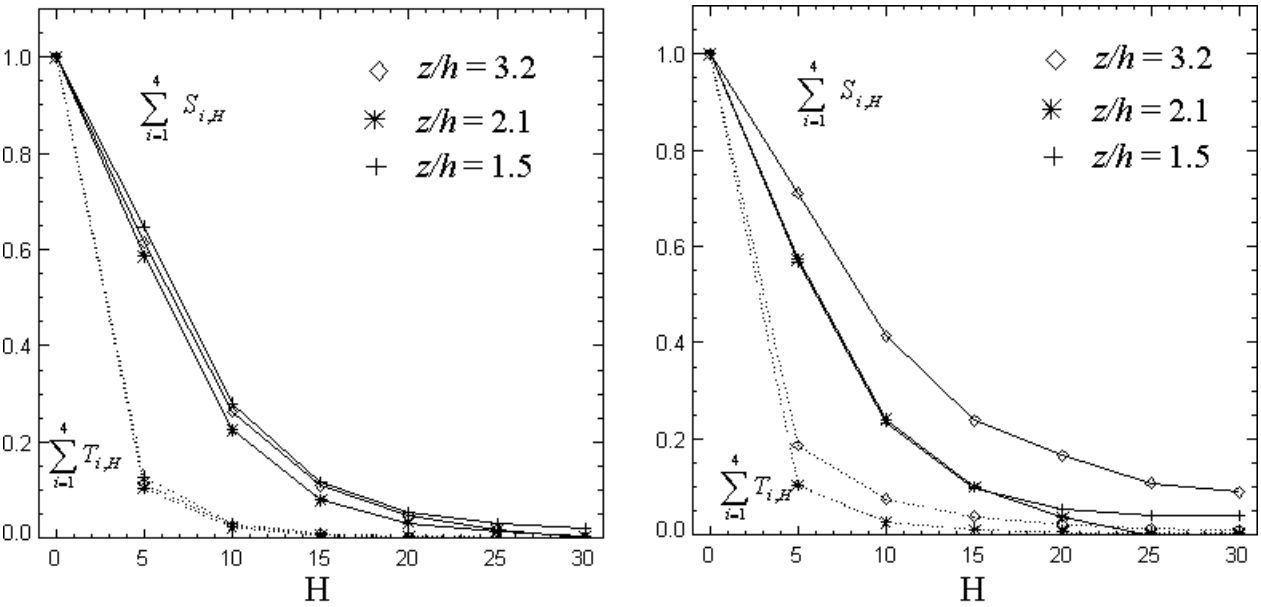

Fig 4.14: Cumulative magnitudes of flux fractions Σ*S(i,H)* (solid) and time fractions Σ*T(i,H)* (dashed) of momentum flux (left) and sensible heat flux (right) for varying hole size *H* and weakly unstable stratification $-0.5 < (z\text{-}z_d)/L < -0.05$.

For strongly unstable conditions, ejections contribute most to the total fluxes, for sensible heat flux, the interaction terms nearly vanish (fig. 4.15, right side). The large contributions to momentum flux from all quadrants are mainly due to the small values of the total flux for strongly convective conditions and it must be questioned, if the quadrant analysis is still representative for such conditions for momentum flux at all. The turbulent transport of sensible heat is fully dominated by organized motions at all measurement levels and ejections contribute the largest part to the total heat flux.

Rotach (1993a) reports positive values for ΔS_0 (a dominance of sweeps over ejections) up to his highest level at z/h=1.55. However, ΔS_0 becomes smaller and smaller with increasing distance from the roof level (0.051 at z/h=1.55). Compared to the decreasing values of ΔS_0 with increasing height in tab. 4.5 for all stability classes, this leads to the assumption, that the turnaround to a dominance of ejections over sweeps lies somewhere around z/h = 1.5. Shaw et al. (1983) and Shaw (1985) found sweeps dominating over ejections in transporting momentum up to z/h = 1.6 over a corn canopy and a wheat canopy (probably under near

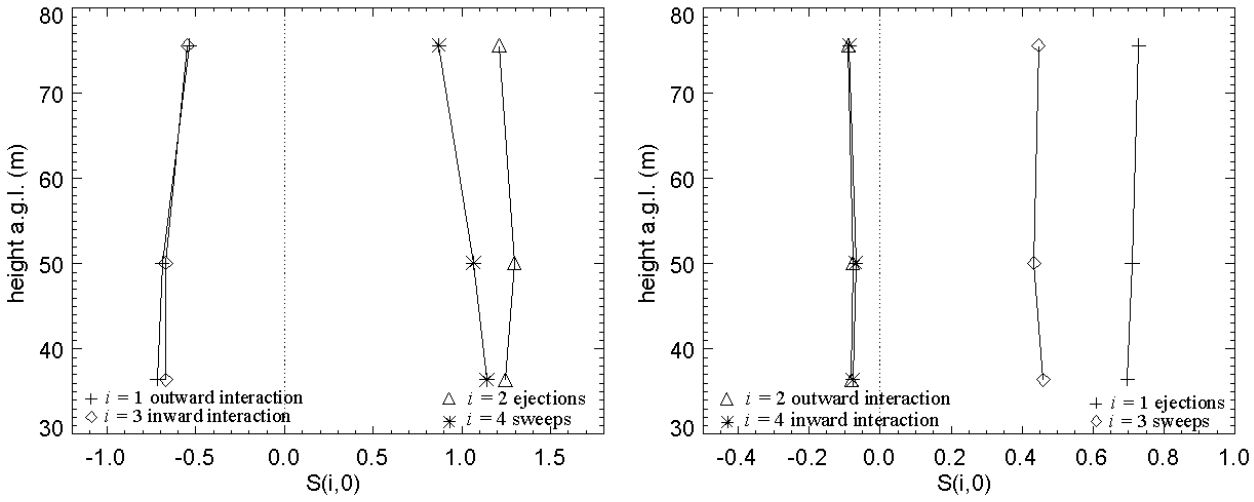

Fig 4.15: Averaged vertical profiles of momentum flux fractions (left) and sensible heat flux fractions (right) contributed by the four quadrants for unstable stratification $(z\text{-}z_d)/L < -0.5$.

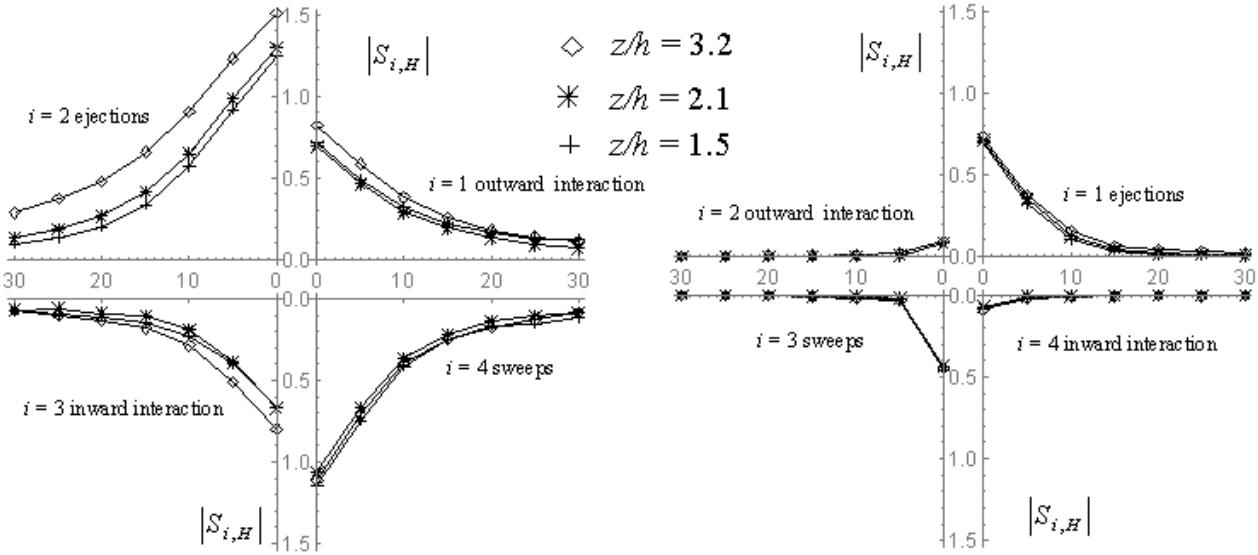

Fig 4.16: Contribution of stress fractions (left) and heat flux fractions (right) for varying hole size H and unstable stratification $(z\text{-}z_d)/L < -0.5$.

neutral conditions). Maitani and Othaki (1987) report sweeps to be more efficient in transporting heat and momentum for near neutral conditions, however, ejections become more efficient than sweeps for heat transport under very unstable conditions. Oikawa and Meng (1995) report a dominance of ejections for heights above $z/h = 1.5$ in a suburban area, in Bergström and Högström (1989) over a pine forest, the crossover takes place at $z/h = 2$. Relative contributions to sensible heat flux by sweeps were significantly larger than those by ejections in the canopy layer and roughness sublayer in Maitani and Shaw (1990) over a deciduous forest, whereas in the SL ($z/h = 2.4$), relative contributions of ejections were slightly larger than those by sweeps for heat and momentum under near neutral to slightly unstable conditions. Chen (1990) found similar results over natural malle bushland. At $z/h = 4$, sweeps and ejections contribute equal parts to the total flux of momentum and heat under neutral conditions, whereas under unstable conditions, ejections tend to be dominant for the transfer of heat and sweeps for momentum.

As shown above, an interpretation of the results of quadrant analysis depends highly on the stability conditions considered. Under unstable conditions, probably the most common situation in urban areas, ejections are the most efficient structures for the transport of sensible heat and momentum. If the transition from the RS to SL is equated to the turnaround of a dominance of ejections over sweeps under neutral conditions, this boundary lies

somewhere between $z/h = 2.1$ and $z/h = 3.2$ in the present study (fig. 4.11). However, the results from quadrant analysis in this study and from the studies mentioned above suggest, that the magnitude of the RS, or at least the height of the turnaround, depends strongly on stability.

4.4 Spectral analysis

In this chapter, the departure of the urban (co)spectra from the reference spectra (Kaimal et al., 1972) is investigated and the properties of the (co)spectra are compared to other urban studies. The three main points of the comparison are:

- the overall (co)spectral shape
- the position of the spectral peaks and derived length scales
- the slope of the (co)spectra in the inertial sub-range

The presented spectra and cospectra are normalized by their respective variances and co-variances and plotted against the non-dimensional frequency f. The averaged mean wind speed over all runs was 3.9 ms^{-1} at the uppermost level. Note that all spectra and frequencies are normalized by their local values. Spectral and cospectral peak frequencies are compared in tabs. 4.6 and 4.7 with other urban turbulence studies.

Additionally the well established Kansas spectra from Kaimal et al. (1972) for neutral conditions are plotted in the following figures for comparison. Note that the velocity spectra are scaled with the variance, whereas the Kansas spectra scale with u_*, this explains the differences in the power level. The slopes of -2/3 and -4/3 in the figures indicate the proportionality of the spectral and cospectral energy densities to the inertial subrange laws predicted by Kolmogorov's hypothesis.

4.4.1 Velocity spectra

In Figs. 4.17-18, the composite spectra of the wind components u, v and w are shown for all three measurement heights and the four stability classes according to table 4.5. In the inertial subrange they all follow the -2/3 slope. In contrast to the lateral and vertical velocity spectra, the spectra of the longitudinal velocity u in Fig. 4.17 do not exhibit a strong stability dependence. A peak shift to lower frequencies can be observed at each height as stratification becomes more unstable. Spectral peaks for weakly unstable conditions are in the region of $f_m \approx 0.044$ for $z/h = 3.2$ and shift to lower frequencies for all stability classes as we come closer to the roughness elements. Since $f_m = (z-d)/\lambda_m$ by virtue of Taylor's hypothesis, the dominant eddy scale or peak wavelength λ_m for the longitudinal component u ranges from 1200 m at $z/h = 3.2$ to 969 m at z/h=2.1 and 960 m at z/h=1.5 for weakly unstable conditions.

The spectra of the lateral and vertical wind components v and w in Figs. 4.17 and 4.18 show a clear stability dependence at all three measurement heights. Spectral energy densities for unstable conditions are significantly higher in the low frequency range and the spectral peaks are shifted to lower frequencies as instability increases. In the inertial subrange, the -2/3 slope is well established, but in contrast to the longitudinal wind component spectral densities in the inertial subrange are lowest for unstable conditions and they increase as stratification be-comes more and more stable. As observed with the u-spectra, the peak frequencies of the v- and w-spectra shift to lower values as z/h decreases. Peak frequencies f_m of v-spectra and w-spectra in the weakly unstable case are 0.131, 0.085 and 0.044 and 0.38, 0.31 and 0.25, respectively, from top to bottom. This corresponds to dominant lateral eddy scales λ_m of 412 m, 329 m and 318 m and of 141 m, 91 m and 58 m for their vertical extension.

Since the peak wavelengths λ_m decrease for all three wind components as we approach the surface from the uppermost measurement level, the dimensions of the dominant eddy structures become smaller. This is in best agreement with the results in Roth's (1999) review paper, where peak wavelengths (scaled with h) from several urban studies show the same behavior from $z/h = 0.91$ up to $z/h = 5.64$. The uppermost level is influenced strongly by large scale thermal structures in the surface (or even mixed) layer, where as the lowest level nearest to the roughness elements is strongly influenced by thermal updrafts and downdrafts of smaller scales linked to the heat sources/sinks and the geometrical properties of the urban surface. This supports the hypothesis also mentioned in Roth (1999) of a transition from a boundary layer scale dominated flow at larger heights to a regime close to the roughness elements, that responds primarily to canopy-layer plumes.

The peak frequencies of the uppermost level at $z/h = 3.2$ fit best to the surface layer reference spectra from Kaimal et al. (1972) for all three wind components, which suggests, that this measurement level is above the roughness sublayer within the inertial sublayer of the SL. In tab. 4.6, the observed spectral peak frequencies of wind components are compared to values reported in other urban studies. The scatter between the values for the same variable is quite large, but one has to consider the different measurement heights and the different „urban" surfaces. Roth and Oke (1993a) and Oikawa and Meng (1995) measured over relatively uniform suburban areas (mean building height $h = 8.5$ m and 7 m, respectively) with a

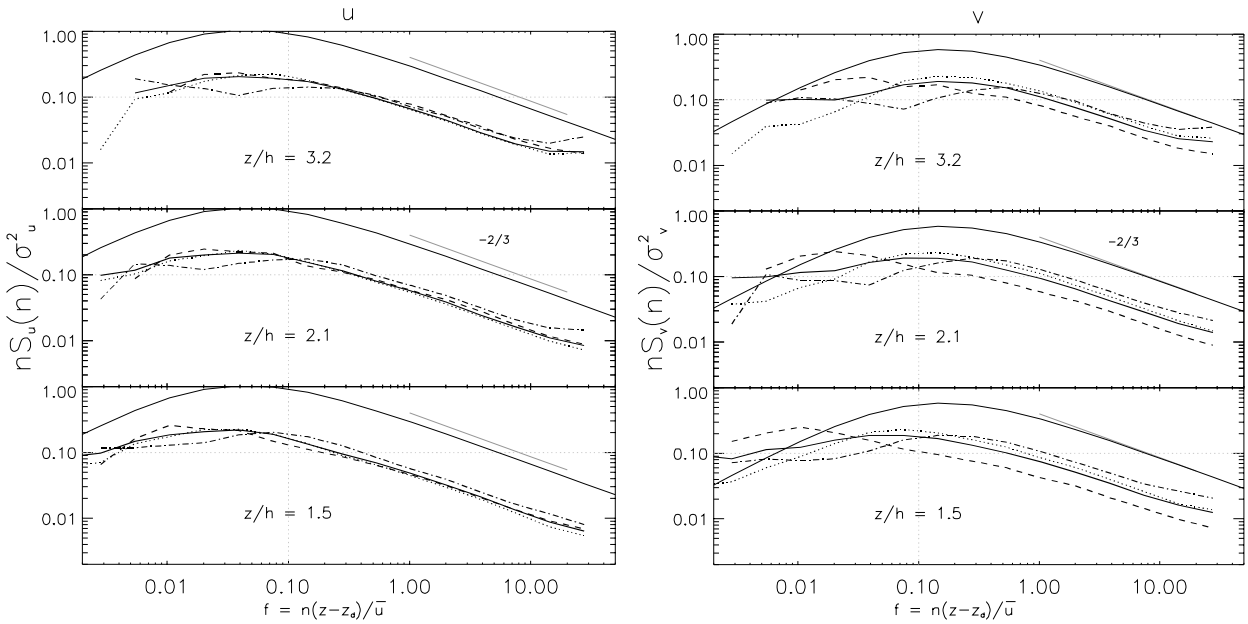

Fig. 4.17: Spectra of longitudinal wind component *u* (left) and lateral wind component *v* (right) for stable (dashed-dotted), neutral (dotted), weakly unstable (solid) and unstable (dashed) conditions. Reference spectrum from Kaimal et al. (1972) (solid thin).

percentage of area covered by buildings of about 25%, while Högström et al. (1982) and Rotach (1995) were investigating European cities (h = 15 m and 20 m, respectively) with about 50% of total area covered by buildings, which is similar to the present study. Additionally the number of runs analyzed in this study is significantly larger than in all studies mentioned above (see also tab. 4.6).

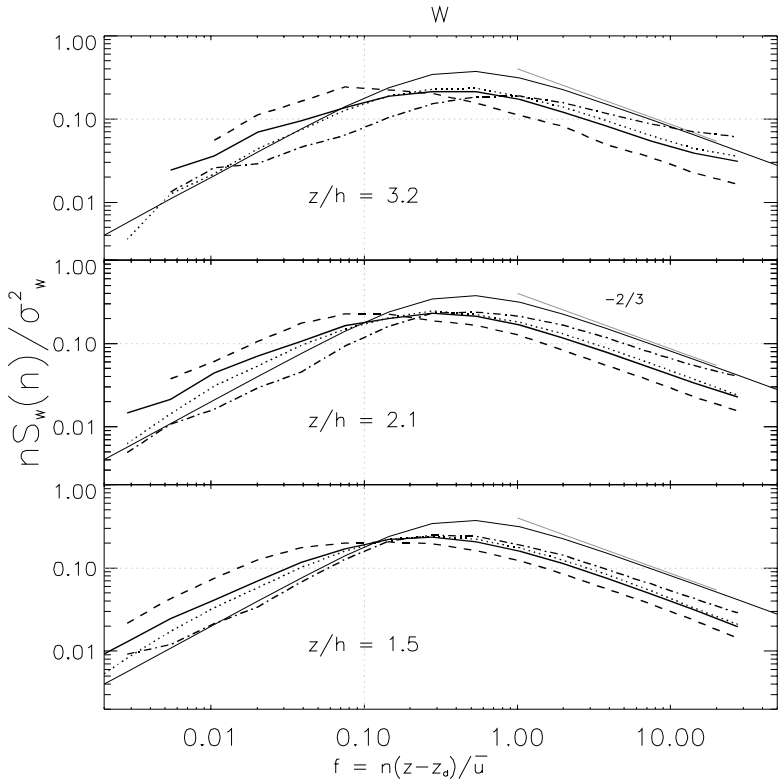

Fig. 4.18: As fig. 4.17 but for vertical wind component *w*.

Tab. 4.6: Spectral peak frequencies of wind components *u, v* and *w* above urban surfaces (except Kaimal et al., 1972) from various studies.

Study	Height	Peak frequency			Stability
	z/h	*u*	*v*	*w*	
Kaimal et al. (1972)		0.045	0.142	0.45	neutral
Rotach (1995)	1.55	0.1..0.2		≈ 0.65	$0>(z-z_d)/L>-1.$
	1.27	0.05..0.5		≈ 1.4	$0>(z-z_d)/L>-1.$
Högström et al. (1982)	3.5	0.053 ± 0.017	0.24 ± 0.037	0.54 ± 0.12	$-0.2<(z-z_d)/L<0.2$
	1.3	0.101 ± 0.039	0.11 ± 0.02	0.35 ± 0.08	$-0.2<(z-z_d)/L<0.2$
Oikawa and Meng (1995)	2.5	0.02..0.05		0.1..0.4	$-0.08>(z-z_d)/L>-0.23$
Roth and Oke (1993a)	2.65	≈ 0.02	≈ 0.14	≈ 0.15	$-0.05>(z-z_d)/L>-1.8$
This study	3.2	≈ 0.044	≈ 0.131	≈ 0.38	$-0.05>(z-z_d)/L>-0.5$
	2.1	≈ 0.029	≈ 0.085	≈ 0.31	$-0.05>(z-z_d)/L>-0.5$
	1.5	≈ 0.015	≈ 0.044	≈ 0.25	$-0.05>(z-z_d)/L>-0.5$

Horizontal and vertical velocity composite spectra exhibit the predicted -2/3 slope at the high frequency range and therefore, one could conclude, that an inertial subrange is observed within the urban roughness sublayer. As an additional test based on Kolmogorov's hypothesis concerning local isotropy in this frequency range, the ratio of the vertical to the longitudinal spectral energy densities $S_w(f)/S_u(f)$ is expected to approach 4/3. This ratio is drawn in fig. 4.19 for all measurement heights and stability classes. Note that the Kansas spectra are not adjusted to provide the 4/3 ratio (Kaimal and Finnigan, 1994). This is in good agreement with the $z/h = 3.2$ level, however, the $z/h = 1.5$ curve approaches the 4/3 line best. Rotach (1995) reported values for $S_w(f)/S_u(f)$ smaller than 1 at $z/h = 1.55$ and concluded, that there is no inertial subrange within the urban roughness sublayer. However the present data and the values from Högström et al. (1982), who reported $S_w(f)/S_u(f)$ ratios of 1.3 and 1.06 for $z/h = 3.5$ and $z/h = 1.3$, respectively, and Roth and Oke (1993a) (ratios of 1.2-1.4 for $z/h = 2.6$) suggest, that an inertial subrange could be established.

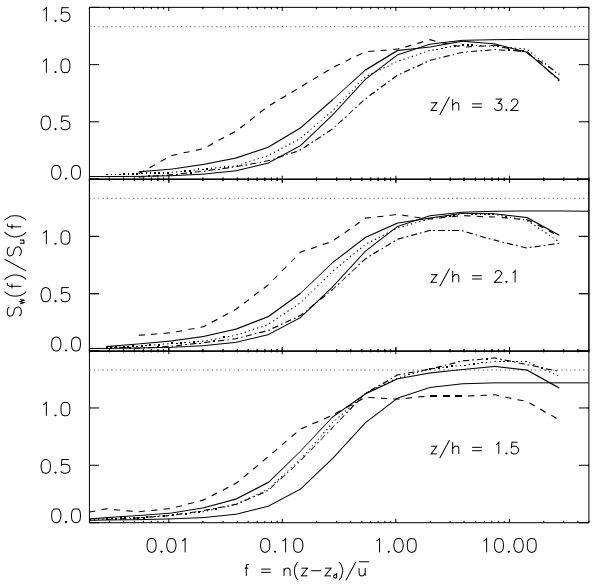

Fig. 4.19: As fig. 4.17 but for ratios of spectral energy densities $S_w(f)/S_u(f)$. Reference curve (solid thin) from Kaimal et al. (1972).

4.4.2 Temperature spectra

Temperature spectra in fig. 4.20 are generally ill-defined and flat for stable and neutral conditions at all heights and also for weakly unstable conditions at z/h=3.2. The increase of the spectral densities at the low frequency end of these spectra indicate a significant mesoscale component, which is also observed by Clarke et al. (1982). Rotach (1995) explains the higher spectral densities at low frequencies with warm bubbles rising sporadically from the street canyon. The fact that the increase of spectral densities at the low frequency end is most pronounced at the uppermost level supports the idea of a different thermal regime at the uppermost measurement level, caused by advection from areas with different surface characteristics and decoupled from the underlying surface, as supposed in a previous section, though the interpretation of temperature spectra must be made with caution. A striking feature of all temperature spectra is their increase at the high frequency end at all heights and stabilities at $f > 5$, which might reflect a (white) noisy signal, eventually caused by vibrations of the instrument. Normally, one would assign this effect to an aliasing of potential energy contained above the Nyquist frequency, however, the output signal is averaged internally from 8 measurement cycles, which should minimize aliasing effects (see Appendix A.2).

The -2/3 slope in the inertial subrange is only followed for unstable conditions, the corresponding peak frequencies are 0.085, 0.069 and 0.044 for z/h = 3.2, 2.1 and 1.5, respectively.

4.4.3 Cospectra

As for temperature spectra there are not many studies that deal with cospectra over urban surfaces. Some of the few are compared to this study in tab. 4.7. Because of the large scatter and occasional negative values, the curves for stable and strongly undstable conditions are not well formed and therefore they are nor plotted in fig. 4.21 for cospectra of *u'w'*. Cospectra of *u'w'* are well established for neutral and weakly unstable conditions, however the -4/3 slope is not given for the uppermost level in the inertial subrange and peak locations for the two lower levels are slightly shifted to lower values (Tab. 4.7). Cospectra of $w'\theta'$ in fig. 4.21 behave very similar to those of *u'w'*, again the curves are not well defined at all measurement levels for the stable stability class and at z/h = 3.2 and z/h = 2.1 for the neutral class. Nevertheless the reference cospectrum agrees almost perfectly in shape and peak frequency with the weakly unstable cospectra of the two lower levels, whereas the peak frequency for z/h = 3.2 is shifted to a higher value of $f_m \approx 0.16$. Compared to the velocity spectra, cospectra do not show that distinct height and stability dependence, what makes a clear interpretation difficult. However, since the peaks of both cospectra shift to higher frequencies for neutral and stable conditions as already observed for all three velocity components, it can be stated that smaller length scales are dominating the flow for this conditions. The dominating length scales λ_m derived from peak frequencies for the weakly unstable case are 635 m, 659 m and 254 m for *u'w'* and 337 m, 341 m and 164 m for $w'\theta'$ and z/h = 3.2, 2.1 and 1.5, respectively.

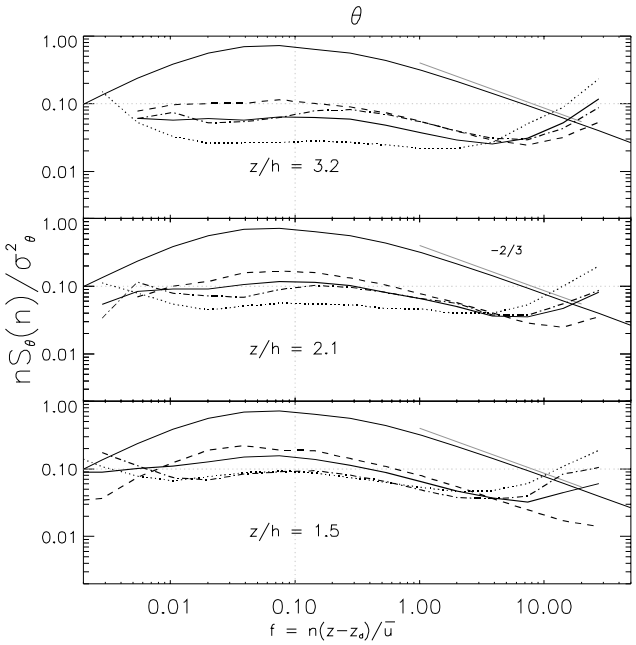

Fig. 4.20: As fig. 4.17 but for sonic temperature θ_s.

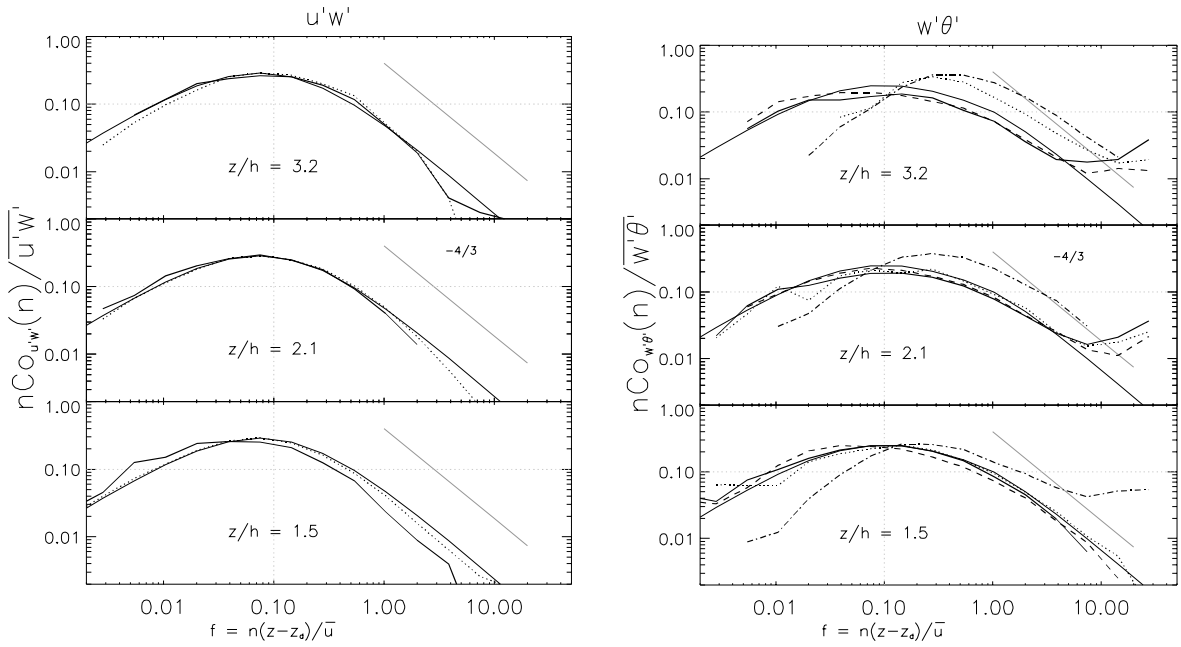

Fig. 4.21: As fig. 4.17 but for cospectra of *u'w'*.(left) and cospectra of *w'θ'* (right).

Table 4.7: (Co)spectral peak frequencies of temperature θ, momentum flux $\overline{u'w'}$ and kinematic heat flux $\overline{w'\theta'}$ above urban surfaces (except Kaimal et al., 1972) from various studies.

Study	Height	Peak frequency			Stability
	z/h	*θ'*	*u'w'*	*w'θ'*	
Kaimal et al. (1972)		0.063	0.07	0.09	neutral
Rotach (1991, 1995)	1.55	distorted	≈ 0.25	≈ 0.25	0> $(z-z_d)/L$ >-1.
Roth and Oke (1993a)	2.65	≈ 0.04	≈ 0.035	≈ 0.045	-0.05>$(z- z_d)/L$>-1.8
This study	3.2	distorted	≈ 0.085	≈ 0.16	-0.05>$(z- z_d)/L$>-0.5
	2.1	≈ 0.085	≈ 0.044	≈ 0.085	-0.05>$(z- z_d)/L$>-0.5
	1.5	≈ 0.068	≈ 0.055	≈ 0.085	-0.05>$(z- z_d)/L$>-0.5

4.5 Wavelet analysis

4.5.1 Meteorological conditions

The analysis has been done on a data set of 3 days from August 3 to 5 (day of year DOY 215-217) 1995. The essential meteorological parameters are presented in fig. 4.22. This period was characterized by nearly identical conditions for all three days. Net radiation ranged from a maximum of 550 Wm^{-2} at 13:00 h to a minimum of -90 Wm^{-2} right after sunset. Temperature maxima were around 29, minima around 17 degrees. With the high temperatures, the air was very dry, and there were extremely high sensible heat fluxes during the day

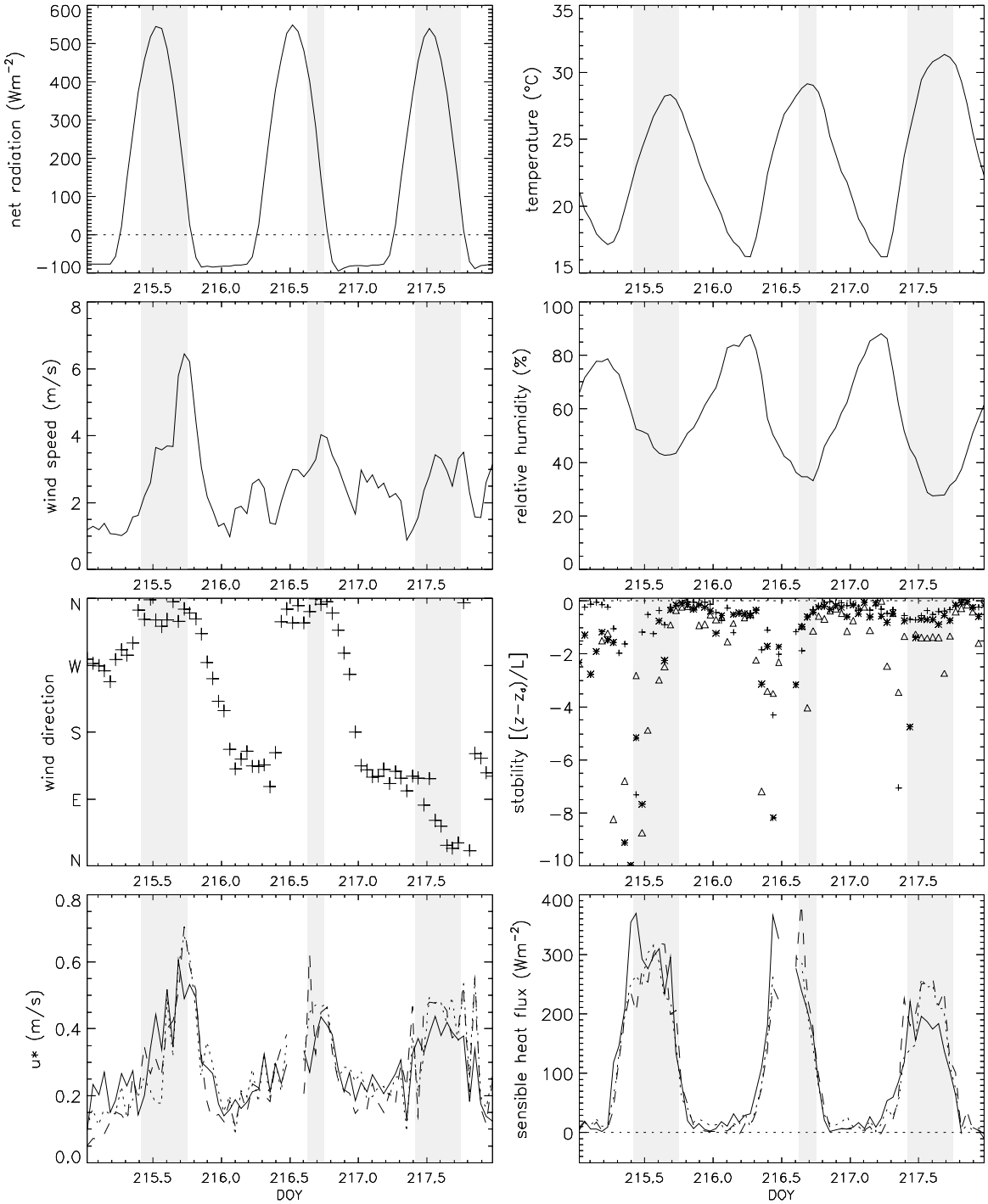

Fig. 4.22: Meteorological conditions from August 3 to 5 1995 (DOY 215-217). From top to bottom and from left to right: Net radiation, air temperature at *z/h*=1.5, wind speed at *z/h=3.2*, relative humidity at *z/h*=1.5, wind direction at *z/h*=3.2, stability index (+: *z/h*=1.5, ∗: *z/h*=2.1, Δ: *z/h*=3.2), u_* and sensible heat flux (solid: *z/h*=1.5, dotted: *z/h*=2.1, dashed-dotted: *z/h*=3.2). The periods selected for analysis are shaded.

(up to 70 percent of net radiation). Though there were no measurements of the latent heat flux, it is supposed, that evaporation was very small during these days, referring to studies dealing with heat storage in urban environments. For instance Roth and Oke (1994) measured and modeled the storage heat flux to be around 30 percent of net radiation during day over suburban terrain in summer; Grimmond and Oke (1995) observed storage heat fluxes of the same magnitude in four North American cities during clear sky conditions in summertime. A typical local feature is the diurnal pattern of the wind direction. During the night, we have a flow from the valleys in the south and the high rhine valley east of the city, turning to north in the late morning, when the stability becomes more and more unstable. See also fig. 3.1 for the topography of the site. This pattern can be observed on numerous days of the year, when the flow is ruled by autochthon clear sky conditions. Windspeed maxima were 6.6, 4.4 and 3.8 ms^{-1} for the three days in the late afternoon, when wind direction has changed to north. Mean wind speed for the whole period was 2.5 ms^{-1}. The friction velocity u_* of course strongly correlates with wind speed. Sensible heat flux was largest on the first two days under strong unstable conditions. For vertical profiles of u_* and sensible heat flux refer to section 4.1.

4.5.2 Event detection

By looking at the turbulence data of this period, one has to ask whether coherent structures exist in the time series at all. From Wilczak (1984) and Kaimal (1976), some well established characteristics for temperature ramps can be summed as follows:

- Large-scale eddies connected with temperature ramps exist in any strongly sheared environment.
- ramps generally have a continuous vertical structure over several Monin-Obukhov lengths *L*. Often ramps will merge in or even above the SL to form larger scale boundary layer thermals
- ramps in general propagate in the direction of the mean wind
- the longitudinal ramp size is strongly dependent on Monin-Obukhov length *L*, with increasing ramp size as instability increases

If we look at the arbitrarily chosen temperature time series in fig. 4.23, we truly find cases where periods of slow increase followed by an abrupt decrease can be detected by eye. These ramps occur simultaneously at all three levels but also isolated at just one or two levels (but always at the lowest level). For this study, we concentrate on simultaneous events at all three levels, because we are interested in the main structures that dominate the flow. Figures 4.24 and 4.25 show the wavelet scalograms of an arbitrarily chosen 53 minutes temperature run as well as the time series itself. For presentation purposes, the data have been smoothed by a 5 s running mean.

The three windows represent the measurements at z/h = 3.2, 2.1 and 1.5 from top to bottom respectively. Looking at the time series in the lower part of the figure, it can be observed, that sonic temperature fluctuations θ' behave most of the time very similar and simultaneously at all three levels, however the amplitude of the fluctuations becomes smaller with increasing height. There are active periods alternating with more quiescent phases. Ramp patterns can be detected by eye, though the idealized shape of the artificial data set is of course not always given.

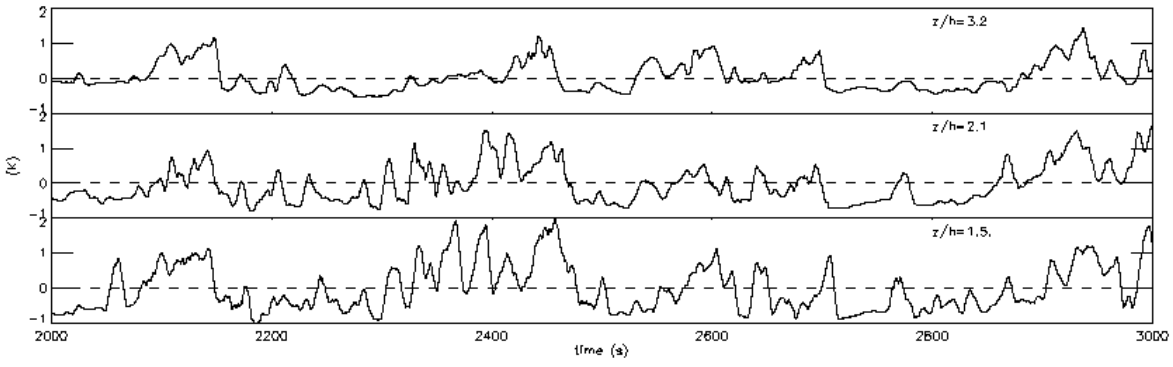

Fig. 4.23: Arbitrarily chosen time series of temperature fluctuations θ '. The three windows refer to z/h = 3.2, 2.1 and 1.5 (from top to bottom).

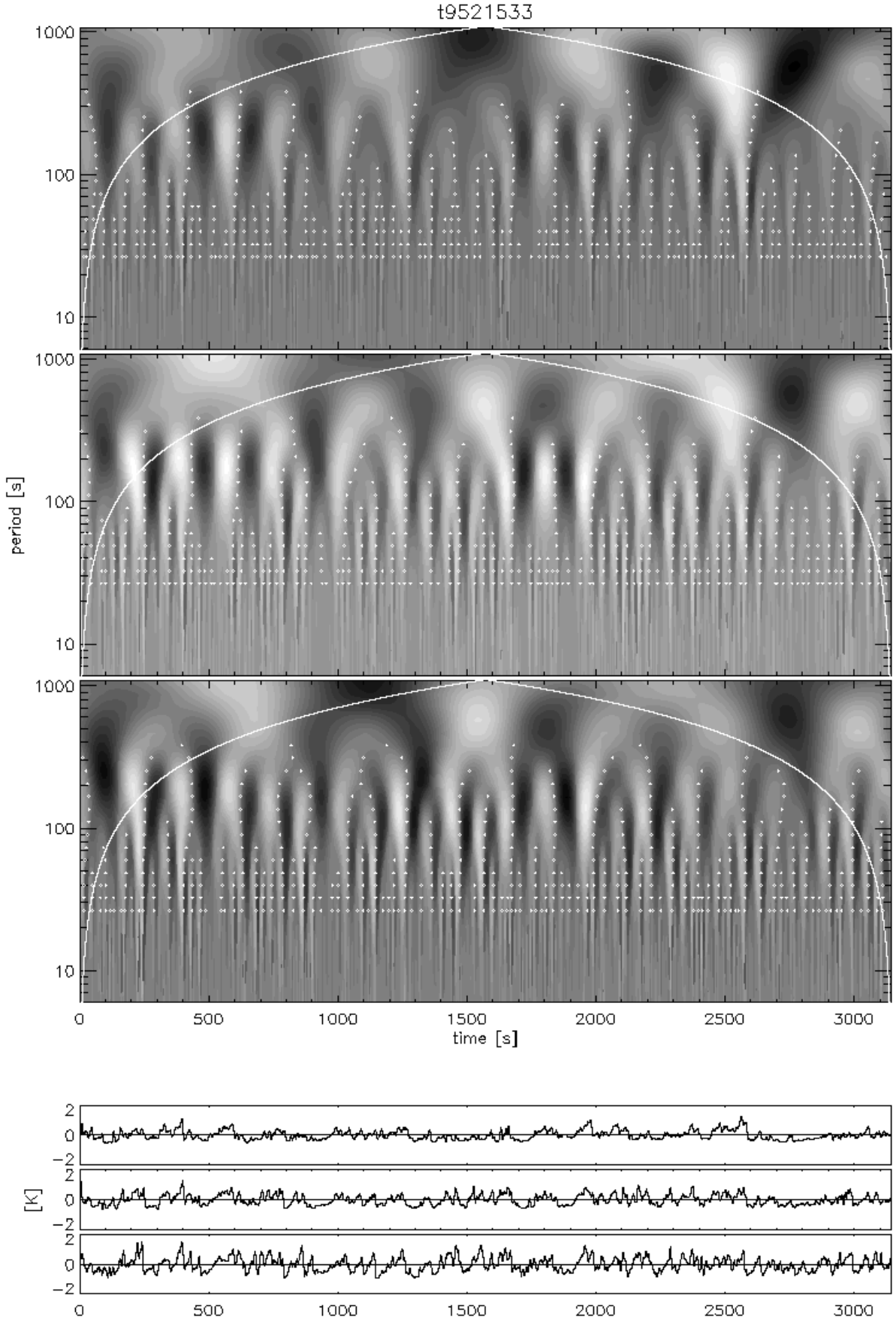

Fig. 4.24: Temperature fluctuations θ' (bottom) and corresponding wavelet scalograms (top) for DOY 215, 16:00-16:53. The three windows refer to z/h=3.2, 2.1 and 1.5 (from top to bottom).

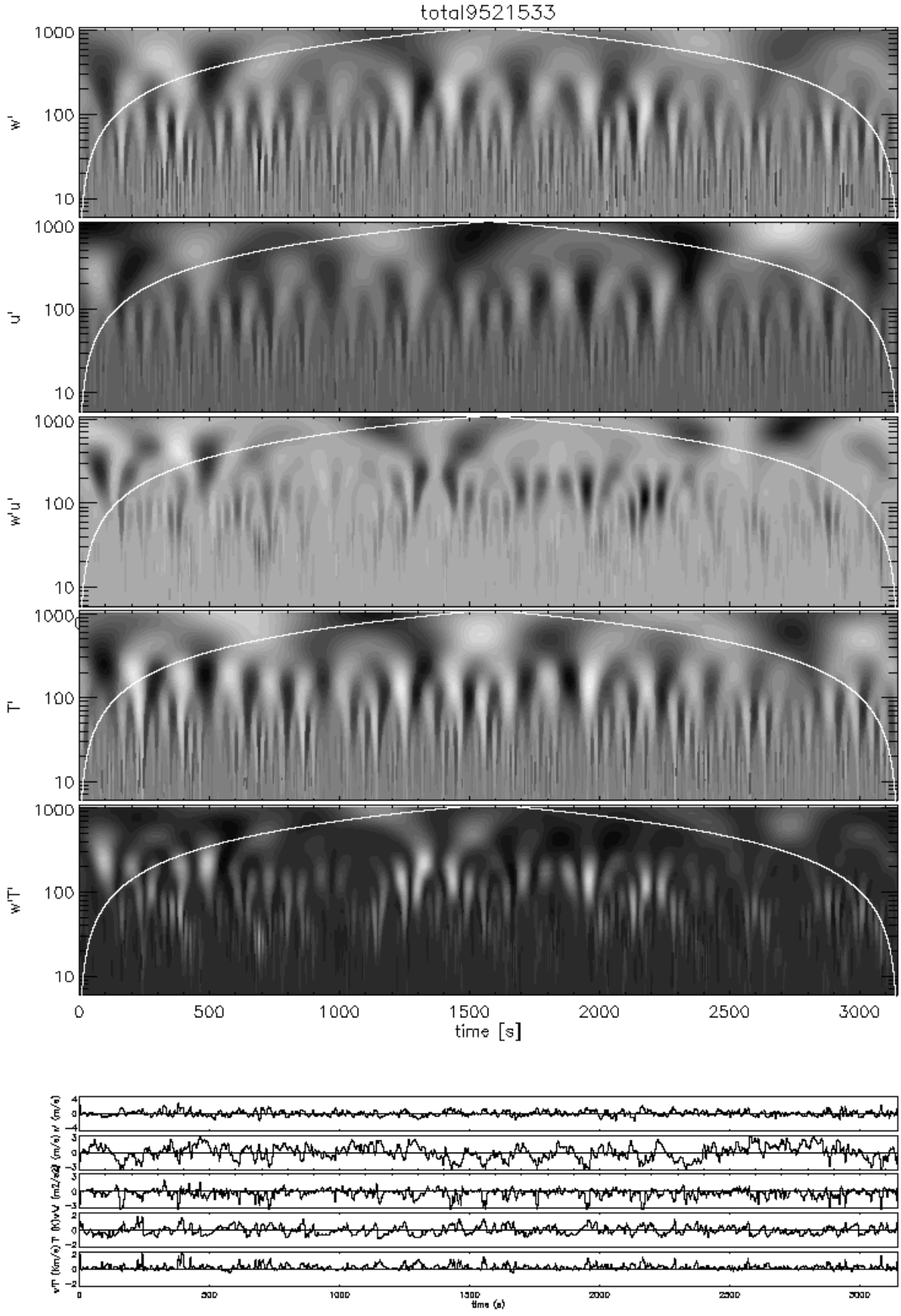

Fig. 4.25: Wavelet scalograms (top) and time series (bottom) for DOY 215, 16:00-16:53 at z/h = 1.5. The five windows refer to *w', u', θ ', u'w'* and *w'θ'* (from top to bottom).

In the scalograms, ramps are characterized by a sharp transition from light to dark colors (zero crossovers with negative slope) and symbols at scales (periods) from 25 to 380 seconds. At a first glimpse, scalograms look very similar at large scales at all three levels, which means, that the fluctuations have somehow to be organized and related to each other.

A comparison of the scalograms of the parameters w', u', θ', $u'w'$, $w'\theta'$ is shown in fig. 4.25 for the z/h = 1.5 level. It is interesting to see, how the fluctuations in u' and $u'w'$ contribute most to the energy at large time scales, whereas the other parameters show strong fluctuations also at periods lower than 40 seconds.

The smaller the scale, the more events are detected as the symbols indicate in fig. 4.24. It is now necessary to determine the dominant scale, that contributes most to the energy of the signal, because this value is needed for the ramp detection method. This can be done by analyzing the Fourier and/or the wavelet spectra of the temperature time series. It is supposed that the spectra have a well defined peak which corresponds to the dominant frequency or time scale.

The turbulence conditions during the selected periods did not change very much (tab. 4.9-11), what justifies displaying results as averages over the selected runs. Wavelet and Fourier spectra (fig. 4.26-28) agree fairly well, again, the smoother shape of the wavelet spectra in the low frequency range can be observed. From peak frequencies of θ'-spectra at z/h = 1.5, the dominant time scale for ramp detection was determined to be around 90 seconds for all three days.

Table 4.8 compares the results found in other studies dealing with the subject of dominating time scales. The higher the roughness elements and the rougher the surface, the larger are the dominating time scales. Considering the results in Tab. 4.8, the 90 seconds found in this study seem to be a very reasonable value.

Tab. 4.8: Comparison of dominating time scales in other studies

Study	surface	canopy height	dominating time scale
Gao et al. (1992)	deciduous forest	18 m	50 s
Bergström and Högström (1989)	pine forest	20 m	33 – 40 s
Paw U et al. (1992)	maize crop	2.6 m	8 – 15 s
Collineau and Brunet (1993b)	pine forest	13.5 m	10 – 15 s
Brunet and Collineau (1994)	maize crop	1.55 m	5 – 7 s
Oikawa and Meng (1995)	suburban	7 m	80 s
this study	urban	24 m	90 s

Tab. 4.9: Meteorological conditions for the analyzed runs of DOY 215

LST	θ	rh	$\overline{u}$	α	u_*			$\overline{w'\theta'}$			$(z-z_d)/L$		
					z/h=1.5	z/h=2.1	z/h=3.2	z/h=1.5	z/h=2.1	z/h=3.2	z/h=1.5	z/h=2.1	z/h=3.2
11:00	23.52	0.52	2.20	331	0.20	0.25	0.35	0.306	0.220	0.169	-7.30	-5.16	-2.81
12:00	24.73	0.52	2.60	358	0.34	0.22	0.27	0.243	0.207	0.225	-1.18	-7.67	-8.74
13:00	25.98	0.51	3.66	331	0.44	0.18	0.31	0.228	0.250	0.210	-0.51	-16.39	-4.88
14:00	27.19	0.46	3.57	322	0.34	0.18	0.26	0.246	0.262	0.250	-1.24	-17.77	-10.56
15:00	28.01	0.43	3.69	331	0.52	0.49	0.40	0.257	0.239	0.266	-0.36	-0.75	-2.98
16:00	28.59	0.43	3.68	355	0.35	0.32	0.42	0.194	0.189	0.263	-0.91	-2.25	-2.47
17:00	28.73	0.43	5.79	329	0.61	0.59	0.51	0.246	0.185	0.165	-0.21	-0.34	-0.90
18:00	28.31	0.43	6.45	345	0.49	0.68	0.70	0.112	0.126	0.171	-0.18	-0.15	-0.35

Tab. 4.10: Meteorological conditions for the analyzed runs of DOY 216

LST	θ	rh	$\overline{u}$	α	u_*			$\overline{w'\theta'}$			$(z-z_d)/L$		
					z/h=1.5	z/h=2.1	z/h=3.2	z/h=1.5	z/h=2.1	z/h=3.2	z/h=1.5	z/h=2.1	z/h=3.2
16:00	29.20	0.35	2.99	342	0.27	0.45	0.62	0.196	0.239	0.320	-1.92	-1.00	-0.97
17:00	29.47	0.35	3.29	359	0.38	0.47	0.32	0.171	0.169	0.194	-0.62	-0.61	-4.11
18:00	29.37	0.33	4.04	351	0.43	0.47	0.45	0.138	0.118	0.145	-0.32	-0.44	-1.15

Tab. 4.11: Meteorological conditions for the analyzed runs of DOY 217

LST	θ	rh	$\overline{u}$	α	u_*			$\overline{w'\theta'}$			$(z-z_d)/L$		
					z/h=1.5	z/h=2.1	z/h=3.2	z/h=1.5	z/h=2.1	z/h=3.2	z/h=1.5	z/h=2.1	z/h=3.2
11:00	26.22	0.45	1.55	118	0.37	0.21	0.13	0.183	0.117	0.149	-0.70	-4.75	-44.13
12:00	27.85	0.42	2.37	82	0.33	0.32	0.46	0.129	0.123	0.165	-0.71	-1.38	-1.24
13:00	29.82	0.35	2.80	117	0.39	0.49	0.48	0.163	0.215	0.207	-0.56	-0.68	-1.37
14:00	30.63	0.29	3.43	61	0.44	0.48	0.48	0.155	0.203	0.209	-0.36	-0.71	-1.39
15:00	31.18	0.27	3.31	53	0.38	0.48	0.49	0.145	0.207	0.216	-0.51	-0.70	-1.36
16:00	31.40	0.28	2.95	27	0.42	0.42	0.45	0.152	0.173	0.178	-0.40	-0.88	-1.37
17:00	31.62	0.28	2.50	23	0.39	0.50	0.37	0.113	0.173	0.198	-0.37	-0.56	-2.71
18:00	31.41	0.31	3.31	31	0.37	0.37	0.38	0.086	0.096	0.105	-0.33	-0.74	-1.32

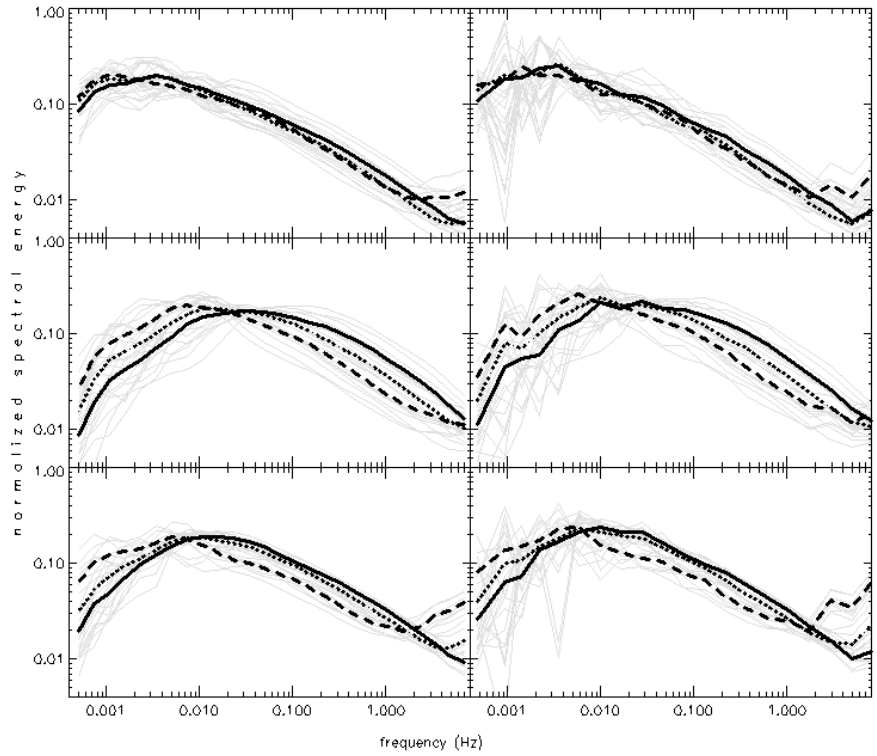

Fig. 4.26: Wavelet (left) and Fourier spectra of *u'*, *w'* and *θ'* (top to bottom) for the period from 10:00 to 18:00 on DOY 215. Measurements at *z/h*: solid line = 1.5, dotted line = 2.1 and dashed line = 3.2. Displayed are averages of spectra based on hourly runs (background, light gray).

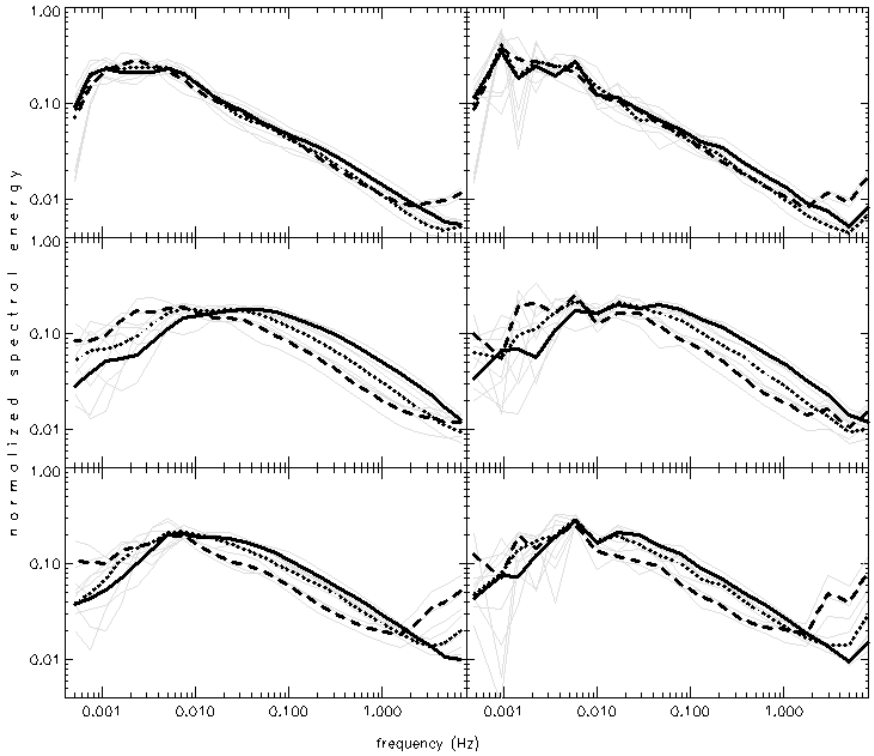

Fig. 4.27: Wavelet (left) and Fourier spectra of *u'*, *w'* and *θ'* (top to bottom) for the period from 15:00 to 18:00 on DOY 216. Measurements at *z/h*: solid line = 1.5, dotted line = 2.1 and dashed line = 3.2. Displayed are averages of spectra based on hourly runs (background, light gray).

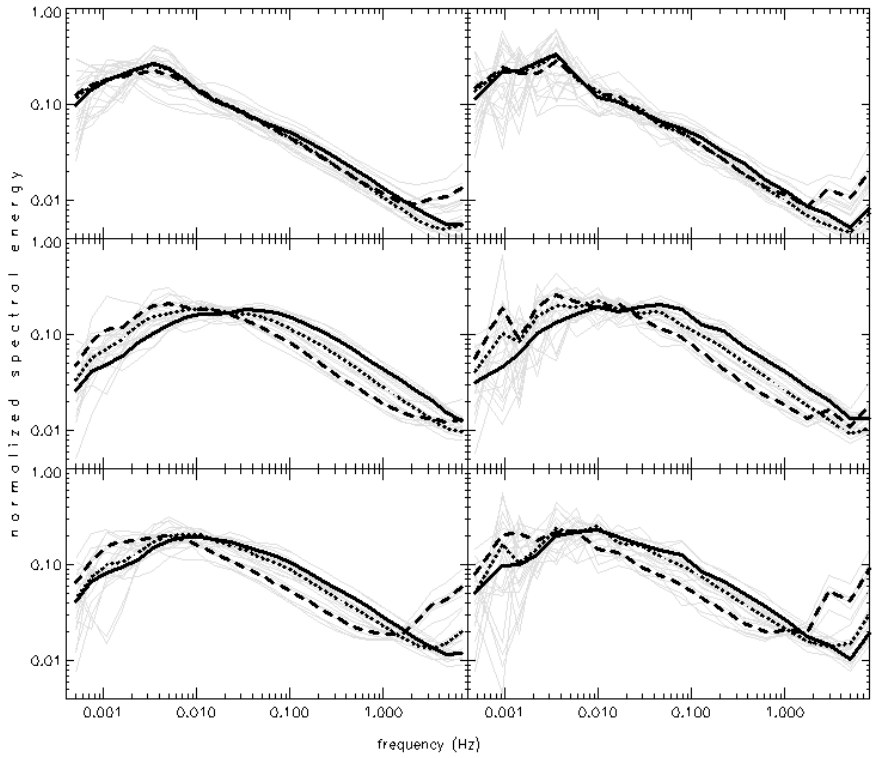

Fig. 4.28: Wavelet (left) and Fourier spectra of *u', w'* and *θ'* (top to bottom) for the period from 10:00 to 18:00 on DOY 217. Measurements at *z/h*: solid line = 1.5, dotted line = 2.1 and dashed line = 3.2. Displayed are averages of spectra based on hourly runs (background, light gray).

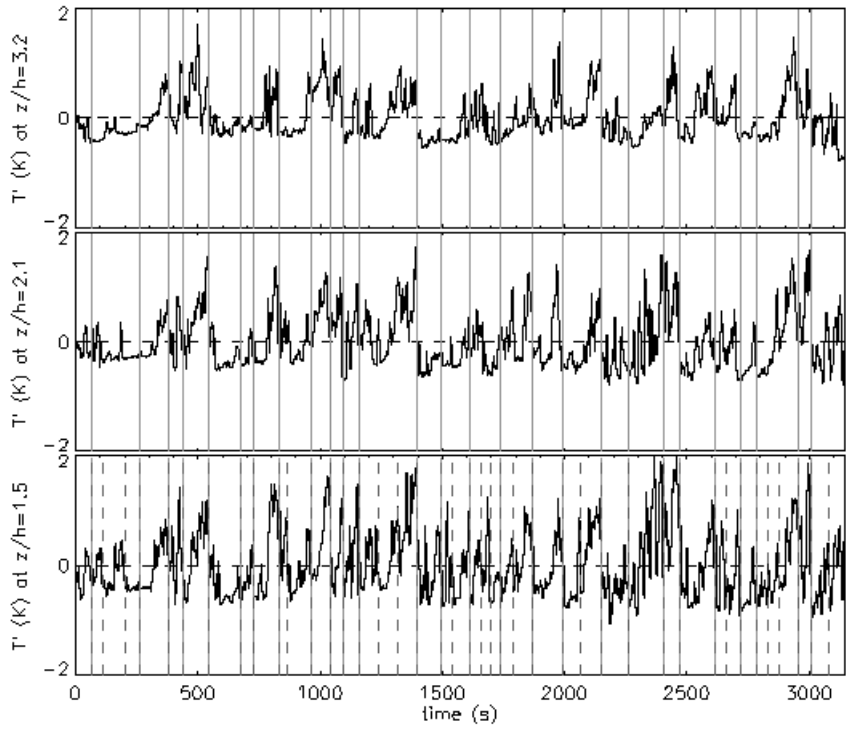

Fig. 4.29: Time series of temperature fluctuations *θ'* (filtered by a 5 s running mean) at *z/h* = 3.2, 2.1 and 1.5 (from top to bottom) on DOY 215, 14:00-14:53. Solid lines indicate the detected events taken for conditional sampling. Dashed lines are detected events at *z/h* = 1.5, that do not have corresponding temperature ramps above.

Tab. 4.12: Statistics of event detection for DOY 215 and 217

DOY	hour	Δt_{ev}	N_{ev}	DOY	hour	Δt_{ev}	N_{ev}
215	11:00	131 ± 77 s	20	217	11:00	182 ± 158 s	15
	12:00	167 ± 125 s	17		12:00	198 ± 87 s	15
	13:00	120 ± 61 s	24		13:00	164 ± 129 s	17
	14:00	113 ± 47 s	26		14:00	174 ± 123 s	16
	15:00	137 ± 64 s	21		15:00	162 ± 117 s	18
	16:00	127 ± 62 s	23		16:00	166 ± 156 s	18
	17:00	106 ± 73 s	27		17:00	137 ± 63 s	21
	18:00	87 ± 47 s	33		18:00	145 ± 60 s	20

To demonstrate the success of the detection method, an arbitrarily chosen temperature time series and the detected ramps are shown in fig. 4.29. Considering the chaotic nature of turbulence, the zero-crossing method detects temperature ramps surprisingly well. As mentioned above, only events occurring simultaneously (± 15 seconds) at all three levels are taken for conditional sampling, the detected ramps indicated by the dashed lines at $z/h = 1.5$ have been skipped.

The most important point of interest derived from detection statistics is the mean time-interval between events, Δt_{ev} and, of course, the number of detected events per run, N_{ev}. These statistics are printed in tab. 4.12. Though the mean duration between events is in a reasonable range, the large standard deviations suggest, that there are series of consistent events (of period slightly shorter than Δt_{ev}) followed by longer "quiescent" periods without events. Thus Δt_{ev} only gives a crude idea of the distribution of temperature ramps during a single run and is of course dependent on the number of detected events N_{ev}. N_{ev} itself shows a moderate run-to-run variation. It must be stated, that there are always some missed or false detections. Such a false detection can be observed in fig. 4.29 at around 250 seconds. In any case, they do not affect the result significantly, since all detected events are averaged and the main structures are obviously catched by the detection algorithm, as can be seen in fig. 4.29.

4.5.3 First-order moments

First-order moments $\langle u' \rangle$, $\langle w' \rangle$ and $\langle T' \rangle$ of the chosen runs are now ensemble-averaged andFirst-order moments $\langle u' \rangle$, $\langle w' \rangle$ and $\langle T' \rangle$ of the chosen runs are now ensemble-averaged and normalized according to eq. (2.63) in order to get more insight to the organized structures. Figures 4.30-35 show the ensemble averages for the selected runs of DOY 215, 216 and 217, respectively. All levels show a characteristic rise in temperature during a slow upward ($\langle u' \rangle < 0$, $\langle w' \rangle > 0$) flow of (warmer) air, followed by a sharp drop of temperature in the center of the time window, which corresponds to the detection point. This drop is associated with an acceleration of the horizontal wind speed and a downward motion ($\langle u' \rangle > 0$, $\langle w' \rangle < 0$) of (cooler) air. The first part of this structure is usually referred to as 'ejection' or 'burst', where as the second stage is referred to as 'sweep' or 'gust' (see also chapter 2.5). These patterns are well established in literature and observed in turbulent boundary layers over different types of canopies and in laboratory experiments.

As expected, the ejection sweep cycle is best established at $z/h = 1.5$, since the detection algorithm was performed at this level. The amplitude of temperature ramps and streamwise wind speed are highest at this level, whereas the intensity of updraft and downdraft is about the same at all three levels. Temperature fluctuations behave similar to and simultaneously with the vertical velocity trace. A phase shift can be observed in the horizontal velocity trace, where acceleration starts slightly before temperatures begin to fall.

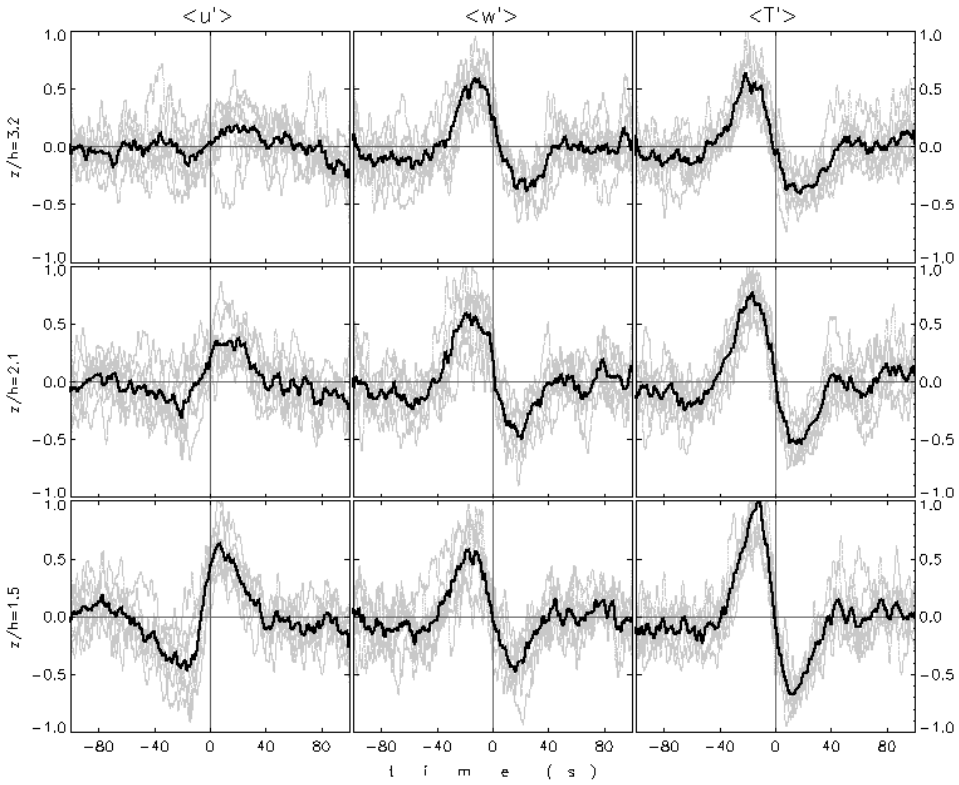

Fig. 4.30: Superimposed conditional averages (light gray), normalized by the corresponding standard deviation for $\langle u' \rangle$, $\langle w' \rangle$ and $\langle T' \rangle$ (left to right) at z/h = 3.2, 2.1 and 1.5 (from top to bottom) for 8 runs from 10:00-18:00 on DOY 215. Solid thick lines indicate the over-all average.

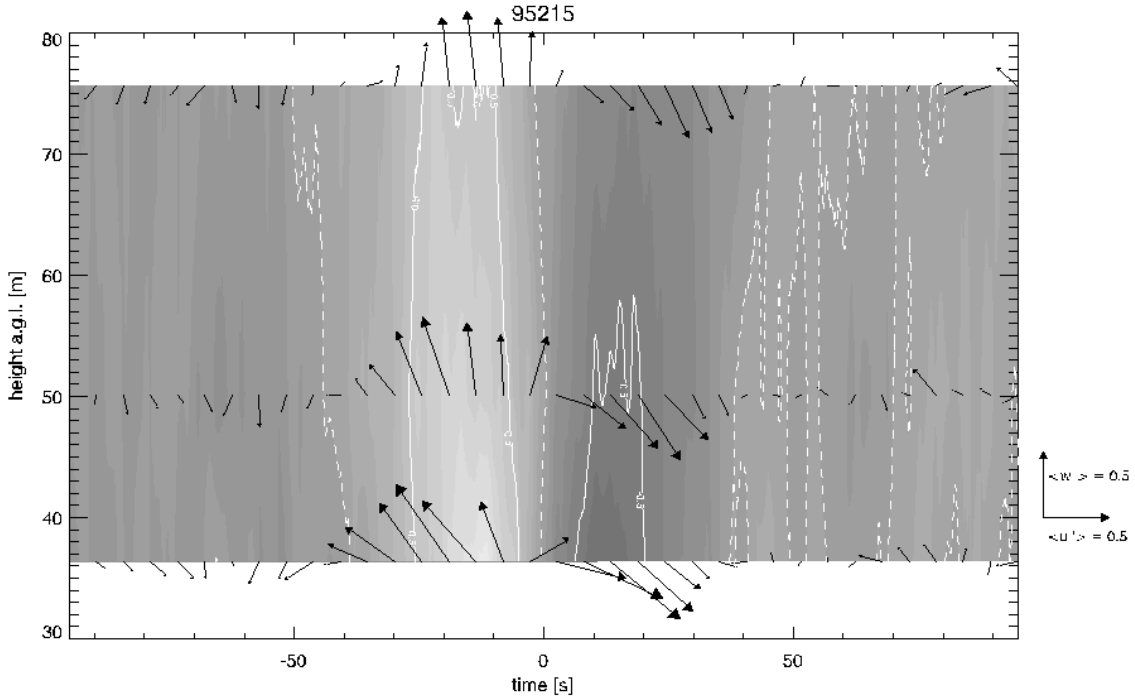

Fig. 4.31: Averaged pattern of ejection-sweep cycles from DOY 215. Contours represent $\langle T' \rangle$ values (light colors positive, dark colors negative, contour lines: solid: ± 0.5, dotted: 0.0). Arrows correspond to $\langle u' \rangle$ (horizontal component) and $\langle w' \rangle$ (vertical component). All values are normalized by their respective standard deviation.

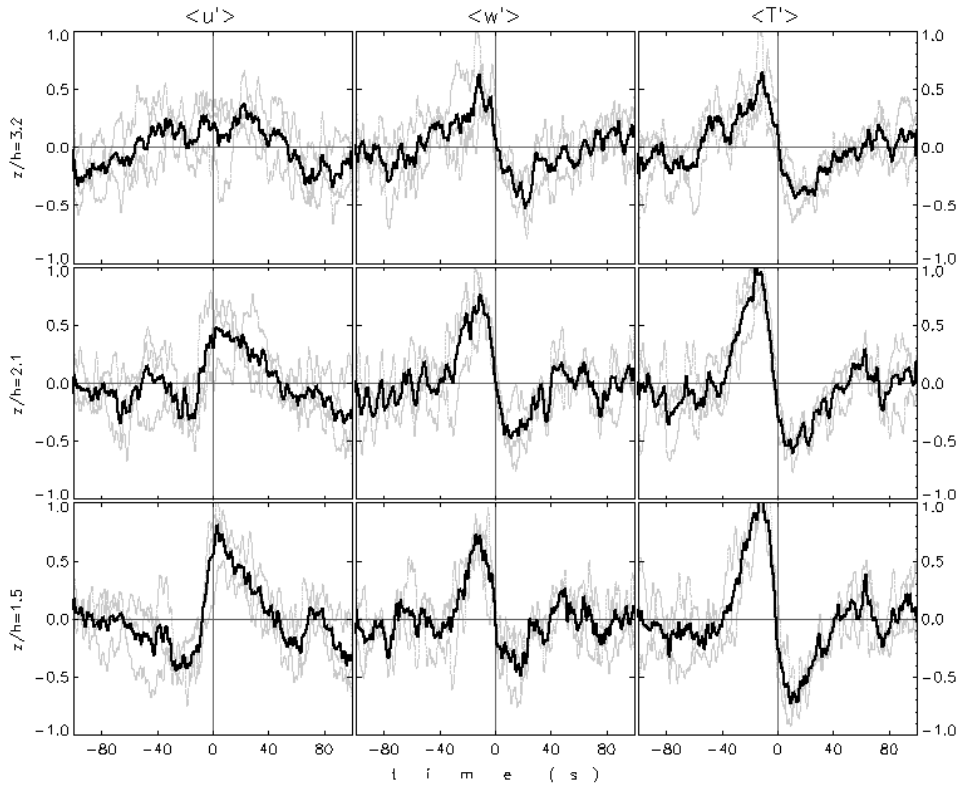

Fig. 4.32: As fig. 4.30 but for DOY 216, 15:00-18:00

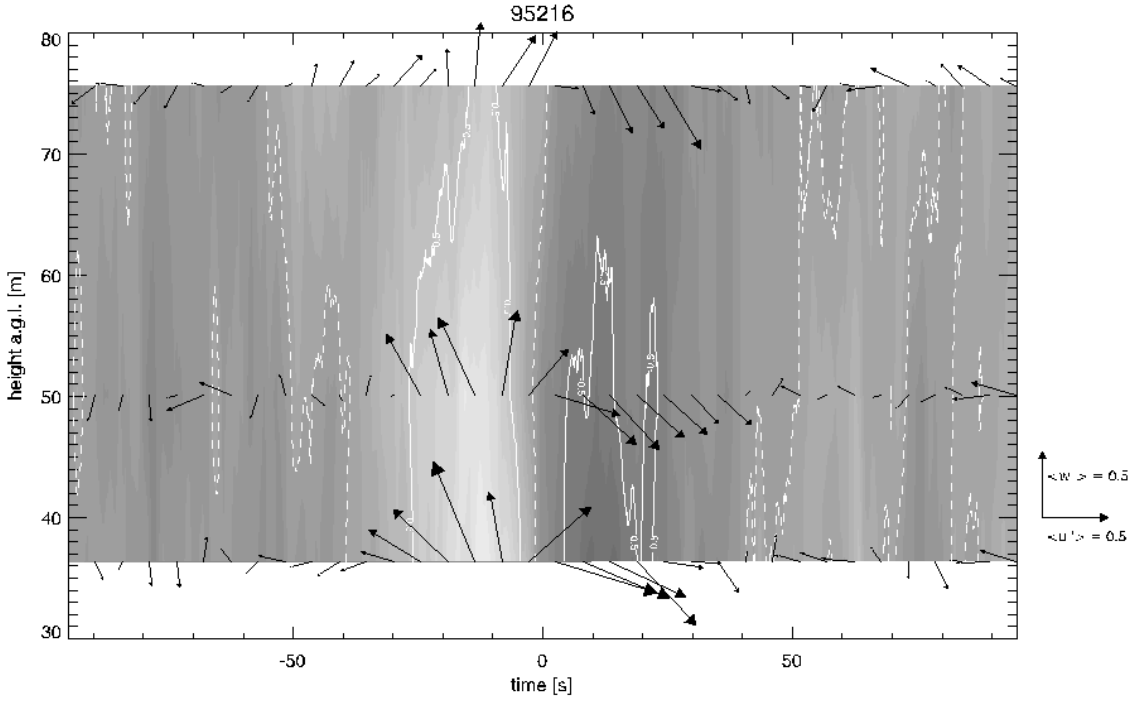

Fig. 4.33: As fig. 4.31 but for DOY 216, 15:00-18:00

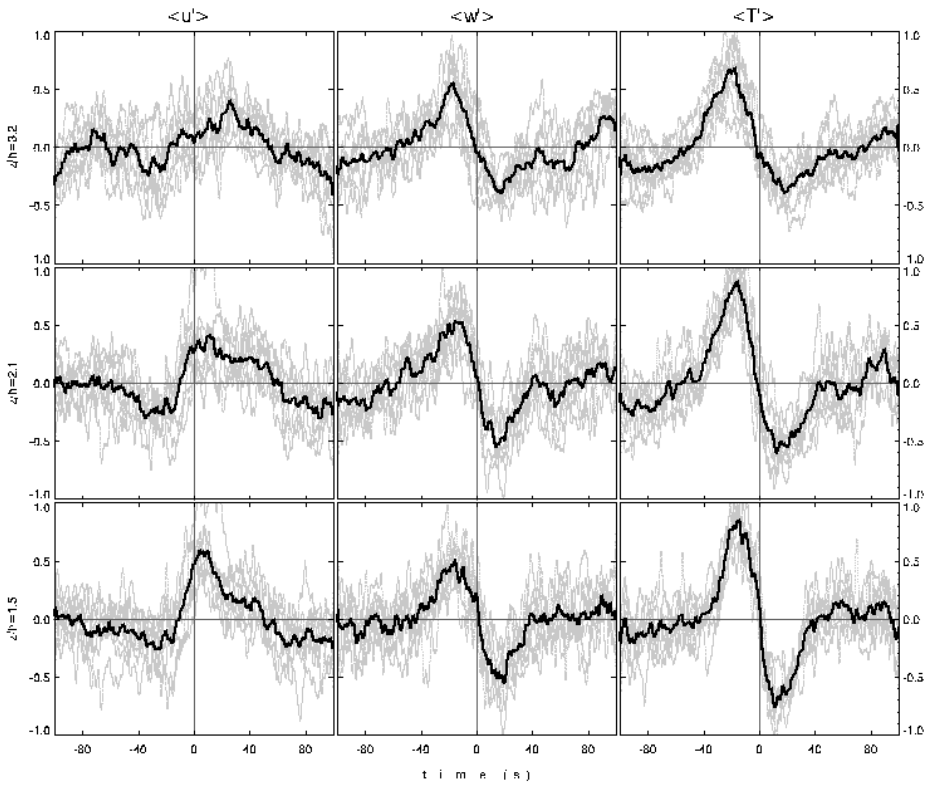

Fig. 4.34: As fig. 4.30 but for DOY 217, 10:00-18:00

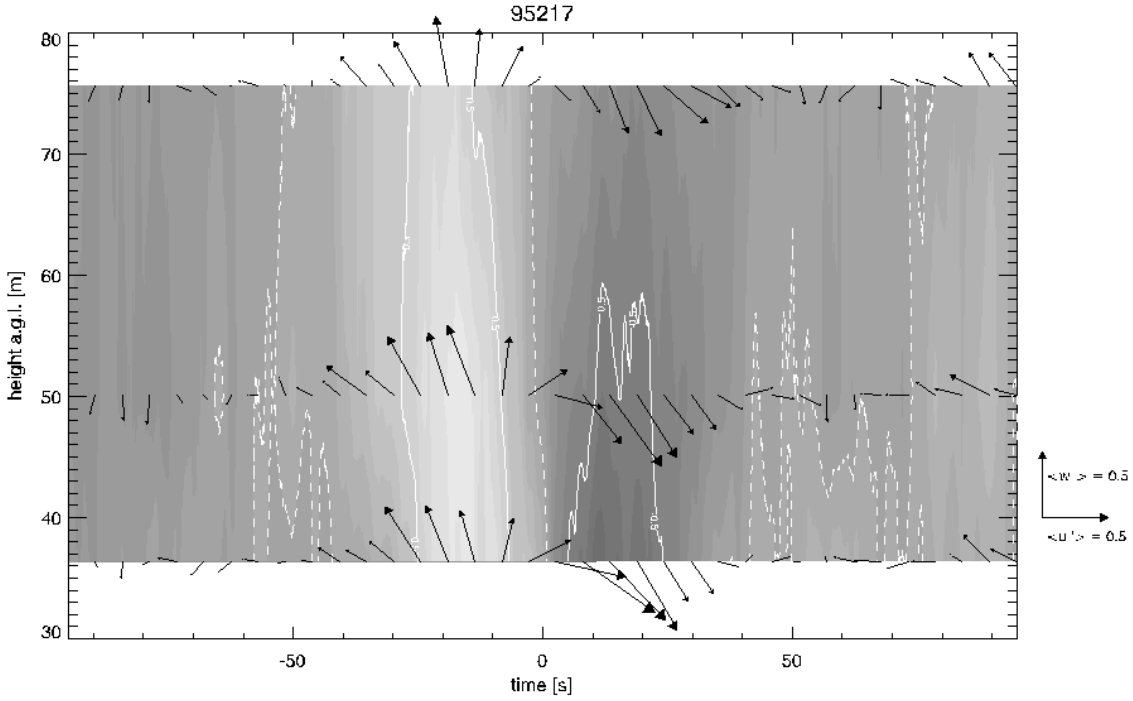

Fig. 4.35: As fig. 4.31 but for DOY 217, 10:00-18:00

There are some remarkable features considering the patterns of the organized structures in figs. 4.30-35:

- The acceleration of the streamwise wind velocity $\langle u' \rangle$ in accordance to the dropping temperatures is not well established at z/h=3.2, while $\langle w' \rangle$ and $\langle T' \rangle$ behave like known from other studies over vegetation canopies. The reason for this is unclear. Again, this level behaves like decoupled from the underlying layer. Since conditional sampling is applied only in a few urban studies, and if at all, mostly by quadrant analysis (Rotach, 1991) or by detection by eye (Oikawa and Meng, 1995), no comparable data sets are available.
- Practically no time lag in the vertical temperature profiles of the organized motions is observed. A time lag would be manifested in figs. 4.30, 4.32 and 4.33 by a tilt of the 0°-isotherm, which is not observable in our case. Downwind inclined microfronts manifested in the temperature traces are reported for example in Gao et al. (1992), Shaw and Zhang (1992) and Collineau and Brunet (1993b). However, these studies are made over vegetation canopies up to heights of $z/h = 2.4$ (Shaw and Zhang, 1992), $z/h = 1.9$ (Gao et al., 1992) and $z/h = 1.24$ (Collineau and Brunet (1993b)) and only a few selected events and runs have been considered. Also, the sharpest tilt is always reported within and immediately above the canopy (say between $z/h = 1$ to $z/h = 2$). Additionally, the sharp tilt of single events is smoothed by the averaging process (Gao et al., 1992). Since our lowest level is located 12 m above roof level and up to 191 events are used to form the conditional averages, the tilt of the single microfronts is probably lost due to the scatter of the individual runs.
- There is no time lag in the vertical velocity component of the flow between the three levels. This is consistent with the observations over vegetation canopies in the studies mentioned above.
- Streamwise velocities $\langle u' \rangle$ in general show the largest run-to-run scatter, this is especially true for $z/h = 3.2$. From the spectra shown in figs. 4.26-28, it is evident, that the horizontal component is ruled by larger time scales than $\langle w' \rangle$ and $\langle T' \rangle$.

4.5.4 Second-order moments

It is now of special interest, how the mean flux fields of momentum and sensible heat flux as a result of the organized structures look like for the observed runs and how much they contribute to the total flux. This is shown in fig. 4.36. The vertical cross-sectional velocity and temperature fields in figs. 4.36-37 have important consequences for the transfer of heat and momentum. Since $<w'>$ and $<T'>$ are positively correlated essentially everywhere through the ramp structure, the sensible heat flux is expected to be consistently down-gradient and therefore positive. Also its expected, that a large part of the total sensible heat flux is represented by the organized motions.The vertical structure of the velocity vector, and therefore the transfer of momentum, is found be more complex during a ramp event than the $<w'>$ $<T'>$ structure. The phase shift between the two velocity components $<u'>$ and $<w'>$ causes large run to run deviations of the conditional averages and occasional counter-gradient fields, tending to increase with height. A clear interpretation is therefore very difficult, because of the large scatter, especially at $z/h = 3.2$. Obviously, the organized structures seem to be not very efficient to transport horizontal momentum to the surface.

According to the theory section in chapter 2.6, the detected organized structures represent the conventionally Reynolds-averaged sensible heat flux to around 80 % at the two lower levels and 56 % at $z/h = 3.2$. The large-scale contributions are found to be 18 % and 13%, respectively (tab 4.13). Compared to other studies, where the ratio of conditionally sampled to conventionally averaged fluxes is often found to be around 1 and values of around 0.4 are reported for the large-scale contributions to the total sensible heat flux, the findings in this study are comparably poor. This could be for several reasons:

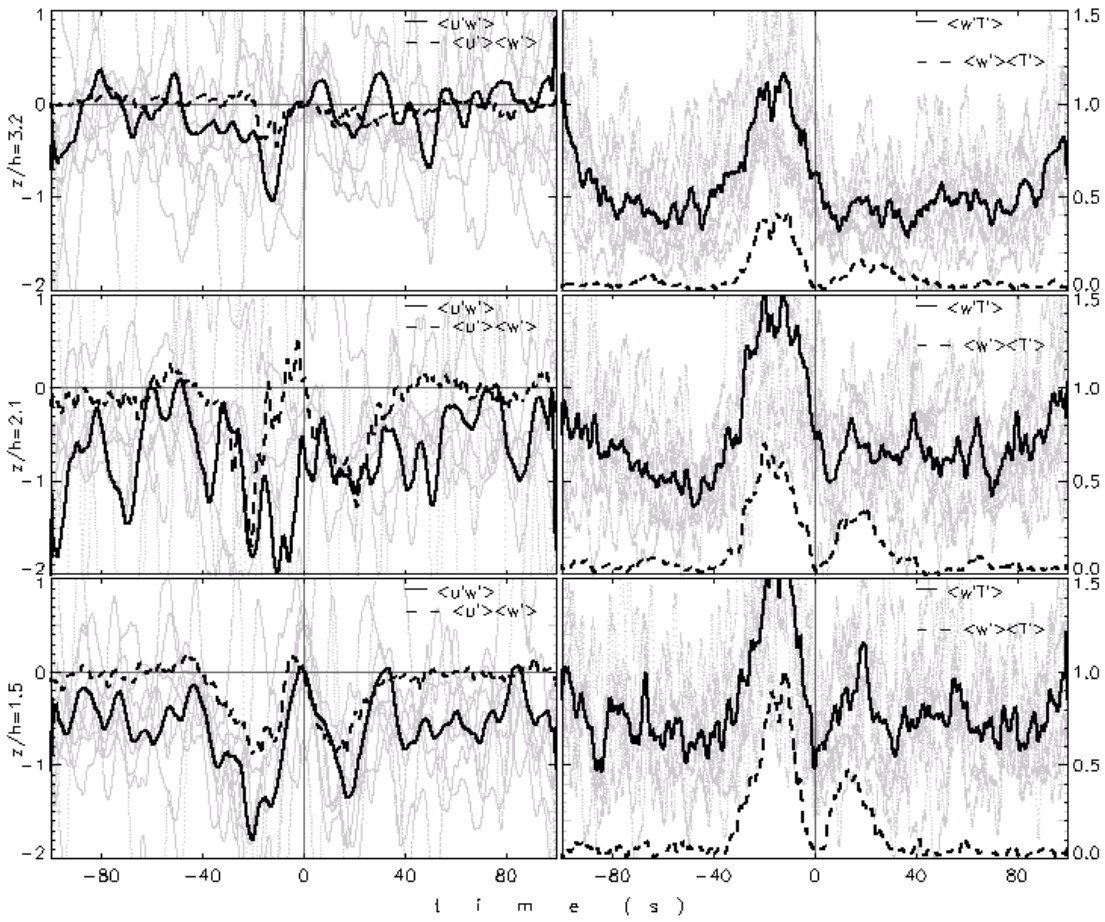

Fig. 4.36: Conditional averages <*u'w'*> and <*w'T'*> and cross-products <*u'*><*w'*> and <*w'*><*T'*> (normalized by $\left|\overline{u'w'}\right|$ and $\left|\overline{w'T'}\right|$, respectively,) for DOY 215, 10:00-18:00.

Tab. 4.13: Ratios of conditionally averaged heat flux to Reynolds flux and large-scale contributions for the runs of DOY 215, 216 and 217. *N* is the number of samples in a time window.

z/h	$\frac{\frac{1}{N}\sum_N < w'T' >}{\overline{w'T'}}$			$\frac{\sum_N (< w' >< T' >)}{\sum_N < w'T' >}$		
	DOY 215	DOY 216	DOY 217	DOY 215	DOY 216	DOY 217
3.2	0.56	0.44	0.54	0.13	0.13	0.14
2.1	0.74	0.60	0.67	0.17	0.19	0.19
1.5	0.81	0.74	0.70	0.18	0.20	0.18

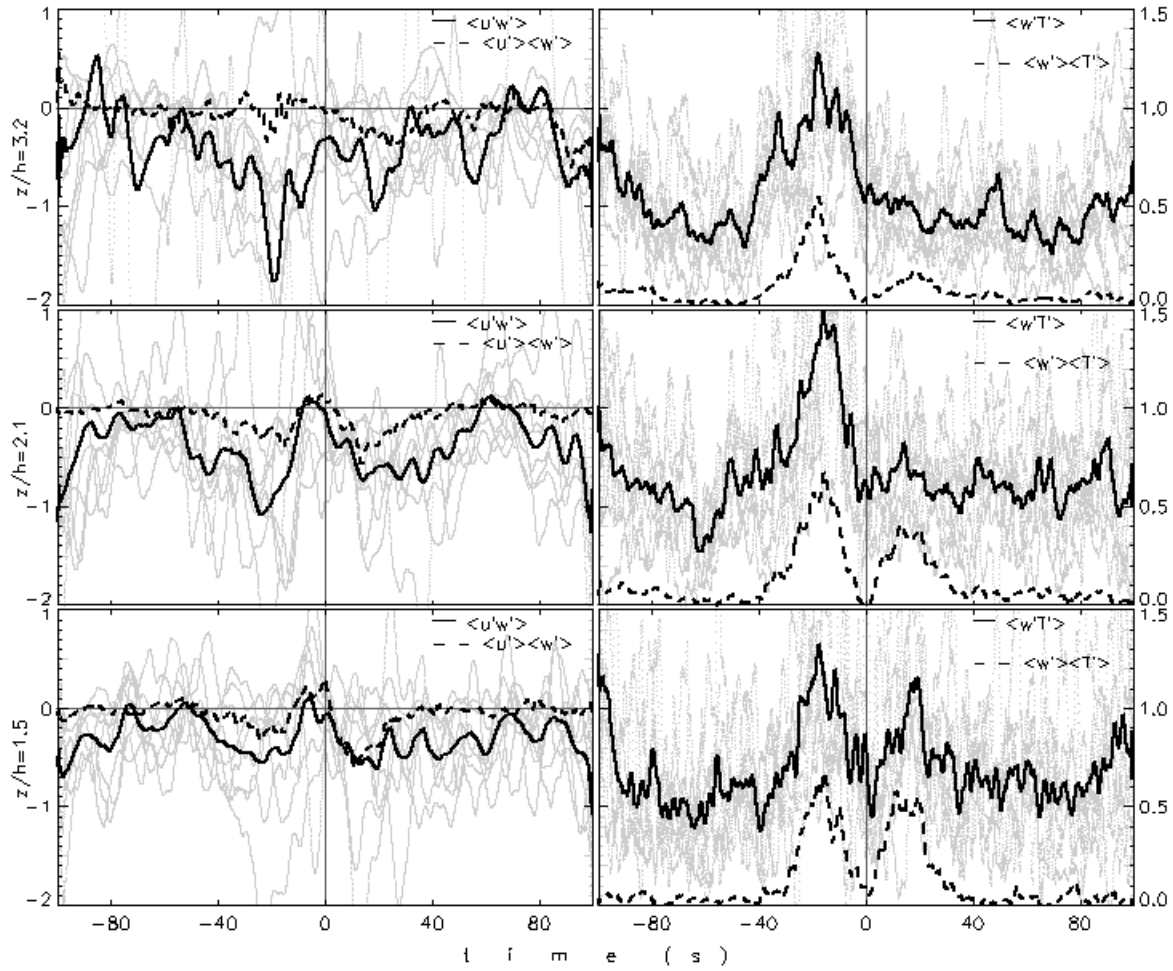

Fig. 4.37: Same as fig. 4.36 but for DOY 217, 10:00-18:00.

- The assumption of small and large-scale motions being uncorrelated made to obtain equation 2.65 is not entirely appropriate. This can be seen in figs. 4.36 and 4.37 where the small-scale contribution (the difference between $\langle w'T' \rangle$ and $\langle w' \rangle \langle T' \rangle$) seems to be roughly constant except towards the edges of the time-window.
- The detected structures and therefore the conditional averages only amount to about 60% (depending on the number of detected events) of a total run time. The missing 40 % is due to poorly defined (or not simultaneously occurring) temperature ramps.
- The variability in the length of the individual events is not taken into account.
- Probably the conditional averages of the fluxes are underestimated, because the time series of the individual events were detrended and rotated according to the procedure described in Appendix A.2.

Since the patterns of the conditional averages and the results in tab. 4.12 turn out to be remarkably stable for all of the selected periods, it is suggested that the methodical problems mentioned above are the reason for the poor representation of the conventional Reynolds-averaged fluxes by the conditionally averaged fluxes. Nevertheless, the patterns of sensible heat fluxes in figs. 4.36 and 4.37 show, that the efficiency of ejections to transport sensible heat is equal at all heights, whereas it decreases with height for sweeps. This is partly confirmed by quadrant analysis, where the contribution of sweeps to the total heat flux decreases slightly with height, whereas the contribution of ejections remains constant.

5 Summary and conclusions

Simultaneously measured turbulent time series of wind components and temperature at three different heights above an urban canopy in Basel, Switzerland, were analyzed within the MOS-framework, with respect to their spectral characteristics and by quadrant analysis and wavelet analysis to investigate organized structures of the flow. The most important turbulent characteristics and findings are summarized in the following.

5.1 Mechanical and thermal properties

The scaled vertical profiles of standard deviations $\sigma_{u,v,w}$ follow the MOS-predictions for the SL in the neutral case very well and are practically constant (or only slightly increasing) with height. The shape of the $\sigma_{u,v,w}$ profiles is strongly dependent on stability, for unstable conditions, $\sigma_{u,v}/u_{*top}$ decrease with height, whereas $\sigma_w/u_{*\,top}$ increases.

As instability increases ($(z\text{-}z_d)/L < -0.1$), locally scaled σ_w/u_* values fall below the reference curve, but finally approach the predicted 1/3 slope for free convection at all three levels. Deviations from the reference are largest at the uppermost level. In general, mechanical turbulence/turbulence properties are described satisfactorily by MOS-theory, using the local turbulent fluxes and stability indices as scaling variables.

Friction velocity u_* is increasing up to $z/h = 2.1$ and nearly constant for $z/h = 2.1$ and $z/h = 3.2$ for neutral and slightly unstable conditions. For strongly unstable conditions the profile is nearly constant.

Thermal turbulence/turbulence relationships such as σ_θ/θ_* follow MOS predictions for the two lower measurement levels well. All three levels they approach the predicted –1/3 slope for free convection. Profiles of σ_θ show a steady increase/decrease for stable and strongly unstable conditions, respectively, while for neutral and slightly unstable conditions, a decrease up to $z/h = 2.1$ and an increase up to $z/h = 3.2$ is observed.

The turbulent flux of sensible heat is found to decrease with height for neutral to unstable conditions and is nearly constant with height for stable conditions.

5.2 Organized motions

The detection of jumps in turbulent time series by the means of wavelet analysis is very efficient. The zero-crossing method in particular provides a excellent tool to analyze a large number of runs since it requires no empirical calibration. The detection performed on temperature time series and the subsequent conditional averaging results in representative patterns of the turbulent variables and the cross-products representing the vertical transfer. Ensemble vertical cross sections for velocity and temperature fields associated with large-scale eddy temperature ramp structures in the turbulent convective urban boundary layer show similar patterns as over vegetation surfaces, but with larger time scales according to the higher roughness elements. The patterns turn out to be remarkably stable for periods of up to 8 hours under unstable conditions, except for the cross-product of longitudinal and vertical velocity. Supported by the results of quadrant analysis and spectral analysis, substantial information on the dynamics of turbulent motions and transport processes and their dominating time- and length-scales is obtained. The dominating time scale of ejection-sweep cycles has been determined to be around 100 seconds. The temperature ramp size decreases with height, whereas vertical velocity fluctuations are fairly constant with height. The pattern of longitudinal velocity fluctuations performs as known from other studies over vegetation canopies, however, the at $z/h = 3.2$, the scatter becomes very large and the association with the temperature ramp is lost. Organized motions turn out to be very efficient in transporting sensible heat, while the transfer of momentum is not well represented.

5.3 The structure of the lower urban boundary layer

From the observations mentioned above, the height of the urban roughness sublayer is determined to lie somewhere around the measurement level of $z/h = 2.1$, the inflection point of the u_* profile for neutral and weakly unstable conditions. This is also confirmed by the turnaround of the dominance of ejections over sweeps for neutral and slightly unstable conditions in the quadrant analysis section. Also, the conditionally sampled longitudinal velocity component and the non-dimensionalized standard deviation of temperature at $z/h = 3.2$ point to a boundary between the two lower and the uppermost level. The non-dimensionalized spectral peak frequencies correspond best to SL-predictions at $z/h = 3.2$ for all spectra and cospectra. The dominating length scales derived from spectral peak frequencies show, that large eddies are broken up into smaller structures when approaching the roof level from above. Different source areas may also play a role for the separa-

tion. Derived from spectral peak frequencies for weakly unstable conditions, the 'typical' eddy size is 1200 m, 400 m and 140 m in its longitudinal, lateral and vertical extension, respectively, at z/h = 3.2, decreasing to 960 m, 320 m and 60 m at *z/h* = 1.5. The lowest level is strongly influenced by eddies that scale with thermal plumes and downdrafts linked to the energetics and morphometric properties of the urban surface, whereas the uppermost level is mainly driven by larger (boundary-layer) scale eddies in the surface (or even mixed) layer. The development and the height of the RS is strongly linked to the mechanical properties of the flow and the height of the roughness elements.

For strong unstable conditions, however, the urban boundary layer tends to be well mixed and profiles of the turbulent fluxes of momentum and sensible heat are nearly constant with height. The shift of the spectral peaks to lower frequencies for strong unstable conditions manifests that the flow is ruled by larger eddies. It is supposed, that the height of the RS is decreasing as instability increases. The flow is now mainly ruled by larger (boundary-layer) scale thermal plumes and downdrafts at all levels and only weakly influenced by the mechanical properties of the flow and the surface. Under unstable conditions, organized motions are very efficient in transporting sensible heat from the surface to higher layers and vice versa, whereas the transfer of momentum seems to loose importance. This is confirmed by the analysis of the organized structures.

5.4 Outlook

The findings in this study partly confirm, partly contradict the results from other studies that deal with the subject of urban turbulence. Since the structure of urban surfaces depends heavily on regional aspects, e.g. the morphometric properties of North American cities differ strongly from the properties of an European city, the complexity of the investigated terrain is different. Nevertheless, the results of this study seem to be characteristic for rough surfaces in general and for urban surfaces in particular. There is certainly more need to investigate the special nature of the turbulent exchange in and above urban canopies. When designing the setup of similar future studies, the following questions should be taken into account:

- How do the organized motions propagate in both directions in an urban environment, say downwards into the canopy layer and upwards to the mixed layer?
- Is the transfer of other scalars like humidity or trace gases by organized motions similar to the found pattern for the exchange of sensible heat?
- Are there other scaling parameters than they height above ground and the height of the roughness elements, i.e. geometric properties of the buildings and street canyons or the height of the mixed layer?
- Does a constant-flux layer exist at larger heights?
- How does the structure of the daytime mixed layer look like in the urban case?

References

Bergström, H., and Högström, U., 1989: Turbulent exchange above a pine forest, II: Organized structures, *Bound.-Layer Meteor.*, **49**, 231-263

Bisset, D. K., Antonie, R. A., and Browne, L. W. B., 1990: Spatial organization of large structures in the turbulent far wake of a cylinder, *J. Fluid. Mech.*, **162**, 439-461

Brunet, Y., and Collineau, S.,1994: Wavelet analysis of diurnal and nocturnal turbulence above a maize crop, in: *Wavelets in Geophysics*, edited by Foufoula-Georgiou, E., and Kumar, P., Academic Press, Inc., San Diego, pp. 129-150.

Businger, J. A., Wyngaard, J. C., Izumi, Y., and Bradley, E. F., 1971: Flux-profile relationships in the atmospheric surface layer, *J. Atmos. Sci.*, **28**, 181-189

Cermak, J. E., 1995: Physical modelling of flow an dispersion over urban areas, in: *Wind climate in cities*, edited by Cermak, J. E., Davenport, A. G., Plate, E. J., and Viegas, D. X., Kluwer Academic Publishers, Dordrecht

Chen, F., 1990a: Turbulent characteristics over a rough natural surface. Part I: Turbulent structures, *Bound.-Layer Meteor.*, **52**, 151-175

Chen, F., 1990b: Turbulent characteristics over a rough natural surface. Part II: Responses of profiles to turbulence, *Bound.-Layer Meteor.*, **52**, 301-311

Clarke, J. F., Ching, J. K. S., and Godowich, J. M., 1982: A study of turbulence in a urban environment, EPA, 150 pp.

Collineau, S., and Brunet, Y., 1993a: Detection of turbulent coherent motions in a forest canopy. Part I: Wavelet analysis, *Bound.-Layer Meteor.*, **65**, 357-379

Collineau, S., and Brunet, Y., 1993b: Detection of turbulent coherent motions in a forest canopy. Part II: Time-scales and conditional averages, *Bound.-Layer Meteor.*, **66**, 49-73

Coppin, P. A., and Taylor, K. J., 1983: A three-component sonic anemometer/thermometer system for general micrometeorological research, *Bound.-Layer Meteor.*, **27**, 27-42

Daubechies, I., 1992: Ten lectures on wavelets, Society for industrial and applied mathematics, Philadelphia, 357 pp.

De Bruin, H. A. R., Koshiek, W., and van den Hurk, B. J. J. M., 1993: A verification of some methods to determine the fluxes of momentum, sensible heat and water vapour using standard deviation and structure parameter of scalar meteorological quantities, *Bound.-Layer Meteor.*, **63**, 231-257

Eugster, W., 1994: Mikrometeorologische Bestimmung des NO2-Flusses an der Grenzfläche Boden/Luft, Ph.D. thesis, Universität Bern, Bern

Eugster, W., and Senn, W., 1995: A cospectral correction model for measurement of turbulent NO2 flux, *Bound.-Layer Meteor.*, **74**, 321-340

Farge, M., 1992: Wavelet transforms and their applications to turbulence, *Annu. Rev. Fluid Mech.*, **24**, 395-457

Feigenwinter, C., Vogt, R., and Parlow, E., 1996: Probing the urban boundary layer: Micrometeorological aspects of the BASTA project, in *Proceedings of ICUC (International Conference on Urban Climatology)*, Essen, Germany, pp. 75-76.

Feigenwinter, C., Vogt, R., and Parlow, E., 1999: Vertical structure of selected turbulence characteristics above an urban canopy, *Theor. Appl. Climatol.*, **62**, 51-63

Foufoula-Georgiou, E., and Kumar, P., 1994: Wavelets in Geophysics, in *Wavelet analysis and its applications*, edited by Chui, C. K., Academic Press, Inc., San Diego, pp. 373.

Gao, W., Shaw, R. H., and Paw U, K. T., 1989: Observation of organized structure in turbulent flow within and above a forest canopy, *Bound.-Layer Meteor.*, **47**, 359-377

Gao, W., Shaw, R. H., and Paw U, K. T., 1992: Conditional analysis of temperature and humidity microfronts and ejection/sweep motions within and above a deciduous forest, *Bound.-Layer Meteor.*, **59**, 35-57

Garratt, J. R., 1992: The atmospheric boundary layer, Cambridge University Press, Cambridge, U.K.

Grimmond, C. S. B., King, T. S., Roth, M., and Oke, T. R., 1998: Aerodynamic roughness of urban areas derived from wind observations, *Bound.-Layer Meteor.*, **89**, 1-24

Grimmond, C. S. B., and Oke, T. R., 1995: Comparison of heat fluxes from summertime observations in the suburbs of four north american cities, *J. Appl. Meteor.*, **34**, 873-889

Hagelberg, C. R., and Gamage, N. K. K.,1994a: Applications of structure preserving wavelet decompositions to intermittent turbulence: A case study, in: *Wavelets in Geophysics*, edited by Foufoula-Georgiou, E., and Kumar, P., Academic Press, Inc., San Diego, pp. 45-80.

Hagelberg, C. R., and Gamage, N. K. K., 1994b: Structure-preserving wavelet decompositions of intermittent turbulence, *Bound.-Layer Meteor.*, **70**, 217-246

Handorf, D., and Foken, T., 1997: Strukturanalyse der atmosphärischen Turbulenz mittels Wavelet-Verfahren zur Bestimmung von Austauschprozessen über dem antarktischen Schelfeis, Deutscher Wetterdienst, Offenbach a. Main

Högström, U., Bergström, H., and Alexandersson, H., 1982: Turbulence characteristics in a near neutrally stratified urban atmosphere, *Bound.-Layer Meteor.*, **23**, 449-472

Holschneider, M., 1995: Wavelets: An analysis tool, Clarendon Press, Oxford, 423 pp.

Howell, J. F., and Mahrt, L.,1994: An adaptive decomposition: Application to turbulence, in: *Wavelets in Geophysics*, edited by Foufoula-Georgiou, E., and Kumar, P., Academic Press, Inc., San Diego, pp. 107-128.

Hudgins, L., Friehe, C. A., and Mayer, M. E., 1993: Wavelet transforms and atmospheric turbulence, *Phys. Rev. Lett.*, **71**, (20), 3279-3282

Kaimal, J. C., and Finnigan, J. J., 1994: Atmospheric boundary layer flows: their structure and measurement, Oxford University Press, New York, 289 pp.

Kaimal, J. C., and Gaynor, J. E., 1991: Another look at sonic thermometry, *Bound.-Layer Meteor.*, **56**, 401-410

Kaimal, J. C., Wyngaard, J. C., Izumi, J., and Coté, O. R., 1972: Spectral characteristics of surface-layer turbulence, *Q. J. R. Meteorol. Soc*, **98**, 563-589

Katul, G., 1995: Estimation of surface heat and momentum fluxes using the flux-variance method above uniform and non-uniform terrain, *Bound.-Layer Meteor.*, **74**, 237-260

Katul, G. G., Finkelstein, P. L., Clarke, J. F., and Ellestad, T. G., 1996: An investigation of the conditional sampling method used to estimate fluxes of active, reactive, and passive scalars, *J. Appl. Meteor.*, **35**, 1835-1845

Katul, G. G., Kuhn, G., Schieldge, J., and Hsieh, C.-I., 1997: The ejection-sweep character of scalar fluxes in the unstable surface layer, *Bound.-Layer Meteor.*, **83**, 1-26

Katul, G. G., and Parlange, M. B., 1994: On the active role of temperature in surface-layer turbulence, *J. Atmos. Sci.*, **51**, 2181-2195

Kolmogorov, A. N., 1941: Energy dissipation in locally isotropic turbulence, *Doklady AN SSSR*, **32**, 19-21

Landsberg, H. E., 1981: The urban climate, Academic Press, New York, 275 pp.

Lumley, J. L., and Panofsky, H. A., 1964: The structure of atmospheric turbulence, Wiley-Interscience, New York, 239 pp.

Maitani, T., and Shaw, R. H., 1990: Joint probability analysis of momentum and heat fluxes at a deciduous forest, *Bound.-Layer Meteor.*, **52**, 283-300

Mazzoni, R., 1996: Turbulenzstruktur im gestörten Nachlauf einer künstlichen Oberflächenmodifikation, Ph. D. thesis, Eidgenössische Technische Hochschule, Zürich

Meneveau, C., 1991: Analysis of turbulence in the orthonormal wavelet representation, *J. Fluid. Mech.*, **232**, 469-520

Monin, A. S., and Obukhov, A. M.,1958: Fundamentale Gesetzmässigkeinter der turbulenten Vermischung in der bodennahen Schicht der Atmosphäre, in: *Sammelband der statistischen Turbulenz*, edited by Gpring, H., Akademie Verlag, Berlin

Oikawa, S., and Meng, Y., 1995: Turbulence characteristics and organized motions in a suburban roughness sublayer, *Bound.-Layer Meteor.*, **74**, 289-312

Oke, T. R., 1995: The heat island of the urban boundary layer: Characteristics, causes and effects, in: *Wind climate in cities*, edited by Cermak, J. E., Davenport, A. G., Plate, E. J., and Viegas, D. X., Kluwer Academic Publishers, Dordrecht, 772 pp.

Oke, T. R., 1987: Boundary Layer Climates, Methuen, London, 435 pp.

Panofsky, H. A., and Dutton, J. A., 1984: Atmospheric Turbulence. Models and methods for engineering applications, John Wiley & Sons, New York, 397 pp.

Paw U, K. T., Brunet, Y., Collineau, S., Shaw, R. H., Maitani, T., Qiu, J., and Hipps, L., 1992: On coherent structures in turbulence above and within agricultural plant canopies, *Agric. For. Meteorol.*, **61**, 55-68

Perrier, V., Philipovitch, T., and Basdevant, C., 1995: Wavelet spectra compared to Fourier spectra, *J. Math. Phys.*, **36**, 1506-1519

Raupach, M. R., 1981: Conditional statistics of Reynolds stress in rough-wall and smooth-wall turbulent boundary layers, *J. Fluid. Mech.*, **108**, 363-382

Rotach, M. W., 1991: Turbulence within and above an urban canopy, Dissertation thesis, Eidgenössische Technische Hochschule, Zürich, 245 pp.

Rotach, M. W., 1993a: Turbulence close to a rough urban surface. Part I: Reynolds stress, *Bound.-Layer Meteor.*, **65**, 1-28

Rotach, M. W., 1993b: Turbulence close to a rough urban surface. Part II: Variances and gradients, *Bound.-Layer Meteor.*, **66**, 75-92

Rotach, M. W., 1994: Determination of the zero plane displacement in an urban environment, *Bound.-Layer Meteor.*, **67**, 187-193

Rotach, M. W., 1995: Profiles of turbulence statistics in and above an urban street canyon, *Atmospheric Environment*, **29**, 1473-1486

Rotach, M. W., 1999: On the urban roughness sublayer, *Atmospheric Environment*, **33,** 4001-4008

Roth, M., 1999: Review of atmospheric turbulence over cities, *Q. J. R. Meteorol. Soc*, **accepted**

Roth, M., and Oke, T. R., 1993a: Tubulent transfer relationships over an urban surface: I: Spectral characteristics, *Q. J. R. Meteorol. Soc*, **119**, 1071-1104

Roth, M., and Oke, T. R., 1993b: Tubulent transfer relationships over an urban surface: II: Integral statistics, *Q. J. R. Meteorol. Soc*, **119**, 1105-1120

Schmid, H. P., and Rotach, M. W., 1997: Grenzschichtmeteorologie, ETH-Z, Zürich, pp.

Shaw, R. H., Paw U, K. T., and Gao, W., 1989: Detection of temperature ramps and flow structures at a deciduous forest site, *Agric. For. Meteorol.*, **47**, 123-138

Shaw, R. H., Tavangar, J., and Ward, D. P., 1983: Structure of Reynolds stress in a canopy layer, *J. Clim. Appl. Meteorol.*, **22**, 1922-1931

Shaw, R. H., and Zhang, X. J., 1992: Evidence of pressure-forced turbulent flow in a forest, *Bound.-Layer Meteor.*, **58**, 273-288

Stull, R. B., 1988: An introduction to boundary layer meteorology, Kluwer Academic Publishers, Dordrecht, 666 pp.

Tillmann, J. E., 1972: The indirect determination of stability, heat and momentum fluxes in the atmospheric boundary layer from simple scalar variables during dry unstable conditions, *J. Appl. Meteor.*, **11**, 783-792

Torrence, C., and Compo, G. P., 1998: A practical guide to wavelet analysis, *Bull. Am. Met. Soc.*, **97**, (1), 61-78

van Gorsel, E., 1998: Aspekte der turbulenten Strömung über einer städtischen Oberfläche, Diploma thesis, University of Basel, Basel, l

Vogt, R., 1995: Theorie, Technik und Analyse der experimentellen Flussbestimmung am Beispiel des Hartheimer Kiefernwaldes, Ph.D. thesis, University of Basel, Basel, 101 pp

Vogt, R., Feigenwinter, C., Paw U, K. T., and Pitacco, A., 1997: Intercomparison of ultrasonic anemometers, in *Proceedings of the 12th Symposium of Boundary Layers and Turbulence*, Vancouver, Canada, 354-355.

Wallace, J. M., Eckelmann, H., and Brodkey, R. S., 1972: The wall region in turbulent shear flow, *J. Fluid. Mech.*, **54**, 39-48

Wickerhauser, M. V., 1993: Adapted wavelet analysis from theory to software, Vieweg & Sohn, Braunschweig, 440 pp.

Wilczak, J. M., 1984: Large-scale eddies in the unstably stratified atmospheric surface layer: Part I: Velocity and temperature structure, *J. Atmos. Sci.*, **41**, (24), 3537-3550

Wyngaard, J. C., Coté, O. R., and Izumi, Y., 1971: Local free convection, similarity, and the budgets of shear stress and heat flux, *J. Atmos. Sci.*, **28**, 1171-1182

A Appendix

A.1 Ultrasonic anemometer thermometer measurement principles

The ultrasonic anemometer (sonic) is generally regarded as one of the best instruments for the study of atmospheric turbulence. Whilst the first sonics were large, very expensive and awkwardly to use, recent devices are attainable, quite robust and relatively easy to operate. The sonics used in this study (Solent Gill Research) are capable of measuring all three wind components and temperature. Vogt (1995, 1996, 1997, 1998) has extensively tested the instruments of this manufacturer. In practice, the Gill-sonics are easy to operate and very reliable.

The velocity of a sound pressure wave is measured on 3 differently oriented paths, and from this, the wind vector and the temperature is derived. This is shown in detail for a single path in fig. A.1. The transit times t_1 and t_2 for a sound wave of frequency f to travel from transducer (transmitter/receiver) TR1 to transducer TR2 and vice versa are measured. In practice, TR1 and TR2 work as transmitter and receiver alternately.

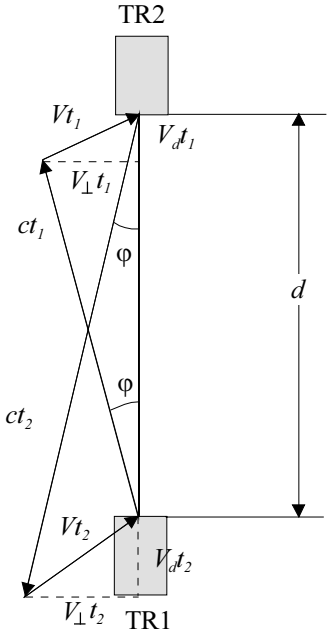

Fig. A.1: Schematic view of a sonic path

If the switching between transmitting and receiving is sufficiently fast, the wind vector $\boldsymbol{V}$ with its components V_p (along the path) and $V_\perp$ (normal to the path) is supposed to be invariant and for t_1 and t_2 the following equations hold:

$$t_1 = \frac{d}{c\cos\varphi + V_p} \tag{A.1}$$

$$t_2 = \frac{d}{c\cos\varphi - V_p} \tag{A.2}$$

where d is the distance apart of the transducers, c the local speed of sound in calm air and φ the deviation of the path caused by the component of the wind vector normal to the path. From the above equations the along path component of the wind vector can be written as

$$V_p = \frac{d}{2}\left(\frac{1}{t_1} - \frac{1}{t_2}\right). \tag{A.3}$$

Equation (A.3) gives an 'absolute' calibration (Coppin and Taylor, 1983), which is dependent only on the distance between the transducers d. For newer sonics, this method is used for online calibration, since the problem to measure and compute the reciprocals of the travel times in real time has been solved.

With the relations $V^2 = V_p^2 + V_\perp^2$ and $\sin(\alpha) = V_\perp / c$ (see fig. A.1), it follows from eqs.(A.1,2), that

$$t_2 - t_1 = \frac{2dV_p}{c^2 - V^2} \tag{A.4}$$

$$t_2 + t_1 = \frac{2dc\cos\varphi}{c^2 - V^2}. \tag{A.5}$$

Equation (A.5) provides the means for measuring temperature. According to theory, the speed of sound c in moist air is given by

$$c = 20.067\sqrt{T(1 + 0.32\frac{e}{p})}, \tag{A.6}$$

where T is the absolute temperature of the air, e the vapor pressure of water, and p the atmospheric pressure[1]. If we substitute e/p by the specific humidity $q \approx 0.622e/p$, eq. (A.5) becomes

$$c = 20.067\sqrt{T(1 + 0.51q)} \tag{A.7}$$

Due to the similarity of eq. (A.7) with the meteorological virtual temperature $T_v = T(1+0.61q)$, defined as the temperature at which dry air has the same density as moist air at the same pressure, Barret and Suomi (1949) introduced the term of

[1] The value of the factor 0.32 varies slightly in literature. It is dependent on the ratio of specific heat capacities of dry and moist air at constant pressure, which vary both with temperature. 20.067 is the square root of the product of c_p/c_v (the ratio of the specific heat capacities) for dry air and the gas constant for dry air (278.04 $Jkg^{-1}K^{-1}$).

'acoustic virtual temperature' $T_{sv}=T(1+0.51q)\approx T_v$ (or simply 'sonic temperature' after Kaimal and Gaynor, 1991). Thus eq. (A.7) can be written as

$$c = 20.067\sqrt{T_{sv}} \qquad \text{(A.8)}$$

and by substituting c in eq. (A.8) from eqs.(A.1,2), the formula for sonic temperature T_{sv} derives as

$$T_{sv} = \frac{d^2}{1612}\left(\frac{1}{t_1}+\frac{1}{t_2}\right)+\frac{V_\perp^2}{403}. \qquad \text{(A.9)}$$

T_{sv} considers therefore the buoyancy contribution from moisture in the kinematic heat flux $\overline{w'T'}$ when calculating the Monin-Obukhov stability parameter $(z-z_d)/L$. The same is valid for the buoyant production term in the turbulent kinetic energy budget in eq.(2.11). For a typical standard deviation of the short term humidity fluctuations e' of 0.5 mb above a very moist surface, Kaimal and Gaynor (1991) calculated the error of using T_{sv} instead of T_v to be around 0.01 K, which is well within the bounds of experimental uncertainty.

Schotanus et al. (1983) presented a correction for these errors, provided that the humidity fluctuations are measured simultaneously, which is not the case in this study. They reported deviations of 5% and 10% from σ_T and $\overline{w'T'}$, corresponding to departures of 1% and 2% for σ_{Tv} and $\overline{w'T_v'}$, respectively, which is well within the experimental error in most field observations. In this study, the temperature fluctuations are calculated according to eq. (A.9).

A.2 The Gill-Solent 3 axis research ultrasonic anemometer/thermometer

The geometry of the Gill Research Sonic was designed to minimize the flow distortion around the transducers. For this reason, the suspension of the sensors is asymmetrically, with a wide open undisturbed sector that is meant to be aligned against the mean upwind direction (fig. A.2). A pulse is sent every 10^{-3} seconds and the travel time between a transducer pair is measured. This is done subsequently for every direction and every transducer pair, thus a complete measurement cycle lasts 6 ms. The instrument offers 4 different modes of operation:

Additionally, up to 5 analogue-channels can be measured with a frequency of 10 Hz and an input range between 0 to 5 V.

In this study, all three sonics have been operated in mode 3. The output transit counts are therefore averages of 8 measurements cycles, this should avoid problems due to aliasing (Kaimal and Finnigan, 1994). With the known quartz frequency of 29.491 MHz, the transit counts can be transformed to the required travel times t_1 and t_2 for the equations of chapter A.1. According to the geometry of the transducer array, the original path components can be transformed to a vector in the sonic coordinate system (x_s, y_s, z_s). The matrix describing the along path unit vectors in the sonic coordinate system (x_s, y_s, z_s) is given by:

Tab. A.1: Operation modes of the Gill Research sonic

Mode	1	2	3	4
output frequency	20.83 Hz	20.83 Hz	20.83 Hz	55.55 Hz
output format	*u, v, w, c* (manufacturer's calibration)	*u, v, w, c* not calibrated	6 transit counts	6 transit counts

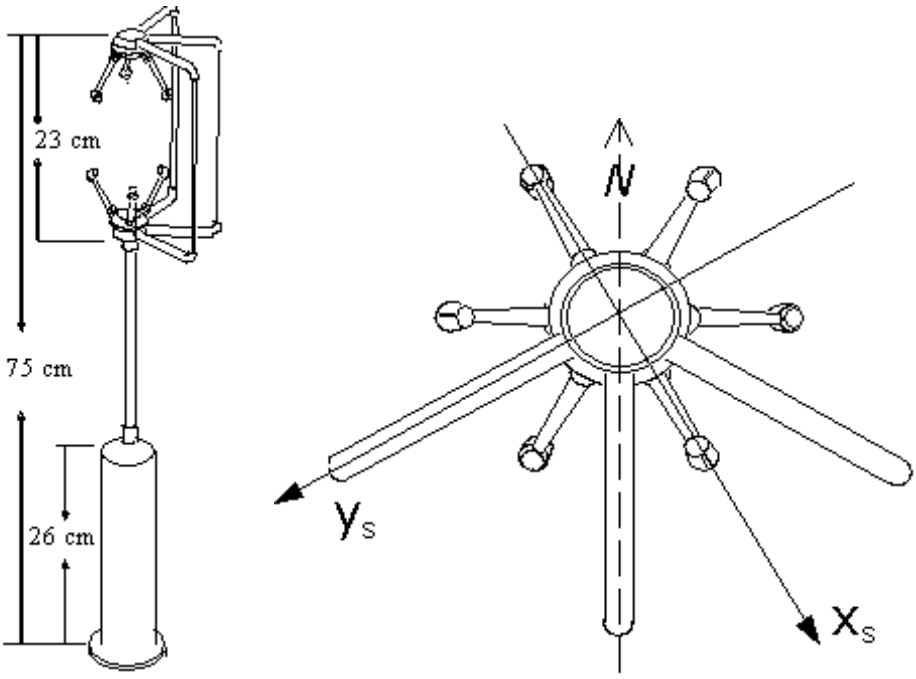

Fig. A.2: Side-view (left) and top-view (right) of the Gill-Solent sonic anemometer/thermometer

$$ep_{ij} = \begin{bmatrix} \cos\varphi_1 \cos\upsilon_1 & \sin\varphi_1 \cos\upsilon_1 & -\sin\upsilon_1 \\ -\cos\varphi_2 \cos\upsilon_2 & \sin\varphi_2 \cos\upsilon_2 & -\sin\upsilon_2 \\ -\cos\varphi_3 \cos\upsilon_3 & -\sin\varphi_3 \cos\upsilon_3 & -\sin\upsilon_3 \end{bmatrix} \quad \text{(A.10)}$$

with $\upsilon_{1,2,3} = 45°$ as the angles between the paths and the horizontal plain defined by the three lower transducers, and $\varphi_{2,3} = 60°$ and $\varphi_1 = 0°$ as the angles between the projection of the paths on the horizontal plain defined by the three lower transducers and the x_2-axis. A vector $\boldsymbol{V}$ with the components v_1, v_2, v_3 in the sonic coordinate system can then be transformed to a vector **P** with the along path components p_1, p_2, p_3 by:

$$P_i = ep_{ij} V_j \qquad i, j = 1, 2, 3 \qquad \text{(A.11)}$$

By inverting ep_{ij}, we the required components $\boldsymbol{V_i}$ can be calculated from $\boldsymbol{P}$:

$$V_i = ev_{ij} P_j \qquad i, j = 1, 2, 3 \qquad \text{(A.12)}$$

with

$$ev_{ij} = \begin{bmatrix} \frac{2\sqrt{2}}{3} & -\frac{\sqrt{2}}{3} & -\frac{\sqrt{2}}{3} \\ 0 & \sqrt{\frac{2}{3}} & -\sqrt{\frac{2}{3}} \\ -\frac{\sqrt{2}}{3} & -\frac{\sqrt{2}}{3} & -\frac{\sqrt{2}}{3} \end{bmatrix}. \qquad \text{(A.13)}$$

It has to be mentioned, that deviations from this standard geometry can have crucial effects on the results, especially on temperature measurements. Gill recommends to measure the pathlengths individually to reach a higher precision. This has been done with the instruments used in this study (Vogt, 1995).

Over flat, homogeneous terrain, it is expected, that the turbulent properties of the flow only change in the vertical direction, which implies, that the mean vertical wind $\overline{w} = 0$. In more complex flows, i.e. above an urban surface, or if the sensor is not aligned horizontally, it is usual to allow the flow to set the coordinate direction instead of using Cartesian coordinates (Kaimal and Finnigan, 1994). An appropriate way for this strategy is to transform the measurements from the reference frame of the instrument $\boldsymbol{V}$ into streamline coordinates $\boldsymbol{U}$. $\overline{U}$ then refers to the local mean wind vector with its components $\overline{u}$ as the longitudinal (streamline), $\overline{v}$ as the lateral (binormal) and $\overline{w}$ as the vertical (principal normal) component.

In a first step, time series of wind velocities are averaged to produce a mean wind vector $\boldsymbol{A}$ with components $(\overline{a}_1, \overline{a}_2, \overline{a}_3)$ in the sonic coordinate system (x_s, y_s, z_s). A first transformation rotates x_s and y_s around the vertical axis z_s into the new coordinate system defined by (x_2, y_2, z_2) to force $\overline{v} = 0$ and results in a vector $\boldsymbol{B}$ with the components $(\overline{b}_1, \overline{b}_2 = 0, \overline{b}_3 = \overline{a}_3)$. Mathematically written, the rotation turns out to be

$$\overline{b}_i = e_{2ij} \overline{a}_j \qquad i, j = 1, 2, 3$$

with

$$e_{2ij} = \begin{bmatrix} \cos\varphi & \sin\varphi & 0 \\ -\sin\varphi & \cos\varphi & 0 \\ 0 & 0 & 1 \end{bmatrix} \qquad \text{(A.14)}$$

and the rotation angle φ as

$$\varphi = \tan^{-1}\left(\frac{\overline{a}_2}{\overline{a}_1}\right). \qquad \text{(A.15)}$$

The second transformation rotates $\boldsymbol{B}$ around the y_2-axis to force $\overline{w} = 0$ and finally results in the along wind vector $\boldsymbol{U}$ with the components $(\overline{u}_1 = \overline{u}, \overline{u}_2 = \overline{v} = 0, \overline{u}_3 = \overline{w} = 0)$:

$$\overline{u}_i = e_{3ij} \overline{b}_j \qquad i, j = 1, 2, 3$$

with

$$e_{3ij} = \begin{bmatrix} \cos\vartheta & 0 & \sin\vartheta \\ 0 & 1 & 0 \\ -\sin\vartheta & 0 & \cos\vartheta \end{bmatrix} \qquad \text{(A.16)}$$

and the rotation angle ϑ as

$$\vartheta = \tan^{-1}\left(\frac{\overline{b}_3}{\sqrt{\overline{b}_1^2 + \overline{b}_2^2}}\right). \qquad \text{(A.17)}$$

The new coordinate system then is the required along streamline system (u, v, w).

A.3 Sonic calibration and intercomparison

After the measurement campaign at the end of February 1996, all three sonics have been recalibrated in the wind tunnel. Vogt (1995) has extensively investigated the influence of several calibration methods on the accuracy of sonic measurements. In the present study, a matrix calibration is used. The matrix has been derived by tilting the sonic at 11 positions (ϑ angles -25° to 25° in 5° steps) and rotating 360° at each position (resolved in 4° steps). Two different matrices are derived for positive and negative tilting angles respectively. This procedure was performed for tunnel speeds of 2, 4, 6, and 8 m/s. See Vogt (1996, 1997) for a comprehensive description of the experimental setup, the methodology and the results.

Testing the instruments in the wind tunnel results in better knowledge of the behavior under well controlled laminar flow conditions. Nevertheless, it is of particular interest, if the results from the laboratory can be applied to turbulent boundary layer flows in field studies and how the instruments perform under nearly identical flow conditions in the field. Therefore, the three sonics were intercompared during a field campaign in April 1996 in Tuscany, Italy. The instruments have been aligned in a row at a height of 1.8 m. Horizontal spacing was around 1.1 m (fig. A.3). Disturbed sectors were excluded from the analysis.

The comparison of the matrix calibration and the manufacturer's (Gill-) calibration shows that differences in are not significant in the case of the mean wind velocity $\boldsymbol{U}$ (except #35), the kinematic heat flux $\overline{w'T'}$ and the standard deviations for the vertical wind fluctuation σ_w and temperature fluctuation σ_T . However, the friction velocity u_* calculated by the Gill-calibration is generally larger for high values of u_* and smaller for low values of u_* compared to the matrix calibration.

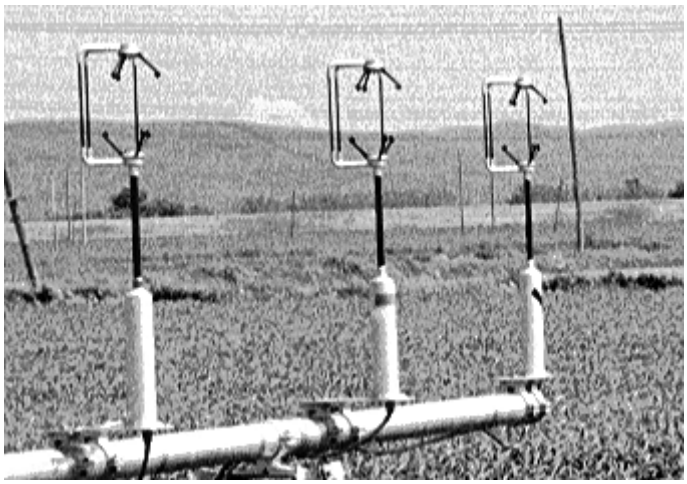

Fig. A.3: The three sonics at the field intercomparison in Tuscany 1996

Tab. A.2: Regression coefficients for calibration comparison: $y_{gill}=a0+a1*x_{matrix}$

parameter	sonic #	a1	a0	r^2
$\boldsymbol{U}$	#36	0.98	0.20	0.998
	#35	1.06	0.05	0.996
	#43	1.00	0.04	0.999
u_*	#36	1.21	-0.09	0.968
	#35	1.12	-0.03	0.994
	#43	1.00	0.02	0.999

The comparison between the instruments among each other is of particular interest, since flow conditions should be nearly identical for the setup shown in fig. A.3, influenced only by the horizontal spacing of the sensors. Results of the intercomparison of the three instruments are shown in fig. A.5 and tab. A.3. In general, all three pairs show good agreement for the measured parameters $\boldsymbol{U}$, σ_w and σ_T. However, a different behavior of the three pairs is found for different parameters. For mean windspeed $\boldsymbol{U}$ and the standard deviation of vertical windspeed σ_w, the pair #43/#35 corresponds best, while for σ_T , the pair #36/#35 shows the best agreement. One explanation for this lies in the computation of the sonic temperature. Since the temperature is the mean of the three paths, a deviation in only one path can influence the calculation essentially. Additionally, the pathlength is the decisive parameter for sonic temperature calculation. Vogt (1995) found that differences in pathlengths recalculated from wind tunnel temperature compared to the measured pathlengths to be up to 1 mm, which corresponds to temperature differences of ± 0.3 K. He supposed, that the reason for this deviation could be due to *transducer shadowing* effects. Scatter is largest for parameters u_* and $\overline{w'T'}$. This is not surprising, since these are combined values and the effect of the horizontal spacing of the instruments has a greater influence.

Tab. A.3: Regression coefficients and standard deviations for instrument comparison: $y_{instr\ 1}=a0+a1*x_{instr\ 2}$

parameter	instr 1	instr 2	a1	a0	σ	r^2
$\boldsymbol{U}$	#35	#36	0.979	0.035	0.013	0.997
	#43	#36	0.996	0.075	0.016	0.995
	#43	#35	1.019	0.032	0.010	0.998
u_*	#35	#36	1.119	-0.130	0.086	0.921
	#43	#36	1.118	-0.089	0.067	0.941
	#43	#35	0.868	0.059	0.040	0.963
$\overline{w'T'}$	#35	#36	0.836	0.011	0.028	0.981
	#43	#36	0.883	0.009	0.028	0.982
	#43	#35	1.0448	-0.002	0.026	0.989
σ_w	#35	#36	0.986	-0.033	0.031	0.984
	#43	#36	1.019	-0.007	0.030	0.984
	#43	#35	0.971	0.023	0.018	0.994
σ_T	#35	#36	1.025	-0.022	0.019	0.994
	#43	#36	1.010	-0.010	0.036	0.978
	#43	#35	0.975	0.035	0.034	0.978

.

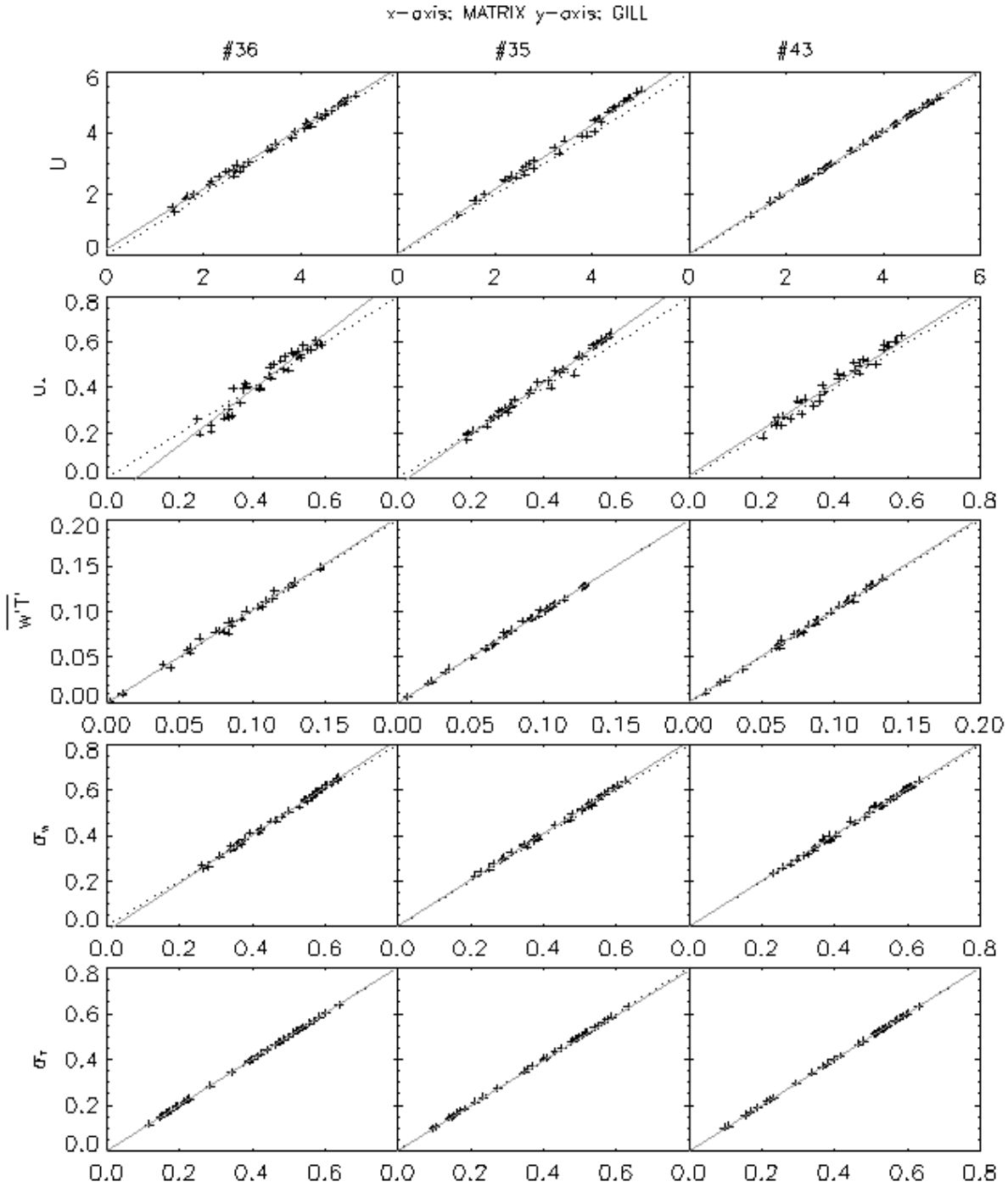

Fig. A.4: Comparison of matrix calibration and manufacturer's (Gill-) calibration. Regression line solid, light gray, 1:1 line dotted.

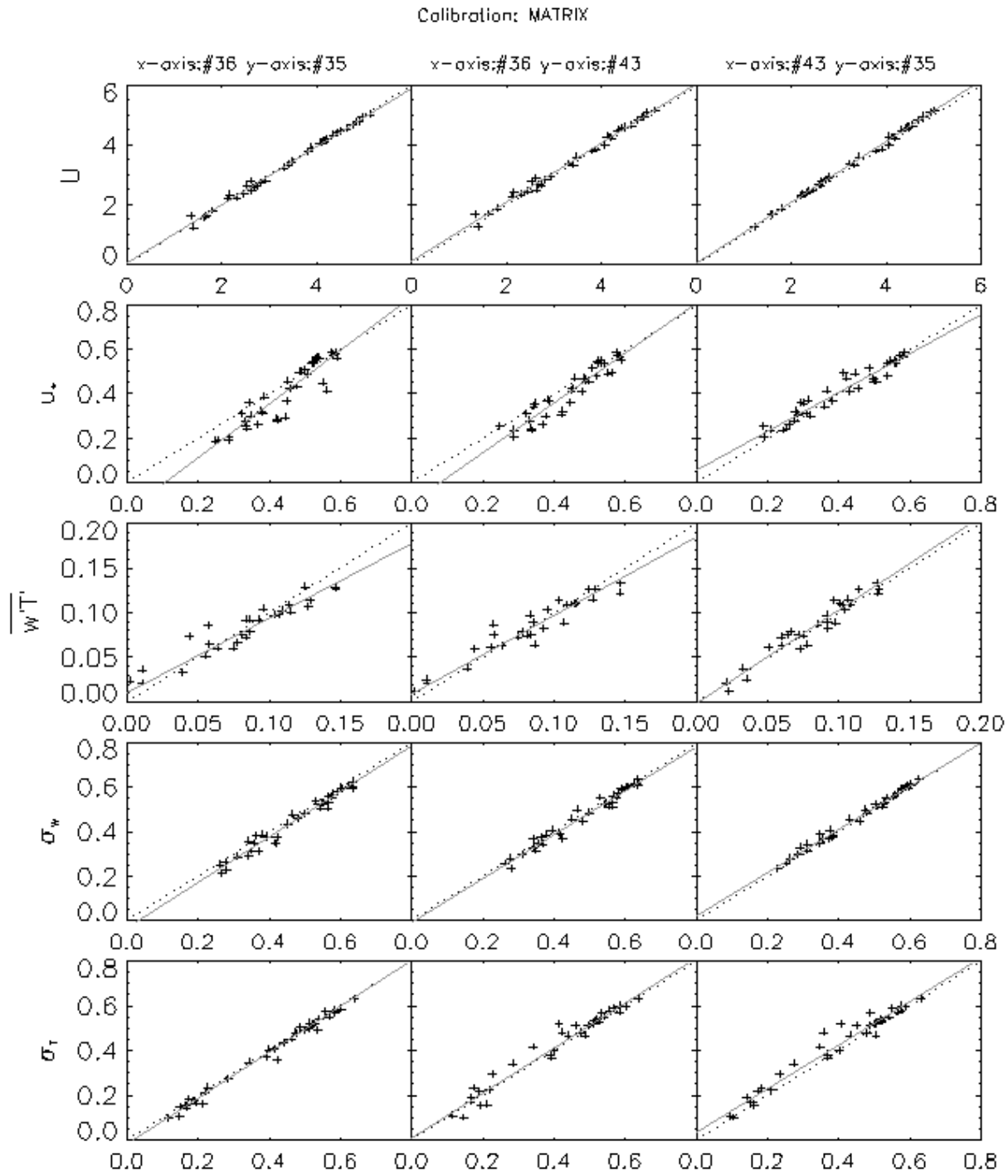

Fig. A.5: Comparison between instruments. Regression line solid, light gray, 1:1 line dotted.